

A HIGH EFFICIENCY AND LOW NOISE MAGNETRON
CATHODE USING GALLIUM NITRIDE AND SILICON
CARBIDE POLYMERS FOR MODULATED MICROWAVE
POWER TRANSMISSION

LEONG WEN CHEK

FACULTY OF ENGINEERING
UNIVERSITI MALAYA
KUALA LUMPUR

2022

**A HIGH EFFICIENCY AND LOW NOISE
MAGNETRON CATHODE USING GALLIUM CARBIDE
AND SILICON CARBIDE POLYMERS FOR
MODULATED MICROWAVE POWER TRANSMISSION**

LEONG WEN CHEK

**THESIS SUBMITTED IN FULFILMENT OF THE
REQUIREMENTS FOR THE DEGREE OF DOCTOR OF
PHILOSOPHY**

**FACULTY OF ENGINEERING
UNIVERSITI MALAYA
KUALA LUMPUR**

2022

UNIVERSITI MALAYA
ORIGINAL LITERARY WORK DECLARATION

Name of Candidate: Leong Wen Chek

Matric No: 17056602/2 (KHA160039)

Name of Degree: Doctor of Philosophy

Title of Thesis: A High Efficiency and Low Noise Magnetron Cathode Using Gallium Carbide and Silicon Carbide Polymers for Modulated Microwave Power Transmission

Field of Study: Power Electronics

I do solemnly and sincerely declare that:

- (1) I am the sole author/writer of this Work;
- (2) This Work is original;
- (3) Any use of any work in which copyright exists was done by way of fair dealing and for permitted purposes, and any excerpt or extract from, or reference to or reproduction of any copyright work has been disclosed expressly and sufficiently, and the title of the Work and its authorship have been acknowledged in this Work;
- (4) I do not have any actual knowledge, nor do I ought reasonably to know that the making of this Work constitutes an infringement of any copyright work;
- (5) I hereby assign all and every rights in the copyright to this Work to the Universiti Malaya ("UM"), who henceforth shall be owner of the copyright in this Work and that any reproduction or use in any form or by any means whatsoever is prohibited without the written consent of UM having been first had and obtained;
- (6) I am fully aware that if in the course of making this Work I have infringed any copyright whether intentionally or otherwise, I may be subject to legal action or any other action as may be determined by UM.

Candidate's Signature

Date: 26 October 2022

Subscribed and solemnly declared before,

Witness's Signature

Date: 26 October 2022

Name:

Designation:

ABSTRACT

A HIGH EFFICIENCY AND LOW NOISE MAGNETRON CATHODE USING GALLIUM CARBIDE AND SILICON CARBIDE POLYMERS FOR MODULATED MICROWAVE POWER TRANSMISSION

Microwave Power Transmission is one of the potential fantastic technologies in Wireless Power Transmission apart from Inductive Coupling, Resonant Inductive Coupling, Capacitive Coupling, Magnetic Resonant, Radio Frequency, Laser Power and Laser Light Wireless Power Transmission. Microwave Power Transmission performs better for low power applications due to its far-field transmission distance. However, due to safety and health concerns, the research on Microwave Power Transmission has been reduced and requires high costs to conduct the experimental investigation. The Magnetron is one of the most commonly used microwave power generators for commercial or industrial applications. The system's efficiency is mainly affected by factors such as the building materials, resonant cavity size, operation space size, anode structure, and operating frequency. Previous researchers have emphasized implementing GaN on SiC polymer in various power device applications such as high electron-mobility transistors, power diodes, and microwaves. However, the solution proposed in this thesis is the first reported for implementing the same polymer in a magnetron's cathode surface. This thesis proposes the modification of magnetron cathode for high frequency and low power applications using Silicon Carbide (SiC) and Gallium Nitride (GaN) coated cathode polymer replacing traditional Barium Oxide (BaO) substrate through an annealing process. The highlighted optimization is intended to modify the control of magnetron electron flow velocity to reduce heat dissipation. Sudden temperature rise during magnetron operation reduces its efficiency because it loses its stability. Simulation and experimental results have been extracted at 2,45MHz to generate 5W microwave power

and tested for over 10 m. of power transmission using a rectenna interface, which results in an efficiency of 87%, compared to 36% using a BaO coat.

Keywords: Microwave power transmission, Magnetron cathode, Annealing, Gallium Nitride, Silicon Carbide, Barium Oxide

Universiti Malaya

ABSTRAK

KATOD MAGNETRON BERKECEKAPAN TINGGI DAN GANGGUAN RENDAH MENGGUNAKAN POLIMER GALLIUM KARBIDA DAN SILIKON KARBIDA UNTUK PENGHANTARAN KUASA GELOMBANG MIKRO BERMODULASI

Transmisi Daya Gelombang Mikro adalah salah satu teknologi yang berpotensi dalam Penghantaran Daya Tanpa Wayar untuk masa depan selain dari Gandingan Induktif, Gandingan Induktif Resonan, Gandingan Kapasitif, Resonan Magnetik, Frekuensi Radio, Daya Laser dan Penghantaran Daya Tanpa Wayar Laser. Penghantaran Daya Gelombang Mikro lebih menjanjikan untuk aplikasi daya rendah kerana jarak penghantaran medan yang jauh. Namun, kerana keselamatan dan kesihatannya, penelitian mengenai Transmisi Daya Gelombang Mikro telah mengurangkan dan memerlukan biaya yang sangat tinggi untuk melakukan eksperimennya. Magnetron adalah salah satu penjana kuasa gelombang mikro yang paling biasa digunakan untuk aplikasi komersial atau perindustrian. Kecekapan sistem terutamanya dipengaruhi oleh beberapa faktor seperti bahan binaan, ukuran rongga resonan, ukuran ruang operasi, struktur anod dan frekuensi operasi. Kerja penyelidikan yang pernah dilaporkan sebelum ini menjurus kepada penggunaan semikonduktor GaN dan SiC dalam peralatan kuasa, transistor dan gelombang mikro. Kajian yang dilaporkan dalam kerja tesis ini adalah yang pertama mencadangkan penggunaan semikonduktor GaN dan SiC di atas permukaan katod magnetron. Tesis ini mencadangkan pengubahsuaian katod magnetron untuk aplikasi frekuensi tinggi dan kuasa rendah menggunakan polimer katod bersalut Silicon Carbide (SiC) dan Gallium Nitride (GaN) menggantikan substrat Barium Oksida tradisional (BaO). Pengoptimuman yang disorot bertujuan untuk mengubah kawalan kelajuan aliran elektron magnetron untuk mengurangkan pelepasan haba. Kenaikan suhu secara tiba-tiba semasa operasi magnetron akan mengurangkan kecekapannya kerana magnetron kehilangan

kestabilannya. Hasil simulasi dan eksperimen telah diekstraksi pada 2,45GHz untuk menghasilkan daya gelombang mikro 5W dan diuji untuk transmisi daya lebih dari 10 m menggunakan antara muka rectenna, yang menghasilkan efisiensi 87%, dibandingkan dengan 36% menggunakan lapisan BaO.

Kata kunci: Penghantaran kuasa gelombang mikro, Katod magnetron, Penyepuhlindapan, Galium Nitrida, Silikon Karbida, Barium Oksida

Universiti Malaya

ACKNOWLEDGEMENTS

First and foremost, I would like to express my deepest gratitude to my supervisors, Honorary Professor Dr. Saad Mekhilef and Professor Ir. Dr. Harikrishnan Ramiah, for their support and guidance throughout the journey. Without their continuous support, it is impossible to accomplish and achieve the objectives of this study. Their emotional, mental, and even technical support has guided me to be more prepared and face the upcoming future professionally. I will never forget and extend the knowledge I gained during my study to the next generation.

Special thanks, appreciation, and acknowledgment to Motorola Solutions, Mini-Circuits Technologies, and Universiti Malaya for funding and facilities for this research. Motorola Solutions and Mini-Circuits Technologies have granted us full access to the facilities and supplies of raw materials for experimental verification. Such experience in the industry leads to a higher quality of experimental results and the opportunity to implement the proposed solutions in a dynamic wireless charging system to charge walkie-talkies wirelessly. Without the funding from Universiti Malaya, this Work would be just a dream.

My sincere indebtedness to my research colleagues in Power Electronics and Renewable Energy Research Laboratory (PEARL), Universiti Malaya, for their constructive and motivational comments, especially during the monthly progress presentation. Having various friends around the globe has given me a fruitful journey knowing various cultures that some of them had never heard of before.

Lastly, the word cannot express how much my family means to me throughout this journey. They are always by my side to support me no matter what happens, and you will always have a special place in my heart.

TABLE OF CONTENTS

Abstract	ii
Abstrak	iv
Acknowledgements	vi
Table of Contents	vii
List of Figures	x
List of Tables.....	xiii
List of Symbols and Abbreviations.....	xiv
CHAPTER 1: INTRODUCTION.....	1
1.1 Research Background	1
1.2 Problem Statement	3
1.3 Research Scope	4
1.4 Research Objectives	5
1.5 Research Methodology	6
1.6 Thesis Outline	7
CHAPTER 2: LITERATURE REVIEW.....	8
2.1 Introduction	8
2.2 Current Technology on Microwave Power Transmission	8
2.3 Magnetron History	12
2.4 Basic of Magnetron	15
2.5 Types of Microwave Power Generators	17
2.5.1 Negative Resistance Type	20
2.5.2 Cyclotron Frequency Magnetrons	21
2.6 Magnetron Optimization	21

2.7	Polymer Annealing	25
2.7.1	PVD Process and Vacuum Basics	26
2.7.2	Film Morphology and Growth Modes.....	27
2.7.3	Structure Zone Model of Sputter Deposition Materials.	28
2.8	Summary	29
CHAPTER 3: METHODOLOGY		30
3.1	Introduction	30
3.2	Magnetron Used Overview	31
3.3	Electron Drift Analysis	33
3.3.1	Magnetron Operation	35
3.3.2	Cavity Magnetron Operations	37
3.3.2.1	Case 138	
3.3.2.2	Case 238	
3.3.2.3	Case 339	
3.3.2.4	Case 439	
3.3.3	Cavity Magnetron with Active RF Field Operations	40
3.3.3.1	Case 140	
3.3.3.2	Case 241	
3.3.3.3	Case 341	
3.4	Multiphysics Element Analysis Simulation	42
3.4.1	Thermal Stress Module	45
3.4.2	Moving Mesh Module	46
3.4.3	Electromagnetic Waves Module.....	46
3.4.4	Electrostatics AC/DC Module.....	47
3.4.5	Charged Particle Tracing Module	47
3.4.6	Post-Processing Results.....	49

3.5	Annealing Process	50
3.6	Experimental Setup	62
3.7	Summary	66
CHAPTER 4: RESULTS AND DISCUSSION		68
4.1	Introduction	68
4.2	Simulation Results	68
4.3	Annealing Results	71
4.4	Experimental Validation	78
4.5	Analysis and Comparison	84
4.5.1	Comparison with Various Magnetron Rating.....	85
4.5.2	Comparison with Recent Works.....	89
CHAPTER 5: CONCLUSION AND RECOMMENDATION		92
5.1	Conclusions	92
5.2	Novelty and Contribution	94
5.3	Recommendation	94
	References	96
	List of Publications and Papers Presented	110
	APPENDIX A: SCHEMATIC OF ANNEALING DEPOSITION FACILITY	111
	APPENDIX B: COMSOL SIMULATION AT DIFFERENT PARAMETER	112
	APPENDIX C: HIGH POWER CHARGING EFFECT	114
	APPENDIX D: PROTOTYPE TESTING BASED ON PROPOSED SOLUTION	115

LIST OF FIGURES

Figure 1.1: Methodology Flow Chart	6
Figure 2.1: Recent WPT systems: (a) MIT near-field demonstration (Kurs, Karalis, Moffatt, Joannopoulos, Fisher, & Soljačić, 2007); and (b) Managed Energy Technologies, Texas A&M University, University of Kobe 2008 Hawaii MPT setup (Foust, 2008)	9
Figure 2.2: Magnetron principle of operation (Jang, Ahn, et al., 2011)	15
Figure 2.3: Schematic of magnetron equivalent circuit diagram (Oraizi & Afsahi, 2007)	16
Figure 2.4: Microwave power generator performance analysis to a sub-millimeter-wave region state art	18
Figure 2.5: SZM (or Thornton) model for sputter-deposited materials (von Helmholt et al., 1997)	28
Figure 3.1: Methodology Flow Chart	30
Figure 3.2: Parts in Conventional 6kW, 2.45GHz Microwave Heating Sintering Thawing CW type magnetrons.....	32
Figure 3.3: Magnetron cross-section and parts	36
Figure 3.4: Constructional details of a cavity magnetron and the magnetic lines of flux present, axially	37
Figure 3.5: The cross-section of the magnetron with the magnetic field is absent.....	38
Figure 3.6: The cross-section of the magnetron with the magnetic field is present.....	38
Figure 3.7: The Cross-section of the magnetron with the magnetic field is critical	39
Figure 3.8: The cross-section of the magnetron with the excessive magnetic field is present	40
Figure 3.9: (A) Electron movements in different cases, (B) Electron clouds formed	41
Figure 3.10: Magnetron components, a) copper Anode, b) modified cathode and c) non-ideal vacuum interaction region	43
Figure 3.11: 3D Magnetron Mesh Model	44
Figure 3.12: COMSOL simulation steps methodology.....	45

Figure 3.13: Thermal stress steps and procedure	45
Figure 3.14: Moving mesh steps and procedures	46
Figure 3.15: Electromagnetic Waves steps and procedures	47
Figure 3.16: Electrostatics steps and procedures	47
Figure 3.17: Charged Particles Tracing steps and procedures	48
Figure 3.18: PT Interaction and Computational.....	48
Figure 3.19: Electric Force to PT Interaction.....	49
Figure 3.20: Individual steps and procedures superposition.....	50
Figure 3.21: Computational of Post-Processing Results.....	50
Figure 3.22: Conventional magnetron cut-off.....	52
Figure 3.23: Gas flow in an annealing chamber	56
Figure 3.24: Annealing process equipment setup. (a) front view, (b) side view	57
Figure 3.25: Deposition chamber	58
Figure 3.26: Gas tanks	60
Figure 3.27: Gas valve solenoid.....	60
Figure 3.28: Gas distribution lines	62
Figure 3.29: Solenoid valves for Ar and O ₂ lines	62
Figure 3.30: Experimental setup block diagram	63
Figure 3.31: Experimental measurement setup diagram.....	64
Figure 3.32: Diagram of measuring system	65
Figure 3.33: Experimental setup; a) Rectenna, b) Connection to battery	66
Figure 4.1: Heat density scale on magnetron model to generate 5W, 2.45GHz microwave power; a) BaO Substrate coated cathode, b) GaN and SiC Polymer coated cathode	69
Figure 4.2: Resonant EF streamline, a) BaO coated, b) GaN and SiC polymer coated..	70
Figure 4.3: EMC performance analysis (a) Cold condition, (b) Working condition	71

Figure 4.4: GaN substrate, (a) TEM and SAED images, and (b) HRTEM image.....	72
Figure 4.5: SiC substrate, (a) TEM and SAED images, and (b) HRTEM image	73
Figure 4.6: Cluster growth of one-dimensional GaN and SiC Polymer nanostructure of 100nm thickness, (a) XRD 3.00K zoom, (b) XRD 6.00K zoom, and (c) XRD 10.0K zoom	74
Figure 4.7: Samples grown at different temperatures, (a) 850°C, (b) 900°C, and (c) 950°C	75
Figure 4.8: Polymer is grown at different periods, (a) 5 minutes, (b) 10 minutes, (c) 15 minutes, and (d) 20 minutes	76
Figure 4.9: Photoluminescence spectrum of samples ammoniated at different temperatures	77
Figure 4.10: Performance comparison; a) measured output spectrum, b) measured received voltage by battery	80
Figure 4.11: Magnetron temperature during operation	82
Figure 4.12: Magnetron input and output voltage.....	83
Figure 4.13: Heat density scale on magnetron model to generate 5W, 2.45GHz microwave power. a) High Power BaO Magnetron (rated 6kW), b) Lower Power BaO Magnetron (rated 900W), and c) Proposed solution.....	86
Figure 4.14: Magnetron output with 5W, 2.45GHz input. a) High Power BaO Magnetron (rated 6kW), b) Lower Power BaO Magnetron (rated 900W), and c) Proposed solution	88
Figure 4.15: Noise captured by a spectrum analyzer. a) BaO magnetron and b) Proposed solution.....	88

LIST OF TABLES

Table 2.1: Limits of exposure for RF and microwave towards workers from Health Canada “Safety Code 6”, 99-EHD-237 (1999) updated in 2002, August 8.....	12
Table 2.2: Comparison of Microwave Power Generator Performance.....	19
Table 2.3: Summary of Recent Optimization	24
Table 2.4: Vacuum Ranges (in Torr)	27
Table 3.1: Parameters and value of CW Magnetron.....	32
Table 4.1: Experimental Results	79
Table 4.2: Experimental result in three conditions for wireless charging and wired charging applications	84
Table 4.3: Comparative analysis	90

LIST OF SYMBOLS AND ABBREVIATIONS

2D	:	Two-Dimensional
2DEG	:	Two-Dimensional Electron Gases
3D	:	Three-Dimensional
AC	:	Alternating Current
AES	:	Auger Electron Spectroscopy
AFM	:	Atomic Force Microscope
AI	:	Artificial Intelligence
AK	:	Anode-Cathode
AlGaAs	:	Aluminium Gallium Arsenide
Ar	:	Argon Gas
BaO	:	Barrium Oxide
BWO	:	Backward Wave Oscillator
CAD	:	Computer-Aided Design
CCD	:	Charge-Coupled Device
CDG	:	Capacitance Diaphragm
COG	:	Centre Of Gravity
CPT	:	Charged Particle
CW	:	Continuous Wave
DC	:	Direct Current
DE	:	De-ionized
DOE	:	Department Of Energy
DSP	:	Digital Signal Processing
EF	:	Electric Field
EM	:	Electromagnetic

ES	:	Electrostatic
ESCA	:	Electron Spectroscopy For Chemical Analysis
F	:	Force
FCC	:	Face-Centered Cubic
FETs	:	Field-Effect Transistors
FGU	:	Frequency Generating Unit
FLC	:	Fuzzy Logic Control
GaAs	:	Gallium Arsenide
GaAs	:	Gallium Arsenide
GaN	:	Gallium Nitride
G_R	:	Antenna Gain At The Receiver
G_T	:	Antenna Gain At The Transmitter
Gv	:	Gate Valve
HCIG	:	Hot Cathode Ionization
HEMT	:	High Electron Mobility Transistor
HFET	:	Heterojunction Field Effect Transistor
HPA	:	High Power Amplifier
HRTEM	:	High-Resolution Transmission Electron Microscopy
ICNIRP	:	International Commission On Non-Ionizing Radiation Protection
I_{in}	:	Input Current
InP	:	Indium Phosphide
IPA	:	Isopropyl Alcohol
I_{rx}	:	Received Current
j	:	Magnetron Cathode Current Density
JAXA	:	Japan Aerospace Exploration Agency

KALI-5000	:	Kilo Ampere Linear Injector
LeRC	:	Lewis Research Center
LiPo	:	Lithium Polymer
LN ₂	:	Liquid Nitrogen
LOCA	:	Loss Of Coolant Accident
<i>m</i>	:	Constant Electron Mass (9.11×10^{-31} Kg)
MD	:	Molecular Dynamics
mES	:	Minimum Element
MFC	:	Mass Flow Controller
MILAX	:	Microwave Lifted Airplane Experiment
MINIX	:	Microwave Ionosphere Nonlinear Interaction Experiment
MIT	:	Massachusetts Institute Of Technology
MM	:	Moving Mesh
MOSFET	:	Metal Oxide Field Effect Transistor
MP	:	Multiphysics
MPG	:	Microwave Power Generator
MPT	:	Microwave Power Transmission
N ₂	:	Nitrogen Gas
NASA	:	National Aeronautics and Space Administration
NI	:	National Instruments
O ₂	:	Oxygen Gas
OEO	:	Optoelectronic Oscillator
PFPE	:	Perfluorinated Polyether's
<i>P_{in}</i>	:	Input Power
<i>P_{out}</i>	:	Output Power
<i>P_{rx}</i>	:	Received Power

PT	:	Particle Tracing
PVD	:	Physical Vapor Deposition
PWM	:	Pulse Width Modulation
QCM	:	Quartz Crystal Deposition Monitor
r	:	Air Gap Distance Between Transmitter And Receiver
RAMP	:	Raytheon Airborne Microwave Platform
RBS	:	Rutherford Backscattering Spectrometry
RF	:	Radio Frequency
RFIC	:	Radio Frequency Integrated Circuit
RHEED	:	Reflection High-Energy Diffraction
r_{neg}	:	Negative Resistance
SAED	:	Selected Area Electron Diffraction
SAXS	:	Small Angle X-Ray Scattering
SBNR	:	Sideband Noise Ratio
SERT	:	Space Electric Propulsion Test
SHARP	:	Stationary High Altitude Relay Program
SI	:	System Identification
Si	:	Silicon
SiC	:	Silicon Carbide
SIMS	:	Secondary Ion Mass Spectroscopy
SPS	:	Solar Power Satellite
SSP	:	Space Solar Power
STM	:	Scanning Tunnelling
SZM	:	Structure Zone Model
TC	:	Thermal Couple
TCE	:	Trichloroethylene

TDTR	:	Time Domain Thermal Reflectivity
TEM	:	Transmission Electron Spectroscopy
THD	:	Total harmonic Distortion
Torr	:	Pressure Range
TS	:	Thermal Stress
TWT	:	Traveling Wave Tube
TWTA	:	Travelling Wave Tube Amplifier
UHF	:	Ultra-High Frequency
UHF	:	Ultra-High Frequency
V_c	:	Critical Voltage
V_{rx}	:	Received Voltage
VCO	:	Voltage Controlled Oscillator
V_{oc}	:	Hull Potential
WBG	:	Wide Bandgap
Wi-Fi	:	Wireless Fidelity
WPT	:	Wireless Power Transmission
XPS	:	X-ray Photoelectron Spectroscopy
XRD	:	X-ray Diffraction
YIG	:	Yttrium Iron Garnet
Z_{in}	:	Input Impedance

CHAPTER 1: INTRODUCTION

1.1 Research Background

In recent decades, numerous research work has been carried out to optimize microwave power transmission for low power applications such as biomedical, agriculture, industrial, health care wearable, and communications. However, this research work has been critically declining due to its safety concern over environmental setbacks and human health effects. This thesis presents the analysis, simulation, and experimental testbench to verify the proposed solutions in compliance with the health and safety rules and regulations. According to Health Canada guideline "Limit of Human Exposure of Radiofrequency Electromagnetic Energy in the Frequency Range from 3kHz to 300GHz – Safety Code 6 (2015)", humans must not be exposed to Electric field strength, magnetic field strength, and power density in controlled spaces higher than 6.455W for frequency a ranging between 100MHz to 6GHz (Code, 2015). The work in this thesis is carried out inline with the safety limit for future implementation.

There are a few common ways to generate microwave power, including 1) the use of coaxial virtual cathode oscillator using velvet or graphite cathodes (Hu et al., 2018; Ikeda & Itoh, 2018, 2019), 2) the use of backward wave oscillator (Kim et al., 2011; Rostov et al., 2018), 3) through MOSFET magnetic superlattices (Gerling, 1987), 4) through high mobility electron heterojunction (Pengelly et al., 2012), 5) through picosecond optoelectronic technique (Saeed et al., 2018; Vintizenko, 2018; Yang, 2013), and 6) through Magnetron (Brown, 1981; Brown & Eves, 1992; Gold & Nusinovich, 1997). A wide range of selection criteria for the microwave generator is based on applications, safety, power density, temperature produced, efficiency, energy consumption, and reliability. A magnetron is commonly used in industry, or home applications due to its safety-favored protection feature, cost-effectiveness, reliability, availability in the market, and suitability for many applications.

One of the methods used in 2.45GHz-Band 250W, Feedback-type GaN-HFET Oscillator using Imbalanced Coupling Resonator Microwave Generator (Ikeda & Itoh, 2018, 2019) for microwave enhancement is in using circuit design techniques of high-power feedback-type Gallium Nitride Heterojunction Field Effect Transistor (GaN-HFET) oscillator for the microwave oven (Lu, Song, Cheng, et al., 2020). The work focused on the harmonic termination for high-efficiency power amplifiers, the coupling factor to feedback circuits, and the insertion phase adjustment of feedback loops (Ikeda & Itoh, 2019). Thus, the system achieves 61.3% efficiency. In another work (Vyas et al., 2016), a Ferrite material filling is adopted to enhance a Continuous Wave (CW) magnetron. However, the approach is utilized for 10kW CW magnetrons with other resonators partially filled with Yttrium Iron Garnet (YIG). This method increases the saturated efficiency and the output power by 7.25% and 13.75%, respectively, for a filling factor of 33.68% (Vyas et al., 2016). Efficiency enhancement has been conducted in an A6 magnetron with a transparent cathode (Fuks & Schamiloglu, 2005) (Ikeda & Itoh, 2018). The approach is simple, and the application is meant for random voltages. The efficiency of a magnetron is significantly affected by the heat generated by the magnetron cathode. Therefore, a planar-balanced magnetron cathode's cooling effort must sustain the operation under the threshold limit to ensure cathode reliability and process reproducibility, achieved by a proper design technique to enhance heat dissipation generated at the cathode. Reported research progresses in distributing temperature and analyzing the magnetron cathode coolant streamlines velocity through the turbulent model (Gerling, 1987; Gold & Nusinovich, 1997; Pengelly et al., 2012; Vyas et al., 2016). Overall, magnetron enhancement research aims to keep the operating temperature under the threshold limit and improves high heat density performance to enhance heat dissipation.

The Magnetron (Luo et al., 2020; Vyas et al., 2016; Zhu et al., 2020) is a conventional magnetron of 6kW, 2.45GHz Microwave Heating Sintering Thawing (CW) type magnetron. Even though this Magnetron is popular in the market and has been used for decades, a few setbacks exist, such as the correlation between thermionic emission, anode resistance, and pulse temperature rise, which affect the Magnetron's performance and efficiency. Numerous research works have been reported correlating the thermionic emission characteristics with the Magnetron (Canali, Majni, et al., 1975; Christou, 2019; Kalinin et al.). For example, at the Cathode Research Group of Radiation Laboratory, an industrial CW magnetron with a high-power 30kW, 60s warm-up time has been used (Chen et al., 2019; Jang, Ryoo, et al., 2011; Lu, Song, & Huang, 2020).

1.2 Problem Statement

Since microwave generators are expensive and comparatively low-efficiency in a heating application, options other than energy generation are realized from microwave processing. Such results include increased process yield, time savings, and environmental compatibility. A wide range of selection criteria in the microwave generator is based on safety, power density, temperature produced, efficiency, energy consumption, and reliability. A magnetron is commonly used in industry, or home applications due to its safety-favored protection feature, cost-effectiveness, reliability, availability in the market, and suitability for many applications. However, the setback in a magnetron's efficiency is mainly due to the heat from electrons' movement, which leads to a sudden temperature rise (Daimon & Jiang, 2007; Gandhi, 2019; Hu et al., 2018; Ikeda & Itoh, 2018). In the worst-case scenario, the Magnetron loses its stability and triggers a malfunction through the safety protection of the attached thermo-switch.

Thus, the researcher assumes that electron drift velocity control is essential in achieving high efficiency and reliable microwave power generation using a magnetron.

It is explained by the unbalanced magnetic field control, which affects instantaneous power consumed in the plasma, leading to sudden temperature rise. Other influencing parameters exist in the spatial distribution of a high-power impulse magnetron cathode annealing process through a controlled, unbalanced magnetic field (Pengelly et al., 2012).

1.3 Research Scope

The selection of microwave operating frequency ranges from 500MHz to 300GHz or even higher, depending on its applications. A traditional microwave oven uses a cross-field magnetron as its heating element with a wavelength from 1 to 3 cm, commonly using 2.45GHz frequency (Chen, Tang, Deng, et al., 2020; Chen, Tang, Tianhong, et al., 2020). The concept of food heating in a microwave oven depends on the food's frequency absorption rate and the container in use. Heat generation occurs when the microwave intersects at a lower absorption rate material. Numerous research work has been reported on microwave power transmission since Brown's first experimental work. The works which remain to be the highest performance to date is observed through his invention of a flying helicopter with 91% of RF to DC conversion efficiency, 54% for 1kW initial power transmission at 10GHz frequency, and 82.5% for 34kW transmission over a mile for a high-power system conducted at 2.1GHz frequency (Brown, 1977a, 1981; Brown & Eves, 1992). However, such experiments have been backtracked due to regulatory restrictions on high-power microwave exposure limitation.

Polymer annealing on Magnetron's cathode surface using Gallium Nitride (GaN) and Silicon Carbide (SiC) semiconductors is a technique used to enable low microwave power generation in magnetron operation at high frequency in higher efficiency. The conventional Magnetron potentially generates 6kW, 2.45GHz microwave power over a 67% efficiency. However, if the identical conventional Magnetron with a non-annealed cathode was used to generate 5W, 2.45GHz low microwave power, the efficiency drops

significantly to approximately 50%, as shown in the experiment results. Losses occur during the generation and transmission process and hence lower the efficiency of the microwave power transmission system.

Therefore, in compliance with the microwave exposure and limitation restrictions (Code, 2015; Gandhi, 2019), the proposed work operates within the range of 5W microwave power generation at 2.45GHz. This operations range is also selected based on the typical charging rate of standard mobile phones (Kutkut et al., 1995; Lawless & Sparks, 1988; Lu et al., 2015; Nasiri et al., 2009; Orr et al., 1984; Yilmaz & Krein, 2012). This work aims to control the operating temperature to achieve higher efficiency for high frequency and low power levels through the coating material selection of Magnetron's cathode.

1.4 Research Objectives

This work aims to optimize Modulated Microwave Power Transmission by modifying magnetron cathode building materials. Therefore, to achieve this aim, the following objectives are determined as a guide:

- To analyze the Magnetron's cathode electron drift velocity with concerning parameters such as material characteristics, electron mobility, targeted structure size, particle charged and heat dissipated
- To design a high-stability magnetron using GaN and SiC Polymer over BaO Substrate based on the electron drift analysis through simulation
- To design and develop an annealing system from a conventional sputtering facility for polymer growth on a current magnetron cathode with different conditions

- To develop an experimental testbench to validate the modulated microwave power transmission system using annealed magnetron cathode and traditional magnetron cathode
- To benchmark the proposed solutions with existing microwave power generators and similar solutions

1.5 Research Methodology

The methodology in this thesis is carried out based on the flow chart identified as shown in Figure 1.1. The work begins with an analysis to determine the characteristics of each material. Based on the analysis, a simulation is performed in COMSOL to verify the hypothesis.

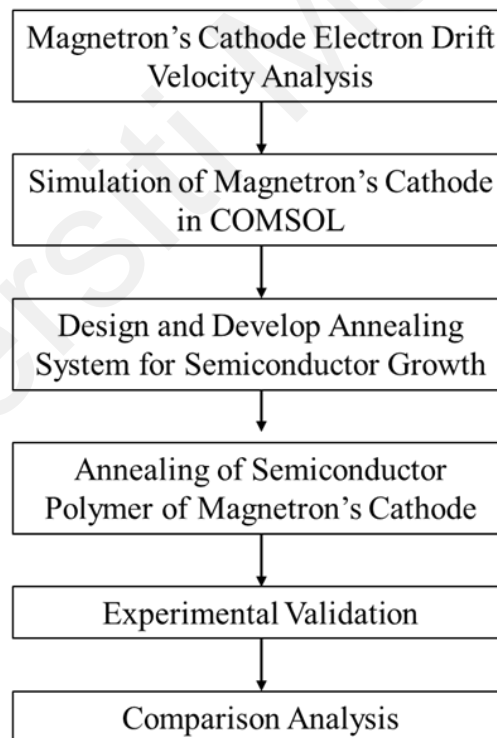


Figure 1.1: Methodology Flow Chart

After obtaining the best simulation results by considering the polymer's thickness on the magnetron cathode surface, an annealing system is designed from a conventional sputtering system to grow a layer of GaN and SiC polymer. An experimental setup in an

anechoic chamber is developed to validate and analyze the microwave power generation limitation. The experimental result is then analyzed and compared with a conventional system and recent work similar to the proposed optimization.

1.6 Thesis Outline

This thesis focuses on High Efficiency, Low Noise Magnetron Cathode using GaN and SiC Polymer over BaO Substrate for Modulated Microwave Power Transmission. After this introductory chapter, the first section of Chapter Two describes a literature review on the brief history of wireless power transmission using a modulated microwave, approaches of magnetron optimization, and semiconductor materials implementation in magnetron optimization.

Chapter Three briefly describes the operation and parts of the Magnetron, the designed annealing system, and the developed experimental setup. This chapter also elaborates on electron drift analysis, simulation, and the annealing system setup.

Chapter Four presents the simulation results in COMSOL, a CAD tool to simulate the model achieving a stable Magnetron using Polymer. Then, extract the comparison over the current substrate magnetron cathode. This chapter also shows the significant contribution of proposed solutions through the experimental validation of annealed magnetron cathode. The proposed results and the reported system performance are compared and analyzed at the end of this chapter.

Conclusions and recommendations for future research are given in Chapter Five.

CHAPTER 2: LITERATURE REVIEW

2.1 Introduction

This chapter consists brief history of recent research regarding microwave power transmission followed by different microwave power generators. Focus is given to the magnetron type and the literature on the annealing process. Reviewing the annealing process is essential to obtain a quality semiconductor deposition process. However, the resources of the annealing review are unpublished industry white papers. Therefore, it only focused on an essential point in the annealing process.

2.2 Current Technology on Microwave Power Transmission

In the last ten years, the number of articles published regarding Solar Space Power (SSP) increasing aggressively. However, complimentary research has been isolated according to scope. The main factor for the termination of activity is the problematic funding limitations. However, there have been a few experiments that are worth discussing. Two of these experiments are John Mankins' Hawaii Microwave Power Transmission (MPT) demonstration (Lee, 2015; Willert-Porada, 2006; Yuen, 2013) and the inductive near-field Work by Soljagic's group at the Massachusetts Institute of Technology (MIT) (Kurs, Karalis, Moffatt, Joannopoulos, Fisher, & Soljagic, 2007).

Reminiscent of Telsa's Work more than 130 years earlier, the 2006 MIT experiment, carried out by physicist Marin Soljagic and his colleagues, involved the inductive near-field coupling of power from a primary AC-excited coil to an awaiting secondary coil located 2 m away (Karalis et al., 2008; Kurs, Karalis, Moffatt, Joannopoulos, Fisher, & Soljačić, 2007). A 60 W light bulb attached to the secondary coil was then successfully lit up, as seen in Figure 2.1 (a). However, MIT researchers quantified the power transfer efficiency of 15%. In addition, the measurable power levels at 10 MHz were 14 times higher than the safety standards issued by International Commission on Non-Ionizing Radiation Protection (ICNIRP)(Protection, 2017; Sliney et al., 2005). Despite these

concerns, MIT researchers identify the work on power induction as a possible way to charge remotely Wireless-Fidelity (Wi-Fi) devices (Kurs, Karalis, Moffatt, Joannopoulos, Fisher, & Soljačić, 2007). This MIT work does not come within the realm of MPT due to its operational frequencies, but it is a Wireless Power Transmission (WPT) experiment worth noting.



(a)

(b)

Figure 2.1: Recent WPT systems: (a) MIT near-field demonstration (Kurs, Karalis, Moffatt, Joannopoulos, Fisher, & Soljačić, 2007); and (b) Managed Energy Technologies, Texas A&M University, University of Kobe 2008 Hawaii MPT setup (Foust, 2008)

The second experiment that has garnered much attention is the Hawaii MPT experiment by John Mankins in 2008 from Managed Energy Technologies in conjunction with A&M University, Texas, in collaboration with Kobe University (Japan). It is worth mentioning that John Mankins is a long-time advocate, having spearheaded the previous Space Electric Propulsion Test (SERT) efforts while at the National Aeronautics and Space Administration (NASA). Discovery Communications is a TV channel (Mankins & Howell, 2000; Patterson & Sovey, 2013; Peterson et al., 2007). The experiment transmits power from the Maui-based array, seen in Figure 2.1 (b), to the main island of Hawaii, over a distance of 148 km (Mankins & Howell, 2000). This length set a new distance record, but the total received power on the main island was less than $1/1000^{\text{th}}$ or 1% of

the total power transmitted from Maui (Strassner & Chang, 2013). This, from an MPT standpoint, is considered by many as a failure. However, the low performance was anticipated because the transmitting and receiving array's size was too small for transmission up to 148km. In other words, massive spillover loss was the setback. The John Mankins' experiment was done on a budget with less than \$1 million, limiting what could be accomplished in all fairness (Henley et al., 2002; Mankins et al., 2012).

Lastly, Japan is keen on developing SSP because of its resource limitations. Japan Aerospace Exploration Agency (JAXA) has begun developing numerous hardware subsystems integrated into a working SPS by 2030 (Blaylock; Kachi et al., 2011; Strassner & Chang, 2013). In the near term, Japanese researchers at the Taiki Multipurpose Aerospace Park in Hokkaido will attempt to use a 2.4m diameter antenna to send microwave power over 50m to a rectenna to operate a household heater (Strassner & Chang, 2013; You et al., 2020). After the experiment has proven successful, the next step is to scale up the 50m distance to 36,000km and the 2.4m antenna to 3km. This scaled-up version would be sufficient to receive 1GW of electricity, which could be enough to power 500,000 homes (Jackson et al., 2010).

Currently, the SSP system warrants the most significant focus on photovoltaic solar cells. In the state-of-the-art solar cell, sunlight to DC efficiency has remained around 30% for decades. The other 70% is predominantly heat loss, which can heat the transmitting aperture, lowering the radiated power. Using quantum dot technology, thin film and improvements in solar cell efficiency are essential before fielding any functioning SSP system. Since MPT/SSP funding over the last decade has been limited, focusing on specific subsystem improvement might make sense before another full-scale MPT test is attempted.

Research on Wireless Power Transmission (WPT) development was carried out by many academic institutions and industries worldwide. There are a few WPT system types: magnetic coupling, resonant, inductive coupled, radio waves, and microwave. These types can be divided into two general classes: short-distance and long-distance power transmission. The short-distance transmission was more popular than long-distance transmission due to its efficiency, lower power losses, and simplicity of system design. However, long-distance power transmission using radiofrequency and microwave was labeled by society as dangerous and harmful to human safety and health if implemented for wirelessly charged mobile phones. Furthermore, the efficiency and power losses during transmission still require optimization before commercialization. Wireless power transmission using the modulated microwave harms human health and damages other electronic circuits nearby due to its Ultra-High Frequency (UHF) characteristics.

As highlighted in Table 2.1, the maximum exposure of microwave frequency stands at less than $50\text{W}/\text{m}^2$. The transmission remains only 5W for standard transmission and 7W for peak transmission. The maximum voltage exposure is 137V for microwave frequencies not more than 6 minutes of exposure. Therefore, this rate is highly safe to be commercialized as the rated voltage was only 3.78V and higher up to 4.5V. However, due to the limitation of magnetic-field strength, the current user is limited to 0.364A with 13.74V transmission. The voltage value can be changed, but with constant magnetic-field strength (0.364A) and must be below 50W.

Table 2.1: Limits of exposure for RF and microwave towards workers from Health Canada “Safety Code 6”, 99-EHD-237 (1999) updated in 2002, August 8

Frequency (MHz)	Electric Field Strength; RMS (V/m)	Magnetic Field Strength; RMS (A/m)	Power Density (W/m ²)	Averaging Time (min)
0.003 – 1	600	4.9	--	6
1 – 10	600/f	4.9/f	--	6
10 – 30	60	4.9/f	--	6
30 – 300	60	0.163	10*	6
300 – 1,9500	3.54f ^{0.5}	0.0094f ^{0.5}	f/30	6
1,500 – 15,000	137	0.364	50	6
15,000 – 150,000	137	0.364	50	616,000/f ^{1.2}
150,000 – 300,000	0.354f ^{0.5}	9.4 x 10 ⁻⁴ f ^{0.5}	3.33 x 10 ⁻⁴	616,000/f ^{1.2}

2.3 Magnetron History

After the 1960s, MPT experiments using microwave tubes were frequently used due to the higher efficiency of the microwave tube compared to semiconductors in high-power amplifiers (HPA) (Treado et al., 1992). Recently, using semiconductor material in HPA produced better efficiency, thus improved by implementing a phased array. However, in point-to-point or short-distance transmission, a microwave tube is still preferable without needing beam development. The choice of using a microwave tube or semiconductor HPA for generating microwaves lies behind the system design and application. Semiconductor's material frequently uses WPT resonant and inductive coupling frequency converters. Specifically, these semiconductors operate at low frequencies in the inverter circuit.

Many types of microwave amplifiers and generators can be used, such as the traveling wave tube (TWT), klystron, traveling wave tube amplifier (TWTA), and the more popular Magnetron (Makishima et al., 1999; Xu et al., 2011). Satellite communications, plasma

heating, and cooking use different types of microwave tubes. These microwave tubes were implemented in MPT at the end of the 1960s.

The Magnetron was discovered in 1921 by A.W. Hull, thus having the most extended history compared to other microwave generators (Hull, 1921; Jepsen & Muller, 1951). Later, in 1928 K. Okabe invented an efficient and practical magnetron that gathered global attention through the proposal by dividing anode type (Caloz et al., 2002; Okabe, 1929; Okawa et al., 2001). During Second World War, the Japanese army improved the magnetron technology for war purposes. Spencer from Raytheon Company, one of the microwave manufacturers in the United States, found the microwave beamed from a radar magnetron melted chocolate kept in his pocket. Since 1952, Raytheon Company has owned the microwave oven patent and started producing ovens (Brown et al., 1966). Since then, Magnetron has had a focused market produced only for microwave ovens.

A magnetron is commonly used to operate at a frequency of 2.45GHz, producing 500 W up to 1,000 W for microwave ovens using a low-cost oscillator for around \$5 each. Magnetron's main construction consists of magnets and metal frames that maintain low cost. The average power produced by Magnetron for every microwave oven exceeds 45.5 GW per annum for net global capacity. The age of magnetron history is the same as the history of microwave ovens. The first oven-using microwave was sold for more than \$2,000 after Second World War in the United States (Levy & Cohn, 1984; Osepchuk, 1984; Skolnik, 2002). Due to the high price of a microwave oven, in 1970, the focus was to reduce Japan's microwave oven production cost. In the late 1970s, Japan successfully manufactured microwave tubes for less than \$30 compared to American ones costing more than \$300. United States manufacturers sold more than 45,000 ovens between \$250 and \$450 per unit in 1970. The Japanese commercialized low-cost ovens at less than \$200 per unit annually. Since then, the sales of the oven have increased significantly for almost

20 years, which exceed 1 million sales after 5 years and 10 million after 10 years (Brown et al., 1966; Hull, 1921; Levy & Cohn, 1984; Okabe, 1929; Osepchuk, 1984). Due to the need for the microwave oven, the Chinese and Korean manufacturers targeted to sell at a lower cost per unit with optimization of other parts in a microwave oven, such as the semiconductor amplifier.

After an in-depth literature review, we found that DC power supply and current filament stabilities are the main components that result in a quality output microwave spectrum for cooker-type Magnetron (Brown, 1973; Dickinson, 1975; Dickinson & Brown, 1975). However, to produce an adequate, pure, and quiet spectrum for MPT in low and high frequencies, a stabilized DC power supply must be supplied to the filament current and Magnetron after stable oscillation. Therefore, the magnetron Q-factor after the DC power supply stabilized is 1.1×10^5 . Higher harmonic's peak levels were less than -60dBc while other spurious radiations were less than -100dBc. A common problem in a microwave oven is the frequency shift due to the impossibility of frequency/phase control and magnetron heating. This problem still occurred even when the spurious radiation was suppressed.

Frequency shift issues due to phase/frequency impossibility control and magnetron heating still occurred after spurious radiation was overcome. Dr. Brown led the technologies implemented in magnetrons and constructed an amplifier for Magnetron (Brown, 1973; Dickinson, 1975) in which phase/frequency was controllable and stabilized. The magnetron amplifier is adopted with an injection locking and feedback loop. Dr. Brown also suggested that the magnetron amplifier can be applied to MPT and solar power satellites (SPS) (Glaser, 1992; Mankins et al., 2012; Sasaki et al., 2007).

2.4 Basic of Magnetron

Magnetrons, also known as M-type devices or crossed-field tubes, generate high-power microwaves. In the system, the DC magnetic field plays a prominent role in radio-frequency (RF) interaction, and the DC electric fields are perpendicular to each other. Crossed field magnetron refers to the microwave power generator that needs magnetic and electrical fields to intersect at the right angles in the interaction space between the anode and cathode (Jang, Ahn, et al., 2011; Surducan et al., 2011; Vintizenko, 2014). Figure 2.2 illustrates Magnetron's sketched top view illustration, which includes a cylindrical cathode of finite length and radius from the center surrounded by a cylindrical anode. The electron path represents an anode with several re-entrant cavities equispaced around the circumference. These electron-carrying cavities are connected between the cathode and anode by channels. The DC voltage V_0 is supplied between an anode and a cathode.

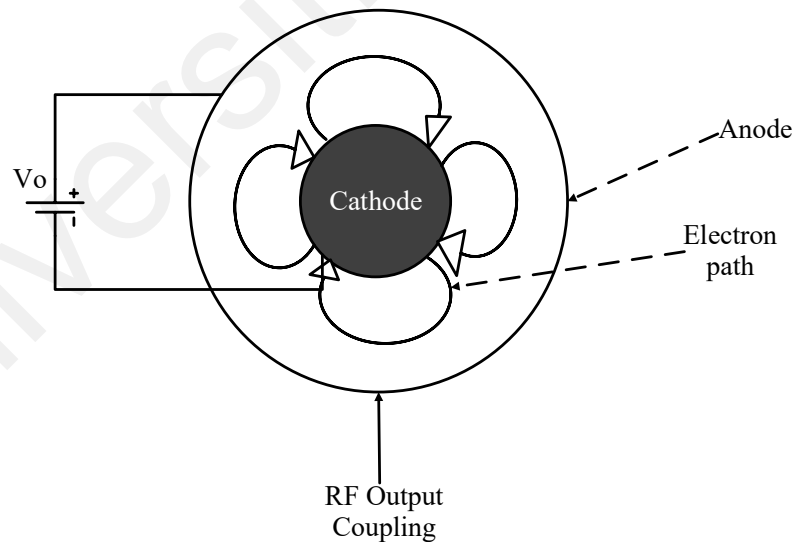


Figure 2.2: Magnetron principle of operation (Jang, Ahn, et al., 2011)

The magnetic flux and supplied DC voltage should be synchronized under combined forces to allow the emerged electrons to follow through the cycloid electron path between the anode and cathode areas and maintain the electron path under balanced magnetic and

electric field strengths. The following equation presents the relation between DC voltage and magnetic flux density:

$$V_{OC} = \frac{e}{8m} \times B_0^2 b^2 \left(1 - \frac{a^2}{b^2}\right)^2 \quad (2.1)$$

B_0 represents the magnetic-field density in webers per square meter (Wb/m^2), a is the cathode radius in meters, b is the anode radius in meters, and m is the constant electron mass (9.11×10^{-31} kg). When the equation is applied in a vacuum, the cathode produces an electron space charged by thermionic emission. Assuming that the magnetic field (B) is constant and critical voltage known as Hull potential (V_{oc}) measured in Volts initiates magnetron operation (Mohamadzade & Afsahi, 2017; Oraizi & Afsahi, 2007). Therefore, magnetron operation depends on the Hull potential. When an electron is infused into an electric field, it is stimulated and flows in orbit. However, if the perpendicular magnetic fields exist, the electron moves in a circle (electron path). The space-charge electron cloud may consistently move along the circle path if the cathode and anode are precisely arranged. This mechanism is known as a planar magnetron. Anodes can be categorized into 1) hole-and-slot blocks, 2) regular-trapezoidal blocks, and 3) rising sun blocks.

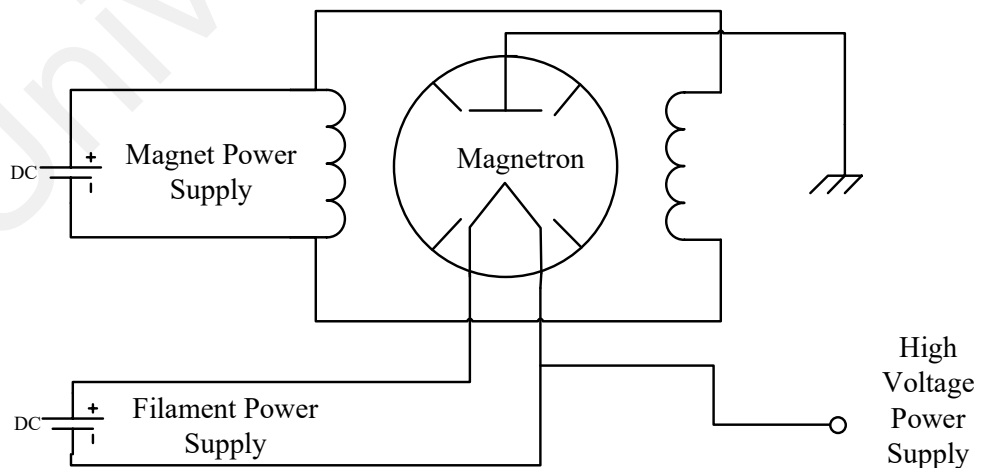


Figure 2.3: Schematic of magnetron equivalent circuit diagram (Oraizi & Afsahi, 2007)

Figure 2.3 shows the equivalent circuit represented as an electronic circuit. The anode is linked to a magnet power source, whereas the cathode is linked to a filament power source. This combination of the two power supplies propagates microwave power from the Magnetron. An antenna or waveguide is needed to control beam propagation direction and transmit microwave power from the Magnetron.

2.5 Types of Microwave Power Generators

There are three main types of microwave power generators defined in the market. However, more evolution magnetron is available, derived from these three main types. The selection of a magnetron depends on its application and implementation.

Magnetron can produce 4000V, 1,200W at a frequency 2.45GHz with 75% magnetron efficiency. However, the optimum operation for a conventional magnetron is at 800V, producing a minimum of 100W to 1,200W with varying energy from 1% to 100%. Therefore, the magnetron is categorized as a medium microwave power generator.

Meanwhile, a coaxial virtual cathode oscillator uses velvet cathodes, and graphite is an extreme high-power microwave generator. The maximum output of this generator is up to 350kV, 25kA, and 100ns, while the current density is up to a few hundred of an ampere per centimeter square. Setting the anode-cathode (AK) gap to 15mm, the system can produce up to 306kV and 20.55kA. However, no high-power microwave is generated for below 300kV and 19kA supply for graphite cathode cases. At the same time, a velvet cathode is the best as it can generate high microwave power with a supply of more than 245kV and 17kA. Therefore, a high-power microwave can be generated using polymer velvet elements as the cathode compared to graphite elements (Kurs, Karalis, Moffatt, Joannopoulos, Fisher, & Soljačić, 2007; Littlejohn, 2013; Matsumoto, 2002; Strassner & Chang, 2013; Surducan et al., 2011; Vintizenko, 2014).

A backward wave oscillator is a popular high-power microwave generator. The output depends on the voltage pulse injected into the Helix consisting of the REB diode and vacuum tube. However, the work is in a limited range of frequency only. The backward wave oscillator can produce up to 230kV, 2kA at 8GHz with a rated power of 2MW using a voltage pulse.

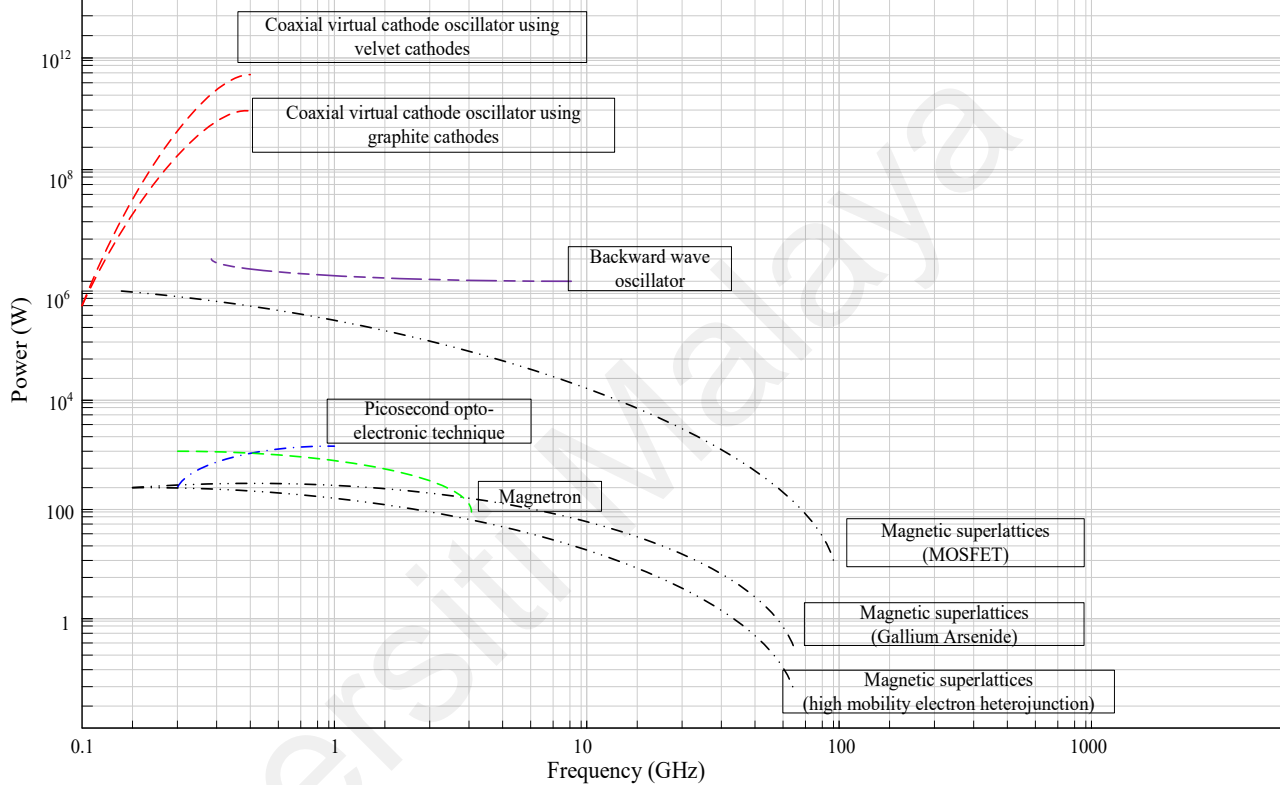


Figure 2.4: Microwave power generator performance analysis to a sub-millimeter-wave region state art

Figure 2.4 clearly shows each microwave power generator's performance and comparison. State-of-the-art shows that magnetic superlattices microwave power generators use the MOSFET element as the hall's ability to perform on a broader range in terms of frequency and microwave power generated. The MOSFET's excellent performance has attracted much more attention due to its high electron mobility and low electron-effective mass. Heat is also one of the critical components that should be considered for stability analysis when involving wireless power transmission. The

stability of super junction MOSFET has been proven when MOSFET can work for at least a maximum temperature of 125°C and as low as -40°C.

Table 2.2: Comparison of Microwave Power Generator Performance

Approach	Magnetron	Magnetic Superlattices			Coaxial virtual Cathode Oscillator		Picosecond Opto-Electronic Technique		Backward Wave Oscillator
		AlGaAs	High Mobility GaAs	MOSFET	Velvet Cathodes	Graphite Cathodes	GaAs	Si	
Basis	-								-
Frequency	300MHz - 4GHz	200MHz - 75GHz	200MHz - 75GHz	100MHz - 100GHz	100MHz - 500MHz		300MHz - 1GHz		300MHz - 8GHz
Peak Power	1,200W	6.4W	0.34W	105W	7,488MW	6,273MW	7kW		460MW
Average Power	700W	570nW	30nW	70W	4,165MW	6,000MW	6.4kW		2MW
Gain	50dB	13dB	13dB	55dB	55dB to 85dB		5dB	20dB	50dB

Table 2.2 shows the comparison of the performance of MPGs discussed in Chapter 2. The elements recommended in Hall's bars and methods to improve MPG performance are discussed. Materials currently considered for Hall's bar production include gallium nitride (GaN) and silicon carbide (SiC), whose development and application have significantly progressed in recent years. These semiconductor materials can operate at high-power densities, temperatures, frequencies, and voltages (Jiang et al., 1995; Kovalchuk et al., 2010; Moller et al., 2009; Sung et al., 2005), thereby conferring them considerable potential for use in future electronic systems, such as switching and radio RF power applications. These materials are interesting, particularly to designers, because the wide-band-gap devices exhibit massive performance compared with Si-based devices. However, whether GaN or SiC is the most feasible and preferred for use in RF power and multiple switching applications remain unclear (Arjavalingham et al., 1989; Frankel et al., 1994; Hung et al., 1989; Knox et al., 1989; Lee, 1990; Qian & Yamashita, 1991; Sayadian et al., 1989). Most researchers believe that GaN and SiC play significant roles, but each semiconductor device performs better in its niche.

GaN-based wide-band-gap semiconductor devices present the following advantages: high dielectric breakdown voltage, electron velocity saturation, and electron sheet concentration because of the heterojunction architecture of GaN/AlGa_N, which is substantial to a high-frequency, high-voltage, and high-output power transistor. GaN field-effect transistors (FETs) on a semi-insulating SiC substrate have been produced and used commercially for amplifiers for mobile and cellular communication base stations (Fischer et al., 1984; Gui-Ming et al., 2013; Lee et al., 2014; Prati & Fanciulli, 2008; Schubert & Ploog, 1984). However, SiC substrates in the market are expensive and thus do not reduce cost due to small-sized substrates. Thereby, reducing the cost of SiC substrates is necessary to facilitate the extensive use of GaN FETs. These semiconductors can significantly contribute to the development of MPGs because they can enhance microwave power.

Outstanding GaN semiconductor material by high breakdown voltages was implemented in GaN/AlGa_N based (Oka et al., 2014; Raskin et al., 1998; Takenaka et al., 2014). The advantage is that the polarization charge at the heterointerface produces a higher density than GaAs. A standard HEMT heterojunction or high-mobility 2DEG is used in magnetrons to reduce one state's resistance. Even so, flanking GaN semiconductor materials exhibit the limits, such as most flanking GaN transistors' threshold voltage being too low for usage for high-power purposes. The threshold voltage of about 3V to 5V is more appropriate to avoid failure operation generated by disturbance (Florian et al., 2014; King & Brazil, 2012; Schnieder et al., 2013; Xu et al., 2014).

2.5.1 Negative Resistance Type

The split-anode, negative-resistance magnetron is a variation of the basic magnetron, which operates at a higher frequency. The negative-resistance magnetron is capable of greater power output than the basic magnetron. Its general construction is similar to the

basic magnetron, except it has a split plate. These half plates are operated at different potentials to provide an electron motion. The electron leaving the cathode and progressing toward the high-potential plate is deflected by the magnetic field and follows the path. After passing the split between the two plates, the electron enters the electrostatic field set up by the lower-potential plate (Bräuer et al., 2010; Hull, 1921; Musil et al., 2005).

The negative resistance between two anode segments is used. This magnetron has low efficiency and is used for specific applications only. They are used at low frequencies below 500MHz (Arnell & Kelly, 1999; Schiller et al., 1993).

2.5.2 Cyclotron Frequency Magnetrons

The negative resistance magnetrons make use of negative resistance between two anode segments. In contrast, cyclotron frequency magnetrons depend upon synchronism amid an alternating electric field component and periodic oscillation of electrons in a direction parallel to this field. Cavity-type magnetrons depend upon the interface of electrons with a rotating electromagnetic field of constant angular velocity. The oscillating electrons and synchronism between the electric component are taken into account. Valid for frequencies higher than 100MHz (Bollen et al., 1990; Van Dyck Jr et al., 1977).

2.6 Magnetron Optimization

A few popular approaches in optimizing the Magnetron to enhance its efficiency include selecting the building materials, increasing the resonant cavity, enlarging operation space size, modifying the anode structure, and implementing solid-state circuits.

For over a century, the material selection for semiconductors played an important role in power devices. Lately, GaN has shown the potential to replace Si-based

semiconductors for high-frequency DC-DC conversion, power transistors in industrial automation, motor drives, and other similar applications. GaN is superior to Si in its inherent wide-bandgap (WBG) characteristic (Kaminski & Hilt, 2012; Lu, Song, & Huang, 2020; Sun et al., 2020; W. Wang et al., 2020). Si's bandgap energy is 11eV, compared to 3.4eV for GaN. The lower energy of GaN in power transistors gives a lower gate capacitance and output capacitance achieving higher switching efficiency, reflecting lower conduction and switching losses with zero/low reverse recovery losses. Other works (Kaminski & Hilt, 2012; Pengelly et al., 2012; Xu et al., 2019) reported using WBG semiconductors, notably Silicon Carbide (SiC), with 3.3eV bandgap energy. However, GaN has the advantage of being widely adopted for high-performance power applications up to about 200V and 50A.

In addition, there are another few general approaches reported in achieving high efficiency and low power microwave generation in recent research involving semiconductors in microwave generators. As such is the ultra-wideband microwave generator using a low-energy-triggered bulk with the implementation of Gallium Arsenide (GaAs) avalanche semiconductor switchable to achieve ultrafast switching period as low as ~200ps (Howes & Morgan, 1985; Hu et al., 2014; Miller, 1981; Wada & Tomizawa, 1988). Also reported is the Silicon (Si) photonic integrated solution into an optoelectronic oscillator (OEO) for frequency-tunable microwave generation. The OEO developed from Si performs better with a high-resistivity metallic micro-heater and is thermally tunable (Cheney, 2011; Maleki, 2011; Yao & Maleki, 1996, 2000). The solid-state device approach oscillates at a low-power microwave output of 210W, 2.45GHz, with an efficiency of 51%.

Furthermore, it is reported that the solid-state injection-locked oscillator has a longer life, and lower voltage operation, with tunable phase and frequency (Boot & Randall,

1976; Lee & Wang, 2009; Tiebout, 2004). Thus, the researcher assumes that electron drift velocity control is essential for achieving high efficiency and reliable microwave power generation using a magnetron. It is explained by the unbalanced magnetic field control, which affects instantaneous power consumed in the plasma, leading to sudden temperature rise.

One of the methods used in 2.45GHz-Band 250W, Feedback-type GaN-HFET Oscillator using Imbalanced Coupling Resonator Microwave Generator (Cheney, 2011; Ikeda & Itoh, 2018; O'Neill, 2007) for microwave enhancement is in using circuit design techniques of high-power feedback-type Gallium Nitride Heterojunction Field Effect Transistor (GaN-HFET) oscillator for the microwave oven (Brown, 1977b; O'Neill, 2007). The Work focused on the harmonic termination for a high-efficiency power amplifier, the coupling factor to feedback circuits, and the insertion phase adjustment of feedback loops (Dickinson & Brown, 1975). Thus, the system achieves 61.3% efficiency. In another work (Brown, 1980), a Ferrite material filling is adopted to enhance a Continuous Wave (CW) magnetron. However, the approach is utilized for 10kW CW magnetrons with other resonators partially filled with Yttrium Iron Garnet (YIG). This method increased the saturated efficiency and the output power by 7.25% and 13.75%, respectively, for a filling factor of 33.68% (Zhang et al., 2009).

Efficiency enhancement has been conducted in an A6 magnetron with a transparent cathode (Fuks & Schamiloglu, 2005; O'Neill, 2007). The approach is simple, and the application is meant for random voltages (Schlesak et al., 1985). The efficiency of a magnetron is significantly affected by the heat generated by the magnetron cathode. Therefore, a planar-balanced magnetron cathode's cooling effort must sustain the operation under the threshold limit to ensure cathode reliability and process reproducibility, achieved by a proper design technique to enhance heat dissipation

generated at the cathode. Reported research progresses in distributing temperature and analyzing the magnetron cathode coolant streamlines velocity through the turbulent model (Boot & Randall, 1976; Brown et al., 1963; Brown, 1973, 1980; Goubau & Schwering, 1961). Overall, magnetron enhancement research aims to keep the temperature under the threshold limit and improve high heat density performance to enhance heat dissipation.

Table 2.3 summarize the recent optimization carried out by other researcher and its efficiency within a similar operating range. The table also detailed the conventional CW magnetron before implementing with proposed solutions. The summary recorded the highest generator efficiency using a TWT at 74%. However, the efficiency recorded is microwave generation at 3.4GHz to 4.2GHz with 150W. In Table 2.1, the operating parameter should not be exposed due to critically exceeding the permitted limit. Therefore, such high-efficiency generators are only applicable in closed-environment operations.

Table 2.3: Summary of Recent Optimization

Generator model and type	Reference	Frequency	Power	Efficiency
CK-625, 6kW, 2.45GHz Microwave Heating Sintering Thawing Continuous-Wave (CW) magnetron – BaO coated magnetron cathode	Conventional (before implementation)	2.45GHz	5W	51.8% (Generator) 18.6% (System)
New BLF6G10, Dual microwave generator (Surducan & Surducan, 2013)	Vasile Surducan and Emanoil Surducan (2013)	905MHz to 918MHz	1.5W to 60W	44.7% to 45% (Generator)
Water-cooled CW CK-2091 magnetrons (Liu et al., 2018)	Zhenlong Liu, Xiaojie Chen (2019)	2,110MHz	500kW	48% (Generator)

2.45GHz-Band Feedback-type Oscillator using Coupling Microwave Generator (Ikeda & Itoh, 2019)	250W, GaN-HFET Imbalanced Resonator	Hikaru Ikeda and Yasushi Itoh (2019)	2.45GHz	5W to 263W	61.3% (Generator)
Traveling-wave tube for the communication "Symphonie" (Bretting & Klein, 1969)	satellite	J. Bretting and W. Klein (1969)	3.7GHz – 4.2GHz	12W	38% (System)
Thales 150 W C-Band radiation-cooled Travelling Wave Tube (Dürr et al., 2015)		W. Dilrr, C. Dilrr, P. Ehret, E. Bosch (Thales Electronics (2015)	3.4GHz – 4.2GHz	150W	74% (Generator)

2.7 Polymer Annealing

Fundamental knowledge of annealing technology and gas dynamics is required to design decisions while developing the system. The literature surveyed pertains to Physical Vapor Deposition (PVD) processes and essential vacuum technologies for a single magnetron sputtering system (Mahan, 2000; Mattox, 2010). Additional literature is provided relating to the quality and fabrication of thin films. This information is aided in selecting components and decisions regarding design, analysis, and determining an adequate range for operating parameters (Helmersson et al., 2006; Mattox, 2002; Sproul, 1996).

Research on polymer, especially GaN on SiC for power devices implementation, started in late 2012 in a high electron-mobility transistor, which has proven to increase its efficiency and lower production cost significantly (Gunaydin et al., 2022; Pengelly et al., 2012). Other research by (Jorudas et al., 2020; Pengelly et al., 2012; Yang et al., 2022) has indicated that implementing power devices with polymer material contributes to

lower power quality noise. While in work by (Jindal et al., 2022; Wu et al., 2022; Ye et al., 2022), proven usage of power devices is popular among microwave devices because of its high saturated electron velocity and wide bandgap. It is also claimed that this solution contributes to better power quality in a high-power application (Hult et al., 2022; Yu, 2022). Therefore it can be estimated from the literature review to support the work in this thesis that implementing GaN on SiC provides better performance.

2.7.1 PVD Process and Vacuum Basics

Physical Vapor Deposition (PVD) produces a thin film. The processes are atomistic deposition processes in which material is vaporized from a solid or liquid source in the form of atoms or molecules, transported in the form of vapor through a vacuum or low-pressure gaseous environment to the substrate where it condenses (*CW Magnetron Sintering Thawing Datasheet*, 2015; Surducan et al., 2011; Vyas et al., 2016). There are several forms of PVD processing. Some main ones are ion plating, vacuum evaporation, and sputter deposition.

These PVD processes are conducted in a vacuum or low-pressure gaseous environment (Helmersson et al., 2006; Mattox, 2002, 2010; Pellish et al., 2010). A vacuum environment consists of a chamber and a pumping system to evacuate the chamber in the most basic sense. Additional components, such as equipment to manipulate samples and a gas injection system within the chamber, are also required for PVD processes. Depending on the process used, the degree of vacuum required can fall into one of the several ranges, as in Table 2.4.

Table 2.4: Vacuum Ranges (in Torr)

Degree of Vacuum	Pressure Range (Torr)
Low	$750 > P > 25$
Medium	$25 \geq P \geq 7.5 \times 10^{-1}$
High	$7.5 \times 10^{-4} \geq P \geq 7.5 \times 10^{-5}$
Very High	$7.5 \times 10^{-7} \geq P \geq 7.5 \times 10^{-8}$
Ultra-High	$7.5 \times 10^{-10} \geq P \geq 7.5 \times 10^{-11}$
Extreme High	$7.5 \times 10^{-13} > P$

The system operates in the medium vacuum range for film fabrication while achieving an ultimate base pressure, or the highest attainable pressure possible, in the very high-vacuum range.

There are several reasons film fabrication is performed at reduced pressure. For instance, a low-pressure environment provides a long mean free path for collision between the source of the material and the location upon which the particles are deposited (*CW Magnetron Sintering Thawing Datasheet*, 2015; Surducan et al., 2011; Vyas et al., 2016). More importantly, the vacuum environment allows for controlling and minimizing contaminants in a given system.

A contaminant can be defined as any material in the ambient or on the surface that interferes with the film formation process, affects the film properties, or influences the film stability in an undesirable way (Han et al., 2020; Walton et al., 2016; Zhang et al., 2018). The effect of a contaminant depends on its concentration and location type; it is a gaseous impurity, adsorbed water vapor, and debris. In addition, contamination can be an unknown variable that hinders the deposition process's reliability or reproducibility.

2.7.2 Film Morphology and Growth Modes

The surface morphology is the nature and degree of surface roughness (Pellish et al., 2010; Somekh, 1984; Walton et al., 2016; Zhang et al., 2018). The primary factors that affect film morphology and the morphology of films are illustrated in the Structure Zone

Model (SZM) for sputter-deposited films (Cheung et al., 1968). It is widely known as the Thornton Model (Cheung et al., 1969).

2.7.3 Structure Zone Model of Sputter Deposition Materials.

As shown in Figure 2.5, film morphology can be categorized into one of four growth modes or regimes. These growth modes are most heavily dependent on the working gas pressure and substrate temperature ratio as the sputtered material's melting temperature (Das et al., 2011). The underlying reasons for these direct dependencies varied by growth mode.

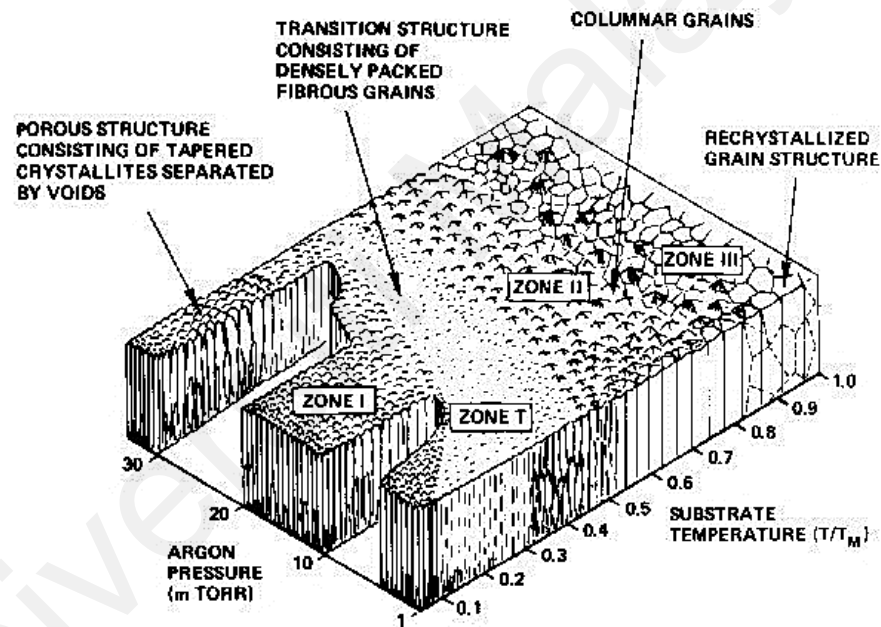


Figure 2.5: SZM (or Thornton) model for sputter-deposited materials (von Helmolt et al., 1997)

The four growth modes are named: Zone 1, Zone T, Zone 2, and Zone 3. Zone T is an intermediate growth mode found between Zone 1 and Zone 2 in plasma annealing and ion plating (Tanaka & Sato, 2007). These molecular dynamics (MD) zones were each associated with conditions where the physics of coating growth was dominated by a particular mechanism (English & MacElroy, 2003; Pellish et al., 2010). The mechanisms for the respective zones are 1) Atomic shadowing during transport, 2) surface diffusion,

and 3) bulk diffusion. Zone T is unique and is affected by several parameters, the most obvious of which is energetic bombardment.

2.8 Summary

This Chapter has detailed the type of magnetron, magnetron operation, and recent optimization carried out on magnetron optimization. There are a few popular optimizations that can be performed on a magnetron. However, the optimization is subject to application to be implemented. This work focuses on optimization by annealing the magnetron's cathode using GaN and SiC polymer to replace conventional BaO. Therefore, annealing is used to grow a polymer layer on the magnetron's cathode surface due to its uniformity of sputtering compared to other methods, such as PVD. This research chooses a magnetron due to its wide operating power range and optimization chances using new semiconductor plasma such as GaN and SiC through a sputtering process. Therefore to verify that the research is valid, some comparison of different semiconductor characteristics and performance in a different microwave power generator was also made.

CHAPTER 3: METHODOLOGY

3.1 Introduction

The proposed solutions to implement annealed GaN and SiC polymer started with an analysis followed by simulation using COMSOL by imitating the Magnetron structure used for this experiment. The correct parameters of the semiconductor deposition obtained from analysis and simulation are then used to prepare the magnetron cathode for annealing. Next, the GaN and SiC polymers are grown on a magnetron cathode surface through an annealing process using a modified sputtering system. Finally, experimental validation is performed using the annealed magnetron cathode for traditional and modified magnetron cathode.

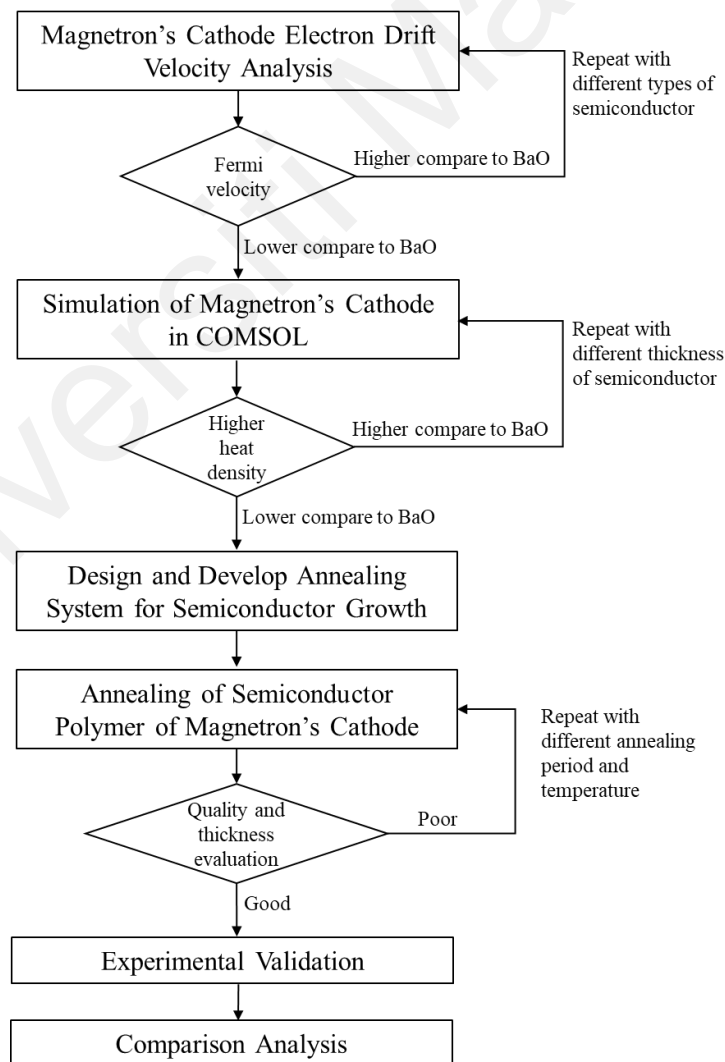


Figure 3.1: Methodology Flow Chart

Figure 3.1 shows the process flow for this thesis methodology which starts from performing analysis on Magnetron's cathode on the possibilities for proposed solutions using Electron Drift Analysis. If the analysis shows positive results, it proceeds with simulation in COMSOL with the same parameters used in the analysis for different semiconductors. Magnetron's cathode is prepared based on the proposed solutions, and an annealing system is modified, designed, and developed from a conventional sputtering system to grow semiconductors on Magnetron's cathode surface. A few annealing trials are performed to determine the best semiconductor growth purity and success rate results. The annealed Magnetron's cathode is then assembled to Magnetron for testing. Experimental validation is carried out for a complete setup of microwave power transmission systems, including microwave generation, transmission, receiver, and energy harvesting. The result is then analyzed and compared with a traditional magnetron and similar solutions.

3.2 Magnetron Used Overview

A 6kW, 2.45GHz rated continuous wave (CW) sintering thawing type magnetron with model number CK-625 is used in this experiment. The Magnetron is attached to a metal-ceramic and a water-cooling system with an integrated RF filter for industrial microwave heating applications. This model of the Magnetron is known for its rapid-heating cathode, high efficiency, and required output power. The Magnetron's cathode is made from Barium Oxide (BaO) material, whereas GaN and SiC are categorized as polymer semiconductors. The technique used in this work is to grow a 100nm thick polymer layer of GaN and SiC combination on the magnetron cathode surface in a dedicated experiment. This thickness is chosen based on the simulation results and supported by an entire growth semiconductor polymer during annealing examined in XRD. Further analysis and comparison during low-power microwave generation were executed. Other defining parts of the Magnetron remain constant.

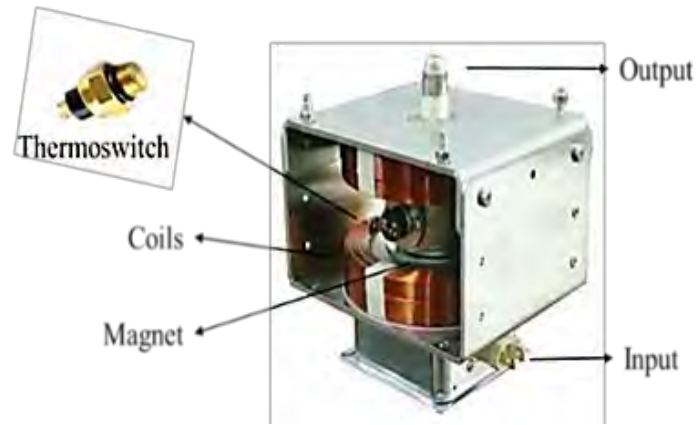


Figure 3.2: Parts in Conventional 6kW, 2.45GHz Microwave Heating Sintering Thawing CW type magnetrons

The Magnetron shown in Figure 3.2 is equipped with Hella Thermo-switch with part number 1MT-372294-851 (FC3722) (*CW Magnetron Sintering Thawing Datasheet*, 2015) sensing temperature maximum up to 180°C. The thermo-switch consists of a pair of bimetallic discs with different thermal expansion coefficients, and the disc is precisely calibrated to snap at 65°C. The deformation causes the pin displacement that closes and opens the silver contacts. This sensor is used to activate the cooling system of the Magnetron. Table 3.1 details the magnetron information used for the experiment.

Table 3.1: Parameters and value of CW Magnetron

Parameters	Value
Frequency Range	0.5 – 75 GHz
Efficiency	40 – 70 %
Range of anode voltage (V_0)	10 – 100 kV
Anode current (I_0)	10 – 100A
Cross-magnetic field (B_0)	10 – 500 mWb/m ²
Duty Cycle	0.1%
Power Output	Over 250 kW (Pulsed mode) 10 mW (UHF Band) 2 mW (X Band) 8 kW (at 95 GHz)

3.3 Electron Drift Analysis

The objective of this annealing is mainly to control the drift motion of electrons by E (electric field) x B (magnetic field) interaction space between the cathode filament and anode. Drift motion is scientifically referred to as the particle drift velocity, such as an electron. Electrons propagate freely on the Magnetron's cathode surface during microwave power generation at Fermi velocity. In this case, the average velocity of an electron is known as drift velocity, which results in a semiconductor due to the existing electric field (Canali, Jacoboni, et al., 1975; Canali, Majni, et al., 1975; Yoshino et al., 1976). Scientifically, the drift velocity refers to axial drift velocity. Therefore, respective to the Fermi concept, the electron propagates freely in a semiconductor at the Fermi velocity as mentioned above. When a small electric field is applied to a magnetron, the electron flows in random motion on the Magnetron's cathode surface due to two main carrier mechanisms: ionized impurity scattering and lattice scattering. By referring to elementary Ohm's law, which states that current is proportional to the electron drift velocity subjected to material resistive, expressed as:

$$u = \mu E \quad (3.1)$$

where u refers to the drift velocity, μ is the electron mobility (in $m^2/(V.s)$) of semiconductors in this experiment (GaN and SiC), and E is the electric field in this Work referred to as the microwave power generated. However, the annealing of these semiconductors covers a sizeable cross-sectional area on the Magnetron's cathode surface. The dimension of the Magnetron's cathode needs to be considered, 80mm in length and 25mm in diameter (*CW Magnetron Sintering Thawing Datasheet*, 2015). Therefore, the drift velocity of the charge in a magnetron's cathode surface with a constant cross-sectional is given as follows:

$$u = \frac{j}{nq} \quad (3.2)$$

In this extended drift velocity equation, j represents the current density flowing through the Magnetron's cathode, n is the number of charge-carrier density, and q is the charge associated with the change in carrier (Canali, Jacoboni, et al., 1975; Jacoboni et al., 1981). For example, by considering the properties of cylindrical current-carrying metallic ohmic semiconductor, with the charge-carrier of the electron, the drift velocity is expressed as:

$$u = \frac{m\sigma\Delta v}{\rho_{\text{eff}}} \quad (3.3)$$

where m represents the semiconductor molecular mass in kg, σ is the electric conductivity in s/m, Δv is the voltage applied in V, ρ is the conductor density in kgm^{-3} , e is the elementary charge in C, f is the free electron number, and l is the conductor length in m. The drift velocity, u is elevated by substituting the properties and parameters for each material, of GaN and SiC polymer, and BaO substrate (represent conventional Magnetron), with Gallium (Ga) for GaN, sputtered Magnetron, and Silicon (Si) for SiC sputtered Magnetron (Canali, Majni, et al., 1975; Canali et al., 1971; Houston & Evans, 1977). However, the drift velocity computation in equation (3.2) is not applicable for an oxide base, including BaO magnetron's cathode, as semiconductor materials are not accounted for. This prohibition was strengthened by electricity commonly conducted in a copper wire. Magnetron's cathode, made from oxide-based material, has a density of 8.94g/cm^3 and an atomic weight of 63.546g/mol with a total of $140,685.5\text{mol/m}^3$. Therefore, in a 80mm thickness, the magnetron's cathode has about 6.8×10^{27} atoms $((6.02 \times 10^{23} \times 140,685.5\text{mol/m}^3) \times 0.08\text{m})$. The reason is that copper base magnetron's cathode has one free electron per atom; n equals 6.8×10^{27} . By substituting the parameter to the drift velocity equation for BaO:

$$u = \frac{I}{nAq} \quad (3.4)$$

$$= \frac{1c/s}{(6.8 \times 10^{27} \text{m})^3 (3.14 \times 10^{-6} \text{m}^2) (1.6 \times 10^{-9} \text{c})}$$

$$= 2.3 \times 10^{-5} \text{m/s}$$

In addition, by considering the cross-sectional shape of the Magnetron's cathode, the equation is further derived from being:

$$u = \frac{A}{\frac{\text{electron}}{\text{m}^3} \cdot \text{m}^2 \cdot \frac{\text{c}}{\text{electron}}} \quad (3.5)$$

$$\frac{\frac{\text{c}}{\text{s}}}{\frac{1}{\text{m}} \cdot \text{c}} = \frac{\text{m}}{\text{s}}$$

The electron for BaO in the Magnetron's cathode flows at the rate of $2.3 \times 10^{-5} \text{m/s}$ with a constant AC supply of 60Hz. Therefore, the electron drift is less than $2 \times 10^{-7} \mu\text{m}$ below the half cycle. Considering the entire cross-sectional area parameter in (3.5) (*CW Magnetron Sintering Thawing Datasheet*, 2015), including the operating temperature in electron, the Fermi flow velocity (Hwang et al., 2012; Ni et al., 2008; Zhou et al., 2003) is computed as 1,570,000m/s for BaO and 854,000m/s for GaN and SiC polymer.

3.3.1 Magnetron Operation

The Magnetron operates similarly to a traditional television Cathode-ray (electron) tube. Electrons are produced by the cathode when a magnetron is powered up and beamed across operation space (Martin et al., 2001; Yang, 2013). The anode with slot cuts is a resonant cavity, illustrated in Figure 3.3. A strong magnet is located underneath the anode to generate a magnetic field around the operation space. When the electron crosses the anode's operation space, stretching occurs between the anode and cathode, simultaneously producing an electric field and magnetic field (produced by the magnet). Therefore, electrically charged particles moved by the magnetic field direction must follow the

rotating electron pole in Figure 3.3. The combination of the components emits microwave radiation and is directed by a waveguide.

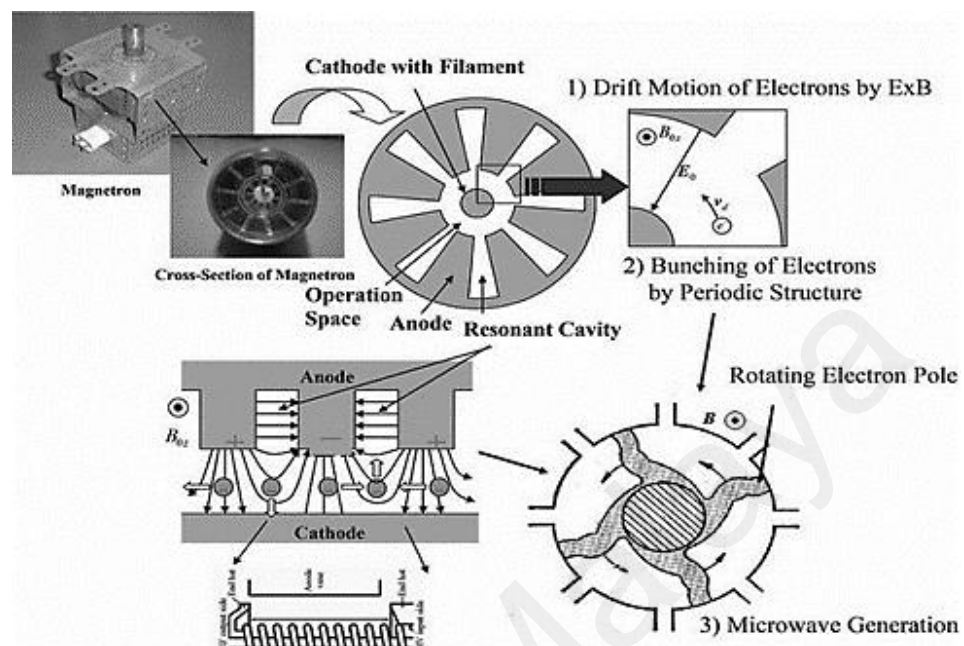


Figure 3.3: Magnetron cross-section and parts

Conventional 6kW, 2.45GHz Microwave Heating Sintering Thawing CW type magnetron operates similarly to the traditional Magnetron and Cathode-ray tube (CW Magnetron Sintering Thawing Datasheet, 2015). A magnetron's cathode is essential in controlling an electron's average velocity or electron drift velocity in operation space.

A thick cylindrical cathode is located at the center, and a cylindrical block of copper is fixed parallel in the center, which acts as an anode. This anode block comprises several slotted blocks that act as resonant anode cavities. The space present between the anode and cathode is called an Interaction space. The electric field is present radially, while the magnetic field is parallel in the cavity magnetron (Boot & Randall, 1946; Jones et al., 2005). A permanent magnet oscillates the magnetic field in the interaction space. The magnetic lines are parallel to the cathode and perpendicular to the electric field between the anode and the cathode, as illustrated in Figure 3.4.

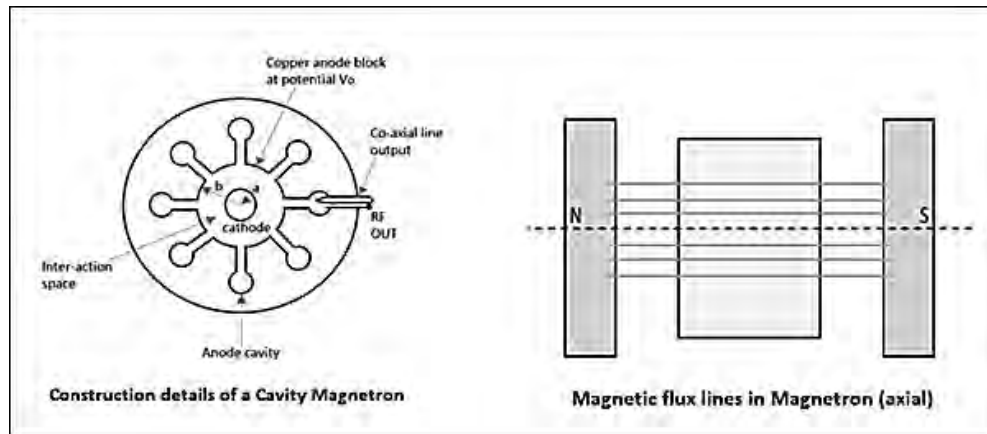


Figure 3.4: Constructional details of a cavity magnetron and the magnetic lines of flux present, axially

This Cavity Magnetron has eight cavities tightly coupled within each other. An N-cavity magnetron has N modes of operation (Boot & Randall, 1946; Boot & Randall, 1976). These operations depend upon the input frequency and the phase of oscillations. The total phase shift around the cavity resonator ring is defined as $2n\pi$, where n is a permanent integer.

If ϕ_v represents the relative phase change of the oscillating AC electric field across adjacent cavities, then $\phi_v = 2\pi nN$. Where $n = 0, \pm 1, \pm 2, \pm(N/2 - 1), \pm N/2$. It means that the $N/2$ mode of resonance can exist if N is an even number.

If $n = N/2$, then $\phi_v = \pi$. This mode of resonance is called π mode. Therefore $n = 0$ then $\phi_v = 0$. It is defined as the Zero mode because there is no oscillating RF electric field between the cathode and is also widely known as the Fringing Field. This mode is not used in magnetrons.

3.3.2 Cavity Magnetron Operations

A few cases are considered when the Cavity Magnetron mode is under operation (Boot & Randall, 1946; Fujisawa, 1958) as an influential operation position for oscillation.

3.3.2.1 Case 1

Suppose the magnetic field is absent in the cavity when $B = 0$, then the behavior of electrons can be observed in Figure 3.5 (Chodorow & Wessel-Berg, 1961). Where electron emits directly goes to the anode under radial electric force.

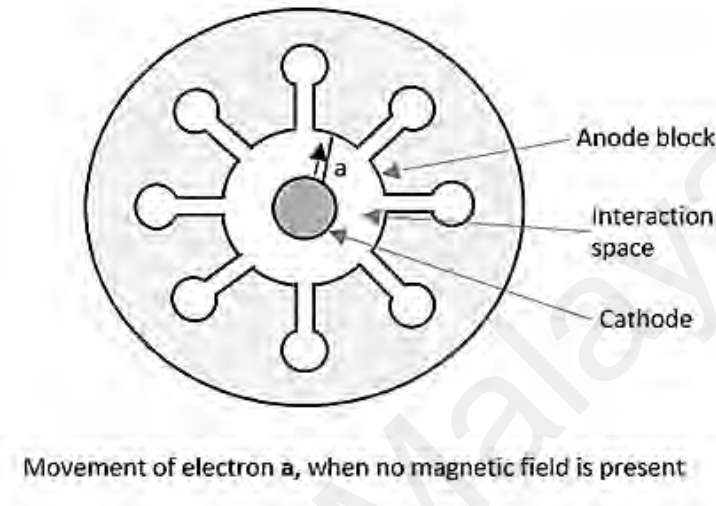


Figure 3.5: The cross-section of the magnetron with the magnetic field is absent

3.3.2.2 Case 2

If there is an increase in the magnetic field, a lateral force acts on the electrons (Boot & Randall, 1946; Sessler & Simon, 1987). It can be observed in Figure 3.6, considering electron b, which takes a curved path while both forces act on it.

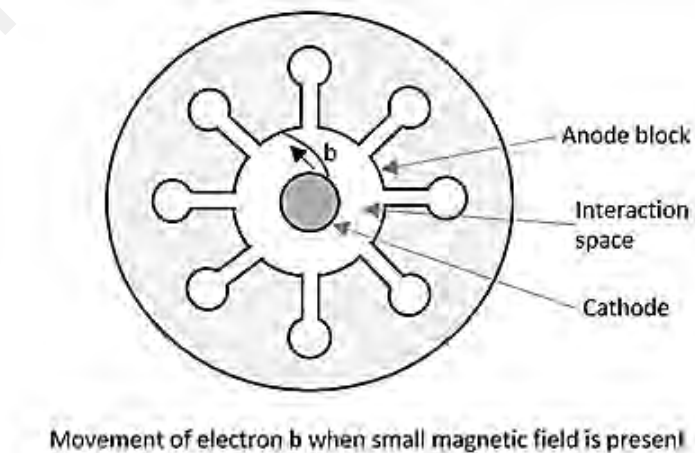


Figure 3.6: The cross-section of the magnetron with the magnetic field is present

The radius of this path is calculated as $R = mveB$. It varies in proportion to the electron's velocity and is not proportional to the magnetic field strength.

3.3.2.3 Case 3

When the magnetic field B is further increased, the electron follows a path such as an electron orbiting the anode surface and producing zero current at the anode (Blazey et al., 1987; Saldin et al., 2002). The "Critical magnetic field" (B_c) is the cut-off magnetic field in Figure 3.7.

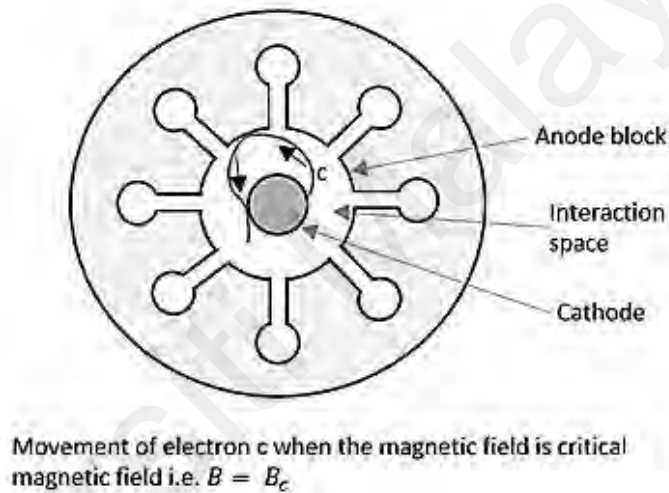
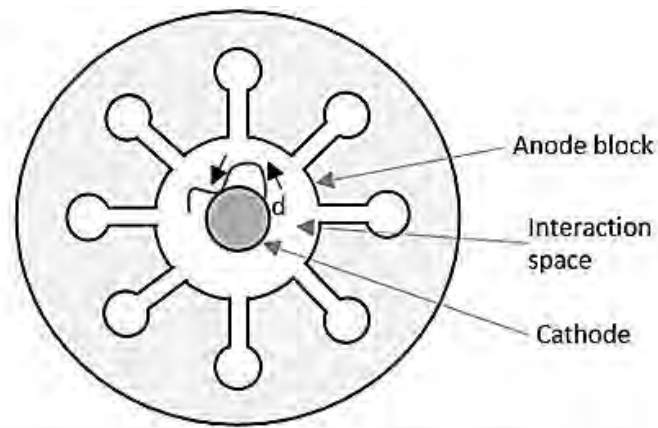


Figure 3.7: The Cross-section of the magnetron with the magnetic field is critical

3.3.2.4 Case 4

However, when the magnetic field is aggressively moving than the critical field, $B > B_c$. Then the electrons follow the path as electron d, where the electron has reflected the cathode without going to the anode (Blazey et al., 1988; Nüchter et al., 2004). It causes "back heating" of the cathode, as in Figure 3.8.



Movement of electron **d** when excessive magnetic field is present

Figure 3.8: The cross-section of the magnetron with the excessive magnetic field is present

It is achieved by switching off the electric supply once the oscillation begins. If this is continued, the emitting efficiency of the cathode gets hugely affected.

3.3.3 Cavity Magnetron with Active RF Field Operations

Cavity magnetron operation is started when the RF field is absent in the cavities of the magnetron static case (Khachatryan et al., 1987). Thus active RF oscillation occurs when the cavity magnetron is activated.

As in TWT, it is assumed that initial RF oscillations occur due to noise transient (Bretting & Klein, 1969; Xu et al., 2011). The operation of the device sustains the oscillations. There are three types of electrons emitted in this process and labeled as electrons “a,” “b,” and “c” in three different cases.

3.3.3.1 Case 1

An electron “a” slow down if oscillations are present, transferring energy to oscillate. Such electrons that transfer the energy to the oscillations are called favored electrons. These electrons are responsible for the bunching effect.

3.3.3.2 Case 2

If another electron, “b,” takes energy from the oscillations and increases its velocity. When this is completed, it bends more sharply, spends little time in the interaction space, and returns to the cathode.

These electrons are called unfavored electrons because it does not participate in the bunching effect. These electrons are harmful as the cause of back heating reflecting magnetron efficiency.

3.3.3.3 Case 3

Suppose electron “c” is emitted later but moves faster. It tries to catch up with electron “a.” The next emitted electron, “d,” tries to step with “a.” As a result, the favored electrons “a,” “c,” and “d” form electron bunches or electron clouds. It is known as the “Phase focusing effect,” as shown in Figure 3.9.

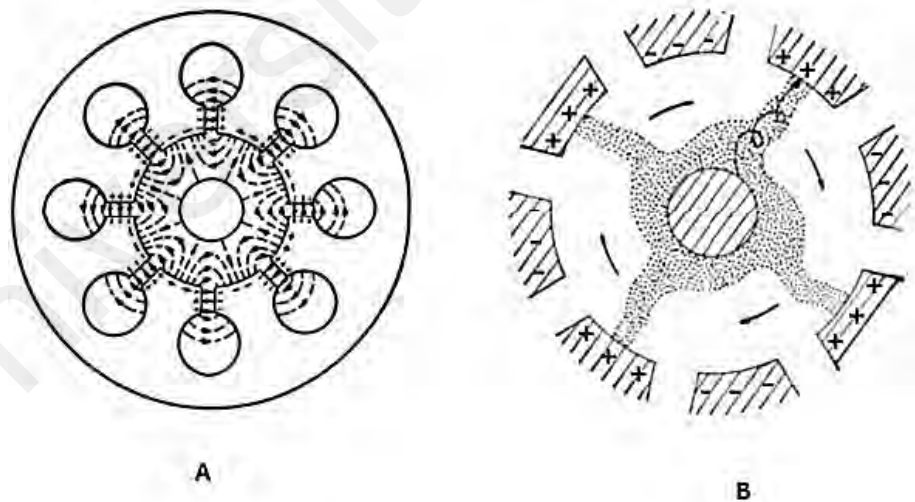


Figure 3.9: (A) Electron movements in different cases, (B) Electron clouds formed

Figure 3.9 (A) shows the electron movements in a different scenario, while Figure 3.9 (B) shows the electron clouds formed. These electron clouds occur while the device is operating. The charges on the internal surface of these anode segments are followed by

the cavities' oscillations (Pottelette et al., 1999). It creates an oscillating electric field rotating clockwise.

Finally, the electric field rotates, and the magnetic flux lines form parallel to the cathode (K. Wang et al., 2020). Under those combined cases, the electron bunches are formed with four spokes, perpendicular in regular intervals, to the nearest positive anode segment, in spiral trajectories (Kearsley, 1984).

3.4 Multiphysics Element Analysis Simulation

The Computer-Aided Design (CAD) tool in COMSOL analyzes and verifies each material's performance to the Magnetron's cathode. A basic magnetron's model consists of components, such as an anode, cathode, operation space, and resonant cavity. The model's measurement is based on the Magnetron manufacturer's datasheet (*CW Magnetron Sintering Thawing Datasheet*, 2015; Surducan et al., 2011; Vyas et al., 2016).

The Magnetron's cathode power dissipation develops a considerable temperature rise, producing thermal expansion in both the anode and cathode, substantiating stresses and strains resulting in a displacement of the resonant structure, transforming the desired Electromagnetic (EM). The oscillation might fail if the cavity temperature surpasses a certain threshold (Boot & Randall, 1946; Kearsley, 1984). Since magnetron efficiency is affected mainly by the operating temperature, a Multiphysics (MP) concept has been adopted. An exact CW-type Magnetron prototype has been developed in a π mode for simulation purposes. The axial static magnetic induction β and electron can oscillate without being captured by the anode by selecting this voltage mode in the anode and cathode. This condition only exists in a critical field, where the voltage in the anode-cathode is equal to the critical voltage (V_c). In contrast, the axial magnetostatics induction must be equal to critical induction (B_c). Both conditions are related to the π mode operating frequency corresponding to the generated microwave power frequency.

The model of the Magnetron simulated consists of a modified cathode, copper anode, and non-ideal vacuum interaction region, as in Figure 3.10. However, for simplification, the cathode surface is modeled as a BaO Substrate and later substituted by GaN and SiC Polymer. The vacuumed medium between the anode and cathode is labeled as operation space, with an air pressure of $P=10^{-10}$ bar. Other materials are temperature-dependent regardless of the high vacuum to establish an accurate reliability model.

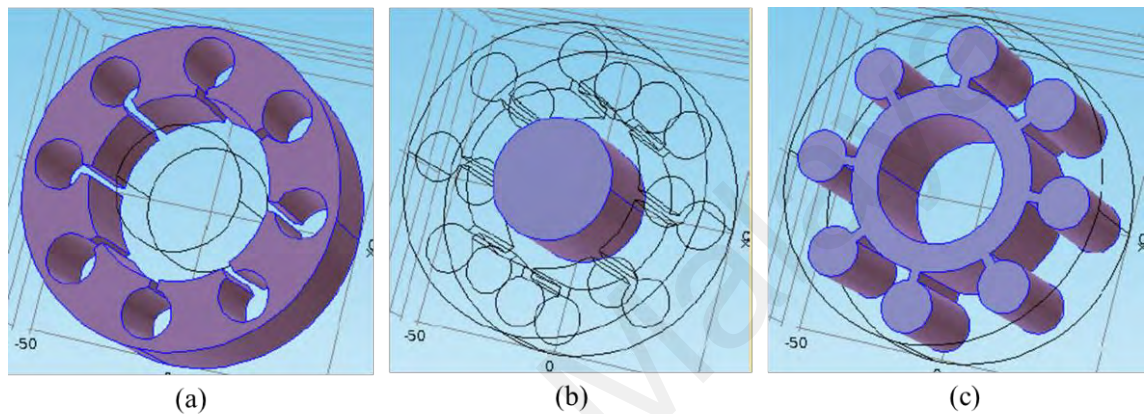


Figure 3.10: Magnetron components, a) copper Anode, b) modified cathode and c) non-ideal vacuum interaction region

The geometry is set with the default setting and uses the physics-controlled mesh with the finite element size in the analysis. Therefore, the completed mesh model consists of 52,889 elements, with a minimum element (mES) required is 4.08^{-4} m, which corresponds to 0.012λ , where λ is the wavelength of operating frequency used at 2.45GHz. Figure 3.11 refers to the build of the 3D Mesh Model.

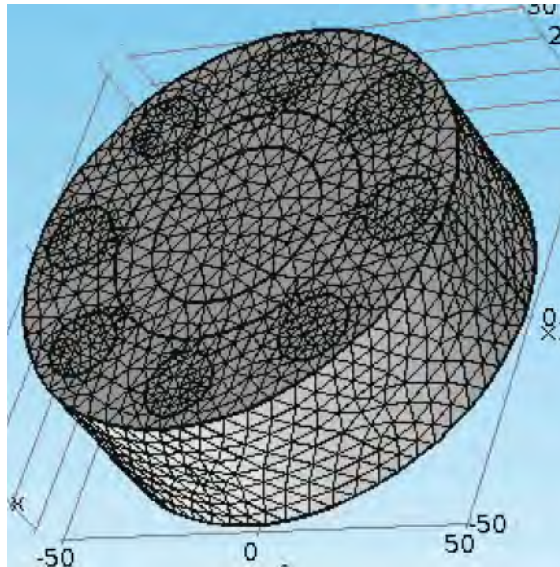


Figure 3.11: 3D Magnetron Mesh Model

Moving Mesh (MM) and storing temperature information are employed in COMSOL due to its ability to combine Thermal Stress Module (TS), Particle Tracing Module (PT), and Electromagnetic Waves Module (EM). TS is used to determine displacement and temperature. MM drives the displacement computed mesh as a function of TS analysis. Note that TS and MM are simulated in a standalone stationary analysis. EM determines the Eigen frequencies corresponding to the Resonant Electric fields by performing Eigenvalue analysis on the magnetron model built and temperature. Electrostatic AC/DC Module (ES) and Charged Particle (CPT) determine the PT and the related properties by executing a time-dependent analysis. Figure 3.12 simplifies the ambient simulation path.

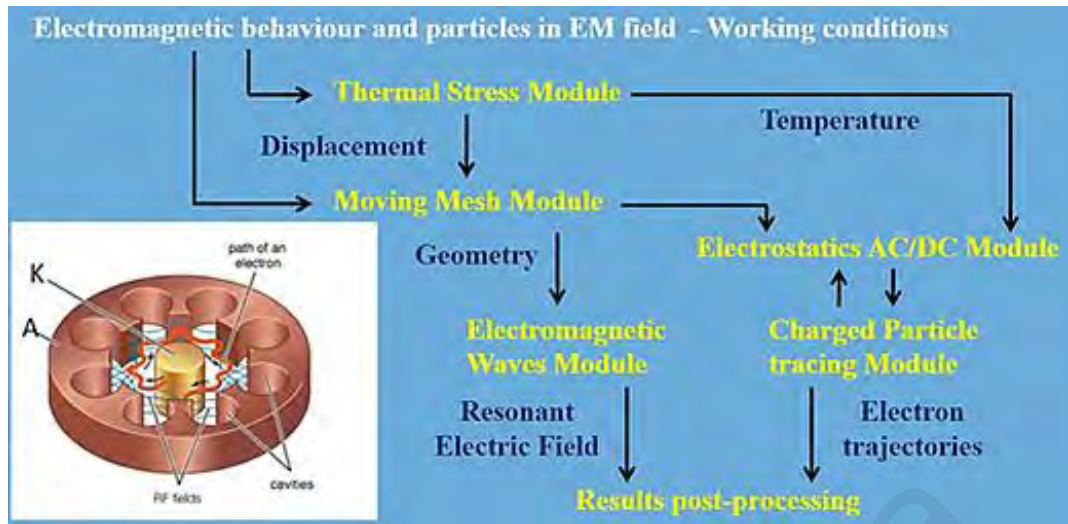


Figure 3.12: COMSOL simulation steps methodology

Therefore, electron trajectories and calculated resonant fields are used to define the magnetron model's functional points to identify the accurate operating of EM and ES conditions. A pathway to obtain post-processing results is shown in Figure 3.12.

3.4.1 Thermal Stress Module

The non-ideal vacuum atmosphere inside the Magnetron volume between the anode and cathode is modeled only to describe the heat transfer from cathode to anode, as in Figure 3.13. The cathode represents a constant volume of heat sources. To reach the necessary temperature for the thermo-electrical effect, $T=1050^{\circ}\text{C}$, the heat power density has been set to $Q = 0.405 \text{ GW/m}^3$.

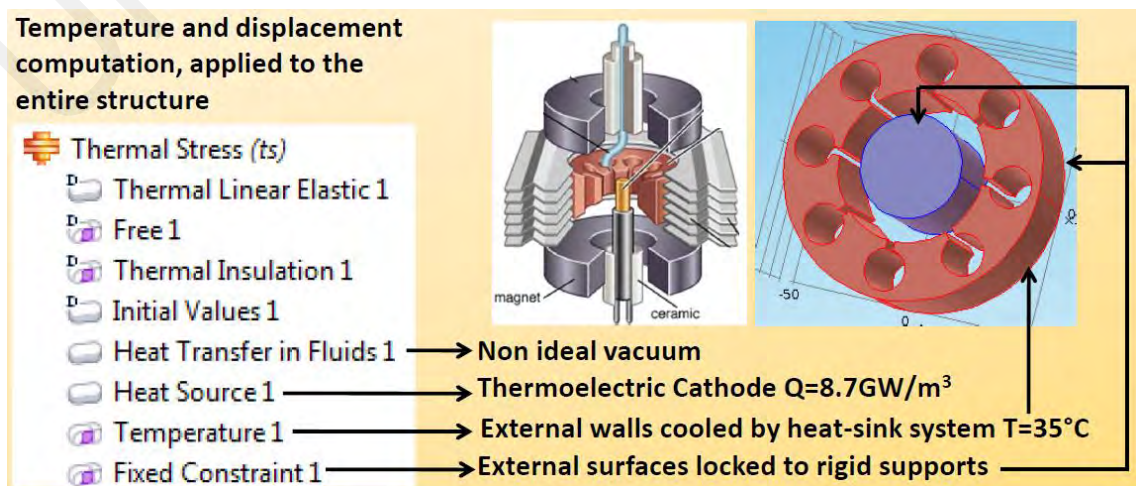


Figure 3.13: Thermal stress steps and procedure

Heat-sink systems cool the external lateral surfaces of the Magnetrons, typically set to 28°C. The external metallic surfaces of the anode and the basis surfaces of the cathode are locked to rigid structures to support the device. Thus, represent the fixed constraints.

3.4.2 Moving Mesh Module

The anode and cathode represent the volumes subjected to the structural formulation by TS analysis, as in Figure 3.14. The non-ideal vacuum volume is free to move since it is subjected only to heat transfer in fluid formulation by the TS analysis (Hu et al., 2018).

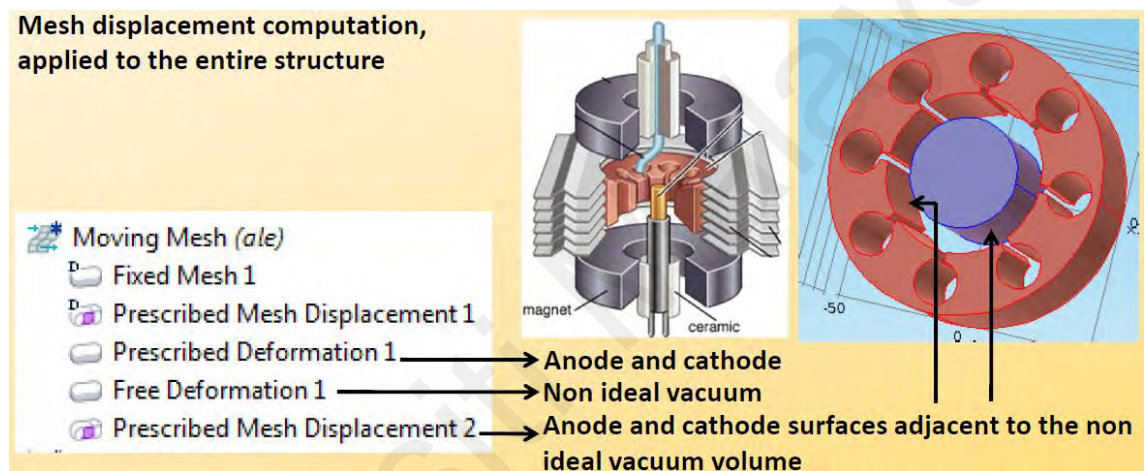


Figure 3.14: Moving mesh steps and procedures

The thermal stress computation deforms anode and cathode surfaces adjacent to the non-ideal vacuum volume.

3.4.3 Electromagnetic Waves Module

The lateral cathode surfaces and the internal lateral anode surface are modeled to consider the losses due to the partial penetration of the electric field in the lossy material, as in Figure 3.15. The specified thickness of the anode and cathode boundaries is fixed at 10 mm (*CW Magnetron Sintering Thawing Datasheet*, 2015). Furthermore, the surface bases of the interaction region are made of a non-ideal vacuum. So, the plane wave which crosses this boundary must be free to feed forward (Ikeda & Itoh, 2018).

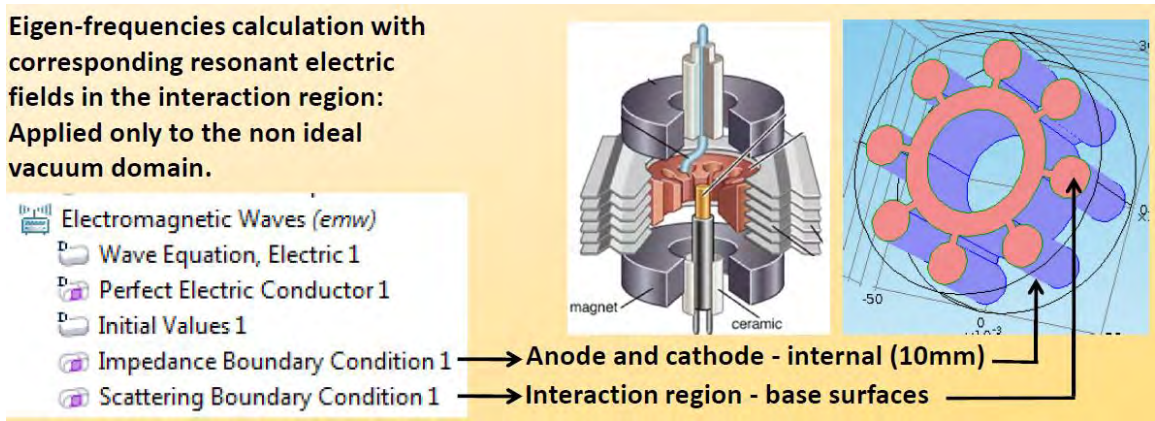


Figure 3.15: Electromagnetic Waves steps and procedures

3.4.4 Electrostatics AC/DC Module

The anode electric potential is set to zero, and the cathode electric potential to $V_k = -60\text{kV}$ is as in Figure 3.16. Dielectric shielding separates the anode electric potential from the cathode electric potential and is applied to the external boundary connecting the anode and cathode (Kim et al., 2011). The surface thickness has been set to 5.2mm (CW Magnetron Sintering Thawing Datasheet, 2015).

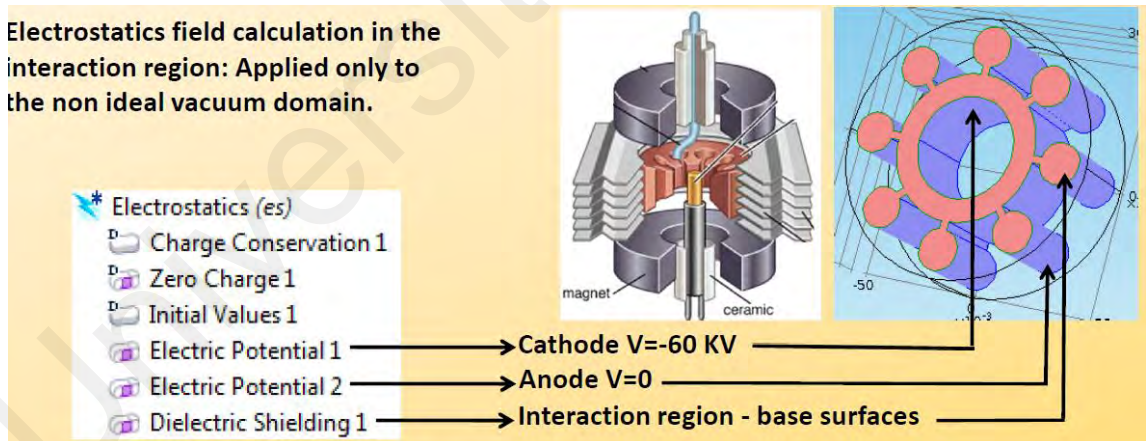


Figure 3.16: Electrostatics steps and procedures

3.4.5 Charged Particle Tracing Module

Electrons are released from the cathode boundary and accelerated by the Force $F = q(-\nabla V)$, where V is the anode-cathode voltage calculated by ES Module as Figure 3.17. Electron trajectory is deflected by the Force $F = qv \wedge B$, where B is the design axial magnetic induction $B = 1,450\text{ G}$. Particle field interaction node adds the two-way coupling

between the particle space charge and the electric field. The particle-Particle Interaction node includes the Coulomb interaction force between charged particles to the total force (Ikeda & Itoh, 2019).

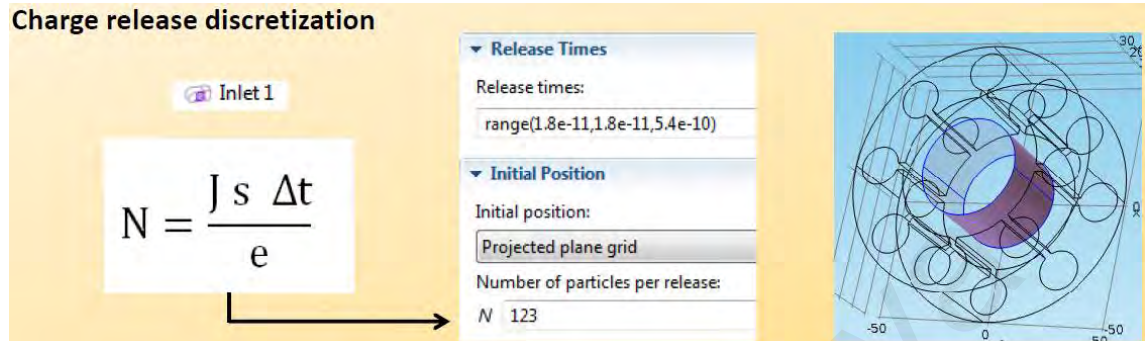


Figure 3.17: Charged Particles Tracing steps and procedures

Since the cathode current density is constant and on the cathode surface, the charge release is represented by a short pulse sequence with an initial null value of a defined number of particles per release, N . Where i is the design cathode current, e is the elementary charge of the electron, and Δt is the time interval between two consecutive charge releases. This design has been set $i = 150\text{A}$, $\Delta t = 2.1 \times 10^{-11}\text{s}$, and $N = 2.48 \times 10^{10}$ particles per release.

This number has been decreased to $N^1 = 123$ to decrease the computational costs. The particle release times have been set to start from $t = \Delta t$ and stop at $t = 42 \Delta t$, by steps of Δt .

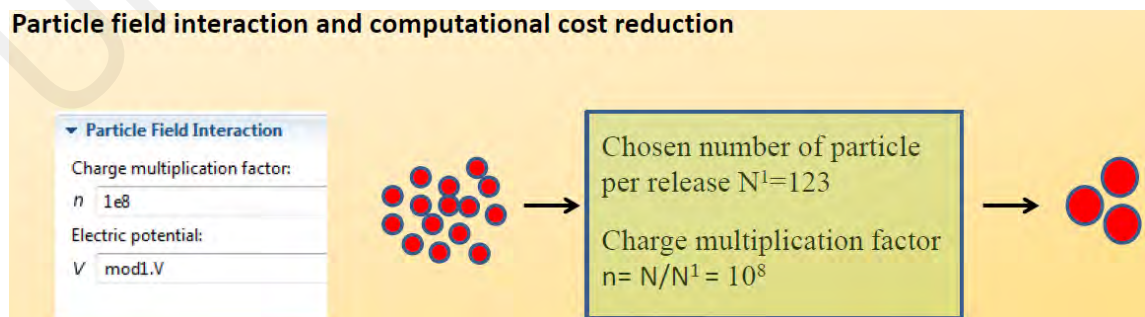


Figure 3.18: PT Interaction and Computational

This feature adds a two-way coupling between the particles and the field to model simultaneously the space charge effect (exerted by the electrons on the ES field) and the force (exerted by the electric field on the charges) as in Figure 3.18.

The number of particle pre-release (in the Inlet feature) has been decreased to $N^1=123$, and a charge multiplication factor (in the particle field interaction feature) $n=108$ has been employed to decrease the computational cost

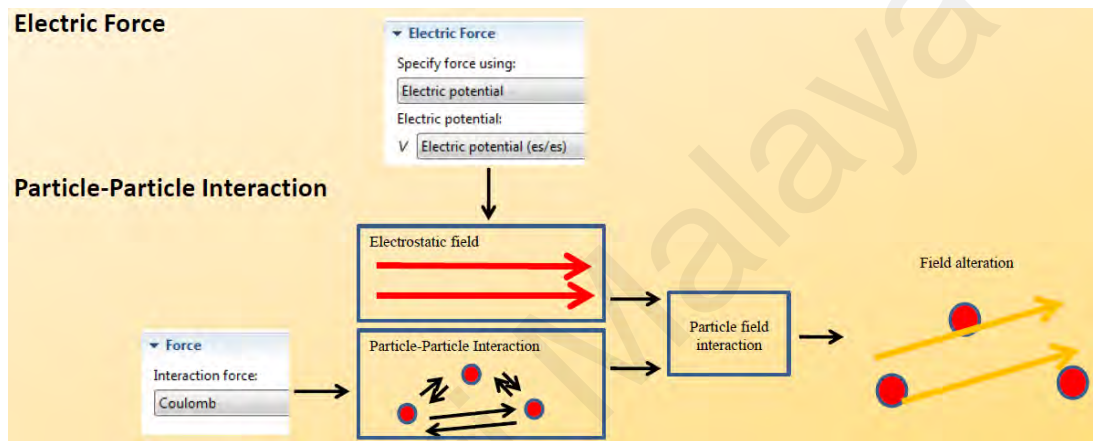


Figure 3.19: Electric Force to PT Interaction

The Particle-Particle Interaction feature includes the Coulomb interaction force between charged particles to the total force. The particle position is step by step updated, and the process repeats until the specified end time for the simulation is reached (Luo et al., 2020). Electric Force is employed to define the electric part of the Lorentz force $F=e(-\nabla V)$ as in Figure 3.19, specified via the electric potential computed time-dependently by the ES module.

3.4.6 Post-Processing Results

The studies are organized in performing two steps: First, a static analysis to compute the thermal TS and MM, then an Eigenfrequency step to compute the Resonant Electric Field and a time-dependent step to compute electrostatic field and particle trajectories,

which has been set to start at time $t=0$ and end at $t=150\cdot\Delta t$, by steps of Δt as in Figure 3.20.



Figure 3.20: Individual steps and procedures superposition

The superposition of the computed resonant field and the electron trajectories have been plotted on a plane that bisects the Magnetron structure. The working points are defined by individuating the correct operating electrostatic and magnetostatics field conditions, as in Figure 3.21.

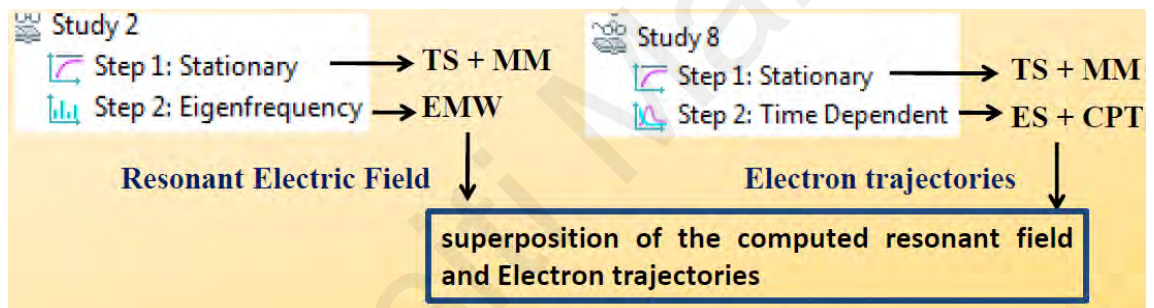


Figure 3.21: Computational of Post-Processing Results

The Magnetron resonance and particle motion have been studied using COMSOL, simultaneously with thermal expansion and mechanical stress. The resonance and velocity alteration due to thermal-structural effects has been documented. The device model has been organized using several strategies allowed in COMSOL to decrease the computational time and resources, maintaining accuracy.

3.5 Annealing Process

The annealing system is modified from the conventional sputtering process to fabricate integrated circuits, ingot, and wafer growth. However, in this experiment, the annealing system is intended to grow an even 100nm thick polymer layer using GaN and SiC combination on the Magnetron's cathode surface of a cylindrical shape. Therefore, a

conventional sputtering system modification, including the deposition chamber enlargement to fit the Magnetron's cathode during deposition, is necessary. Modifying the conventional sputtering system into an annealing system includes an additional transfer arm that regulates the Magnetron's cathode as a target and embeds additional safety features. The modification is necessary as Magnetron's cathode, which serves as a deposition target of 80mm, could not fit into the conventional sputtering system.

The preparation of the magnetron for low-power microwave generation involves direct annealing to the magnetron's cathode surface. Uniformity in semiconductor deposition on the magnetron cathode surface is achieved through a specific annealing process that differs by the deposition temperature and the material's period regarding its characteristics. An improper annealing process potentially leads to leakage of electron flow to the internal layer of the magnetron's cathode. It causes stability issues in microwave power generation due to temperature spikes. This situation potentially leads to risks, such as an explosion due to unstable thermodynamic stability between the magnetron's cathode and the applied semiconductor plasma coating. In this case, it is essential to have a high-quality annealing process on the surface with high-quality semiconductor purity deposition growth.

From the electron drift velocity analysis performed earlier, the annealing process is expected to enable the magnetron to produce a low-power microwave with improved efficiency than the conventional magnetron by controlling the electron drift motion known as electron movement speed. A lower electron motion speed generates lower heat density; this is the key to achieving a highly efficient magnetron. Therefore, the magnetron's cathode surface is deposited with two different semiconductors in dedicated experiments in this process. Before the annealing process begins, the magnetron's cathode is dismantled from the magnetron fixture and is grown with high-purity GaN and SiC

Polymer semiconductors. Figure 3.22 shows the magnetron's vertical cross-section view with the cathode located in the mid-section of the magnetron. The magnetron's cathode-to-sputter dimension is 80mm and 25mm in diameter (*CW Magnetron Sintering Thawing Datasheet, 2015*).

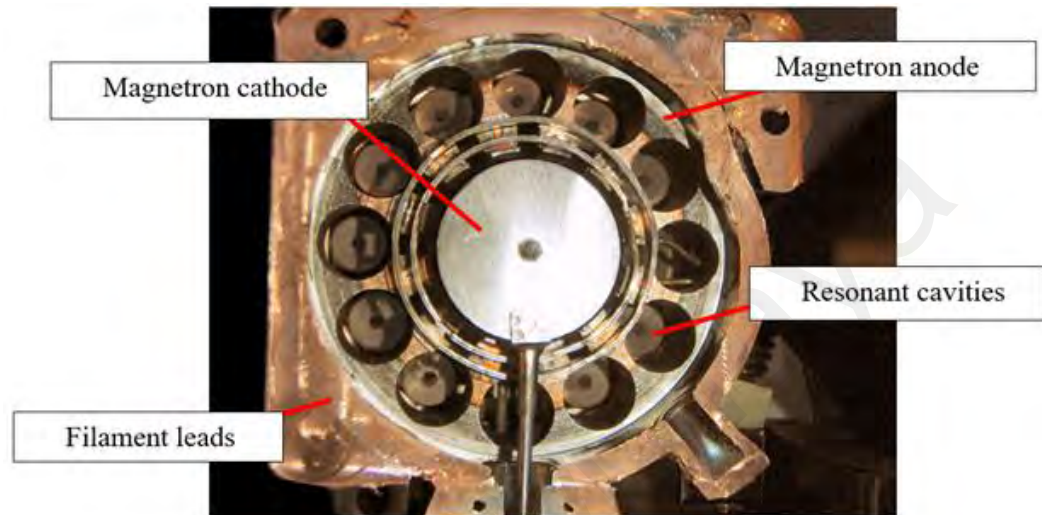


Figure 3.22: Conventional magnetron cut-off

The semiconductor selection with a higher melting point ensures the magnetron is safe to generate microwave power and is stable (Chapin, 1979; Somekh, 1984). A strong coupling between the anode, cathode, and resonant cavity occurs during microwave power generation. This strong coupling produces heat that commonly exceeds the temperature of 300 °C. Therefore, materials used in a magnetron must hold a high temperature and have a high melting point to ensure their safety.

Annealing of semiconductor plasma to the magnetron's cathode is done through a complex deposition system setup. Magnetron's cathode is placed on the right through a deposition system in horizontal, which is labeled as the target component. The transfer arm is used to push the magnetron's cathode into the deposition system chamber for an even plasma annealing ratio. At the same time, polymer semiconductors, GaN, and SiC, are placed on a tray labeled as substrates.

The selected substrates are carefully and rigorously prepared to eliminate surface contamination. First, the substrate is washed in ultrasonic trichloroethylene (TCE), an industrial solvent used to remove organic compounds. The ultrasonic bath serves to agitate or accelerate the bombardment of the liquid particles with that of the substrate surface, increasing the effectiveness of the cleaning. It would also serve to remove any surface particulates. The TCE must be handled with extreme care as it is a dangerous carcinogen. After the TCE is used, the sample is rinsed in de-ionized (DI) water. It then undergoes another ultrasonic bath in a different solvent, concentrated acetone. It is used to remove other potential organic compounds on the film surface. Another rinse is performed if necessary. Any residue from the acetone bath is removed using an ultrasonic bath of isopropyl alcohol (IPA). Finally, the substrate is cleaned in a bath of methanol. Methanol evaporates very quickly and also serves to remove any adsorbed water from the surface of the substrate. Care must be taken not to allow water to enter the squeeze bottles of the methanol; it dilutes the methanol and reduces its effectiveness in removing water.

After the substrate has been cleaned, it is affixed or bonded to a roughened Inconel sample holder with low vapor pressure silver thermal paste. Initially, the sample holder was smooth but was roughened with fine-grit sandpaper to increase the surface area the thermal paste could attach, thus binding the substrate to the sample holder more securely. The thermal paste must be cured for several hours, during which the temperature of the sample holder is increased to a few hundred Celsius using a resistive heated hot plate. Curing the paste guarantees a more secure bond and ensures excellent thermal conductivity between the sample holder and the substrate. The curing process may also alleviate some stress present in the substrate by mildly annealing it.

All told, substrate and sample preparation took almost an entire workday. For this reason, a second Inconel holder was purchased to allow one holder to be prepared while

another is used for film fabrication. Note that powder-free disposable nitrile gloves are worn during all preparations, and the sample is only held using plastic tweezers or with a particle-free KimWipe. Additionally, the substrate surface can be blown clean with high-purity argon gas to remove particulates. Before introducing the sample into the load lock, a final wipedown with methanol and a KimWipe is performed.

The targets are 3-inch diameter disks of the chosen material. Sputter targets are long-lived sources ideal for two-chamber PVD systems where the main chamber should be open to the ambient as infrequently as possible for maintenance. The targets used for the system are a minimum of three nines purity or 99.9% purity. Note that the way the targets are manufactured can determine their purity, density, and porosity, all of which are interrelated. For example, sintered targets are less dense and may outgas more porous once the outer layers have sputtered off. The magnetron guns are actively cooled to prevent overheating and melting of the targets. The targets are typically screwed or bonded to a copper backing to increase heat removal. The uranium and cerium targets are brittle, causing the threads to break off, thus detaching the targets from the copper plates unless bonded with a thermal compound. Alternatively, the targets can be placed under the guns without a backing plate if the guns are operated at a low enough power. However, the choice of power supply can also affect this decision. For example, RF power supplies can cause non-conducting materials to heat rapidly.

The heating of the targets can cause them to expand slightly, but the most remarkable change in the target shape is from sputtering. In planar magnetron sputtering, the target develops a racetrack depression on the surface. This changing geometry can affect the deposition rate, vapor flux distribution, and other deposition parameters, such as the amount of reactive gas needed for responsive deposition in reactive sputter deposition. Typically, only a fraction of the sputter target, usually 10 to 30 percent, is used as the

racetrack erosion determines the overall lifetime of the target. The time can be increased by removing the target and melting it so that the surface becomes symmetrical. However, this can introduce impurities into the target, and it is usually simpler and more cost-effective to buy a new target.

Another consequence of sputtering is that the target may become coated in thin smut of fine particles. These particles may result from the poisoning of the target, gas-phase nucleation, or cross-talk with other sputter guns where the material is deposited on another nearby target. These particles can be wiped off during maintenance or cleaned using pre-sputtering. Pre-sputtering simply spins the target for a given time while the substrate is shielded by a shutter or held in the load-lock chamber. Sputtering removes adsorbed contaminants from the surface of the target and is most commonly used to remove any excess compound created by the reactive gas. It is important to note that the surface morphology of a sputter target can affect the morphology of a sputter-deposited film. A smooth, clean, sputtered target produces a more uniform flux of sputtered atoms. Therefore, the target should always be pre-sputtered before film fabrication and for an increased time after system maintenance that involves opening the main chamber.

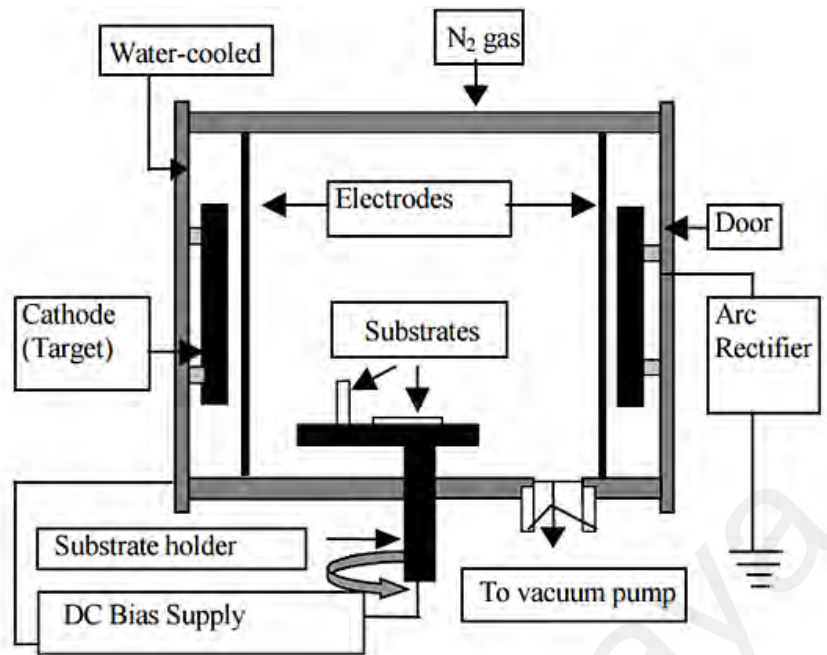
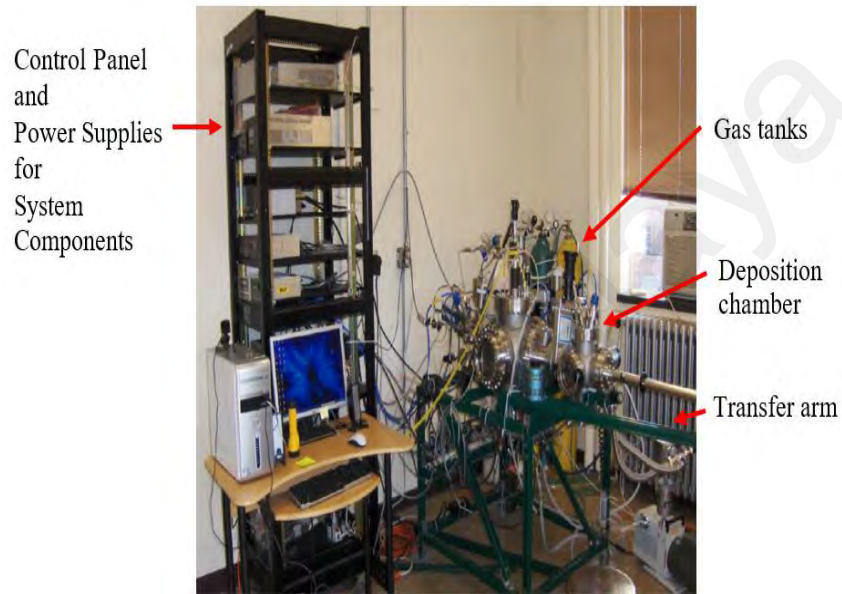


Figure 3.23: Gas flow in an annealing chamber

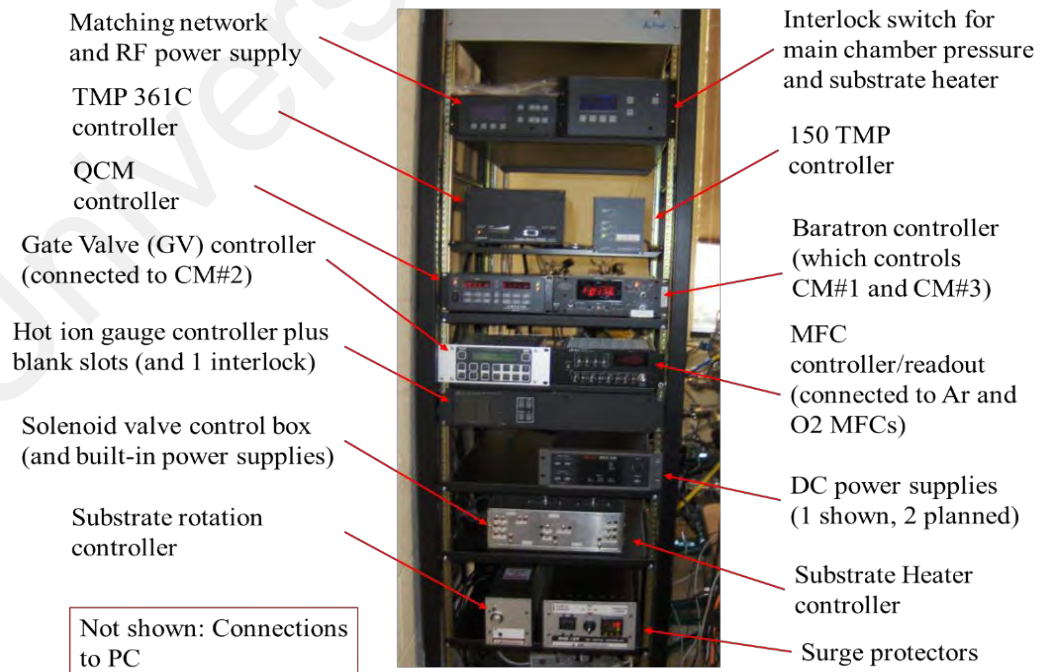
The input of high-pressure gas such as N₂ increases the pressure of the deposition system chamber. Therefore, the vacuum pump below the system reduces and balances the pressure through a valve controller. During annealing to grow GaN and SiC, Nitrogen Gas is used, while annealing to grow the polymer, Carbon Gas is used, respectively, as in Figure 3.23. Due to the different characteristics of each semiconductor, annealing of GaN and SiC Polymer is done in a different annealing parameter such as temperature and annealing period. Each process of polymer annealing is supplied 3kV to the magnetron's cathode during the annealing process to enhance the growth of substrates on the surface. After the first annealing process using GaN, a layer of graphite can be physically seen, and a layer of sapphire can be seen after the second annealing of SiC.

Magnetron's cathode is made from a combination of high purity Copper and Oxide material, specifically, BaO, which has superior conductance and generates high-power microwaves. Both semiconductors sputtered in different conditions of temperature and decomposition period in line with the respective characteristic, such as melting point temperature, material growth, and evaporation rate. Figure 3.24 shows the experimental

setup for the magnetron cathode annealing, modified from a standard annealing setup in semiconductor fabrication for integrated circuit development. Generally, there are three main types of annealing: confocal annealing, in-situ tilt sources in a confocal annealing system, and direct annealing. The annealing process used in this experiment uses confocal annealing as it involves more than one material simultaneously.



(a)



(b)

Figure 3.24: Annealing process equipment setup. (a) front view, (b) side view

Therefore, as the magnetron's cathode diameter is annealed at 80mm, a confocal annealing method is chosen due to its suitability to the chamber design. Direct annealing can achieve +/-5% decomposition uniformity on the magnetron's cathode surface.

The magnetron's cathode cylinder is fixed horizontally into the deposition chamber cage and attached to the transfer arm. A voltage of 3kV is supplied to the cathode throughout the process to produce a strong magnetic field around the cathode cylinder for semiconductor seed deposition. A manual control panel is used to control the rate and pressure of flammable gas pumped into the deposition chamber while controlling the semiconductor plate and transfer arm movement when the chamber is ready to be ramped toward the desired deposition temperature, as in Figure 3.25. An integrated power supply is used to power up all valves and motors in this operation. In addition, a high-temperature monitoring camera is attached to the deposition chamber's top position and connected to a computer for the deposition observation.

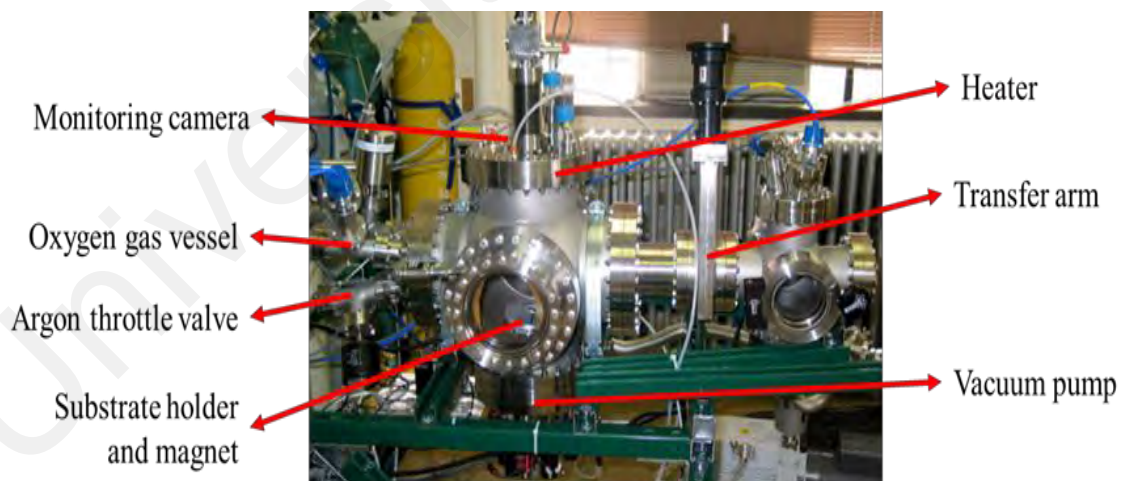


Figure 3.25: Deposition chamber

With the chamber pre-heating up to 950°C and achieving the desired deposition temperature, the transfer arm is used to shift the magnetron's cathode into the midsection of the chamber. The cathode is the deposition target required to be pre-heated simultaneously. A 3kV voltage is supplied to the cathode to ionize the seed from the

substrate holder at the bottom. Due to ionization, the seeds are pulled, and the semiconductors grow constantly. Hence the deposition period is initiated. The cathode keeps rotating at a constant rate and is pushed into the chamber using a transfer arm to deposit the semiconductor onto the other parts of the cathode surface.

3.4.2.4 Gas Supplies, Mass Flow Controllers, and the Gas Injection Manifold

The reactive gas and the working gas supplies used are five nines and six nines pure, respectively (99.999% O₂ and 99.9999% Ar). Each gas supply used dual-vane, high-purity stainless-steel regulator valves specific to that gas/bottle connection. In contrast to single-vane regulators, dual-vane regulators allow the gas supplied to remain at a continuous, non-fluctuating pressure as long as gas is available in the tank. The regulators have stainless steel VCR connections connected to lock-in integral VCR valves that the manufacturer cleaned to cleanroom standards. The secondary valves then connect to custom-ordered ¼ in. stainless steel piping with VCR connections bent into the desired shape using a pipe bender. These metal gas lines transport the gases to their respective Mass Flow Controllers (MFCs). The tanks and associated valves and piping. The processing gases are the two smaller tanks to the left. Note that for safety purposes, the O₂ line also has a flash suppressor so that if flammable gas were somehow introduced into the line and ignited, it could not cause backflow into the O₂ tank.

Additionally, the regulators only allow up to 30 to 40 psi pressures. It is intentional so that the gas lines cannot become over-pressurized. Over-pressurization would damage the MFCs; safety could be further enhanced by adding a pressure relief valve and flow restrictor in line with the MFC. Figure 3.26 from left to right shows O₂, Ar, “low” purity Ar, and Air and associated hardware ((M), 2015). Figure 3.27 shows the gas valve solenoid from the top O₂ and bottom Ar of MFCs.



Figure 3.26: Gas tanks

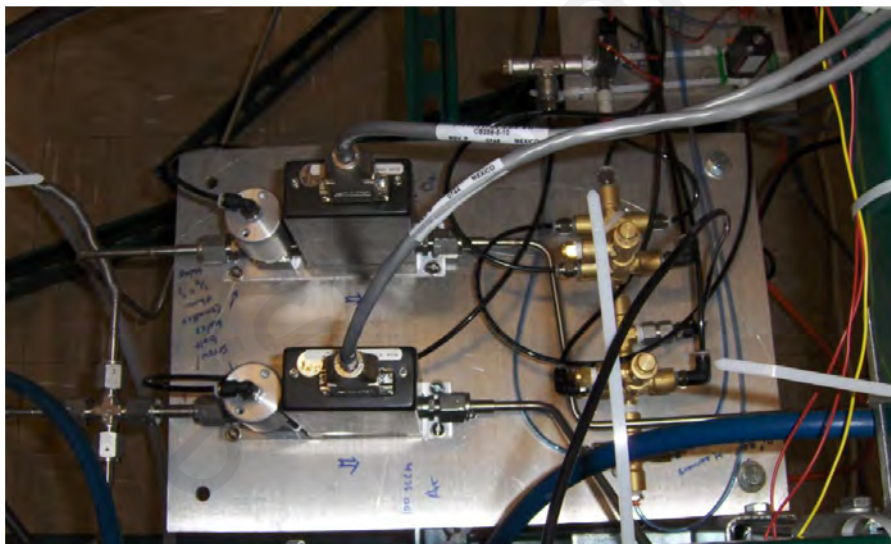


Figure 3.27: Gas valve solenoid

The MFCs are used to control gas flow into the main chamber. Each MFC must be calibrated to a particular gas and has a maximum allowable flow rate; in this case, the MFCs are a 10 sccm O₂ MFC (top) and a 100 sccm Ar MFC (bottom).

MFCs are a combination of a mass flow meter and a metering valve. The mass flow meter takes a percentage of the gas flowing through the MFC and channels it across a heated element. The power needed to maintain the element at a constant temperature is measured and used to determine the gas flow based on the thermal conductivity of the gas

((M), 2015). It is explained that the MFC must be calibrated for a particular gas. The cooling rate also depends on the amount of turbulence in the gas flow, so MFCs are designed for specific mass flow ranges ((M), 2015). The output measured by the meter in the MFC is then used to control a mechanical actuator which functions as a metering valve. This metering valve is not intended to function as a shut-off valve. Each MFC used in the system has its pneumatic shut-off valve.

The pneumatic valves used to control the magnetron shutters and gas injection lines were made toggleable. It was done mainly to simplify operating procedures and reduce gas injection variability by having the valves opened relatively immediately compared to manual operation. The pneumatic valves operate based on the introduction of compressed air forcing the valve open or closed. Some of the valves are held open by a constant set pressure. The valve closes when the compressed air is vented from the line, thus removing the air pressure. Other pneumatic valves, namely those operating the shutters, required a burst of gas to open the valve and another burst through a different port to close the valve.

The air supplied to the pneumatic valves is dry compressed air. The regulator is set to approximately 80 psi, opening the in-line valve. The dry air passes through 5/32 (O.D.) tubing connected to the valve via plastic quick connect or push-to-connect to steel NPT adapters. Quick connects help allow lines to be detached and reconnected in seconds without requiring tools.

NPT brass crosses, tees, and elbows as they were readily available. The manifold can be seen in Figure 3.28 (back center-right) and is controlled by the solenoid, as in Figure 3.29. Brass was an acceptable material as the air feed had no purity requirement other than not containing particulates or excessive moisture. Additionally, since dry air was the working gas, the connection of brass and steel components would not serve to promote electrochemical corrosion.

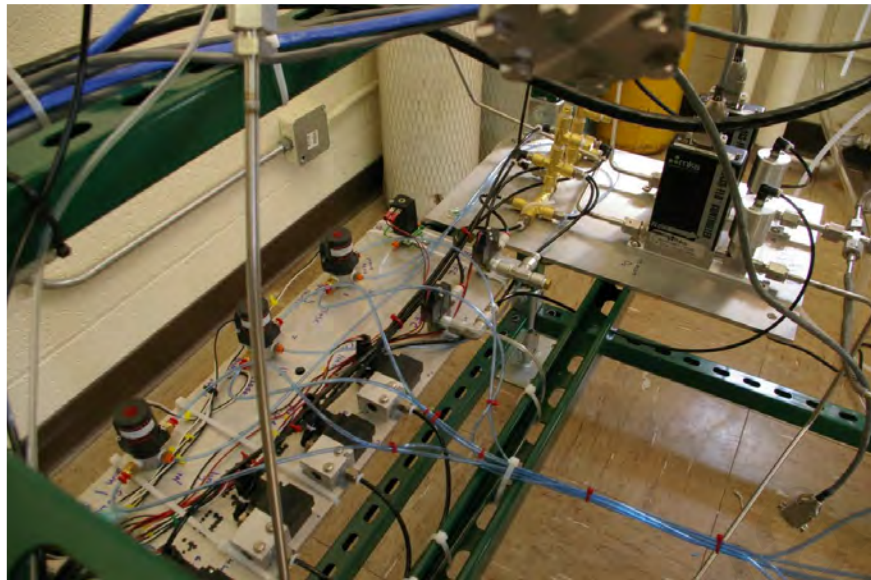


Figure 3.28: Gas distribution lines

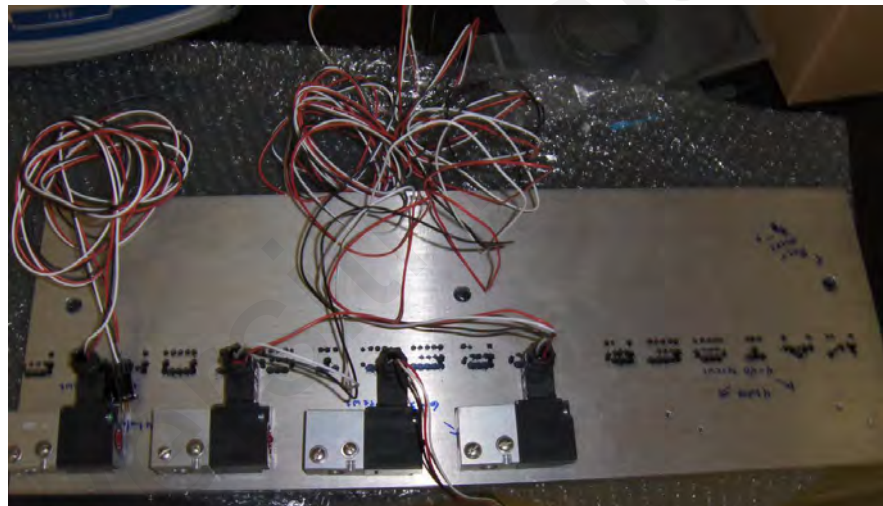


Figure 3.29: Solenoid valves for Ar and O₂ lines

3.6 Experimental Setup

A basic microwave power transmission experimental setup is developed to verify the material change in the magnetron's cathode simulated earlier. The setup consists of a power supply, NI PXI controller, PXIe-5654 RF Analog Signal Generator Module, magnetron, rectenna, rectifier, and battery, as shown in Figure 3.30. A power supply is used to feed 5V DC to the magnetron. An alternative battery could be considered for future applications; however, in this experiment, a portable DC unit ensures a consistent supply instead of a battery. National Instrument PXI through PXIe-5654 RF Analog

Signal Generator generates 2.45GHz carrier frequency to the magnetron and monitors the system performance. Due to transmission distance, an LV15 voltage sensor attached to the rectifier is connected and monitored by NI PXI through ZigBee. 25dBi Yagi-antenna is used to beam power 10 m. from the transmitter to the 20dBd Dipole antenna at the receiver. A full-wave bridge rectifier obtains DC voltage to charge a 3,500mAh Lithium Polymer (LiPo) battery. 3,500mAh battery capacity is chosen as it is popularly used in the market.

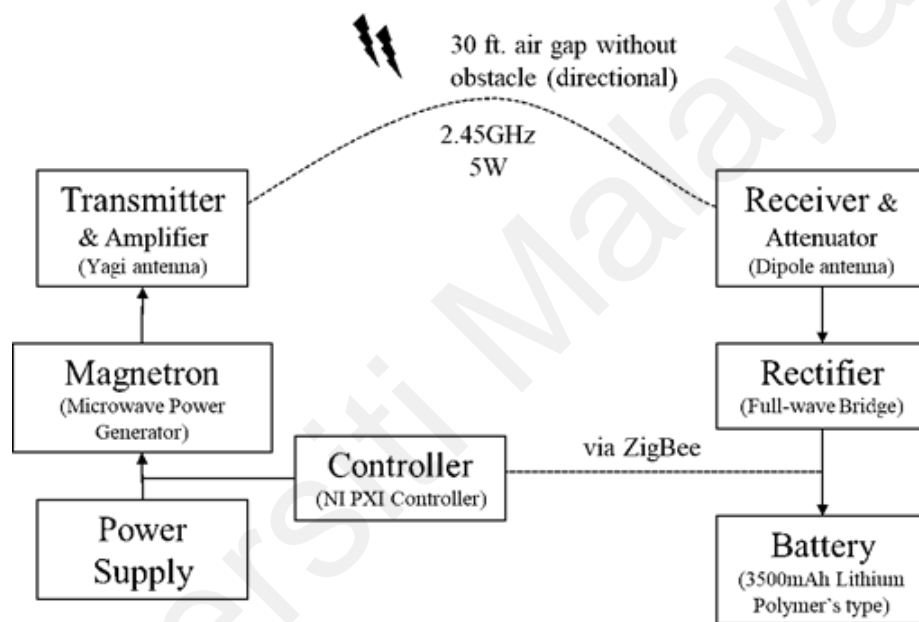


Figure 3.30: Experimental setup block diagram

This experiment is performed in a 10 m compliant semi-anechoic EMC Test Chamber (10n-SAC-LP) for emissions testing to CISPR 16-1-4 and compliant immunity testing to EN6100-4-3 as shown in Figure 3.33 to comply with the safety and health regulation (Code, 2015; Gandhi, 2019; Shakeri et al., 2018). Transmission components such as rectenna and magnetron are placed inside the chamber. The monitoring and control equipment is located outside the chamber. The monitoring and data collection network are connected through the ZigBee Bluetooth module to NI PXI. The receiver is connected directly to a 3,500mAh communication device battery. A few parameters were recorded

throughout this experiment: namely, the receiving voltage in the receiver, the thermo-switch snap period, and the charging time.

Subsequently, the magnetron cathode is sputtered with GaN and SiC polymer, and it is then re-assembled into the magnetron core fitting to measure its performance. The magnetron generates 5W microwave power using 2.45GHz for each test. The power supply of 5V is used for the magnetron. However, in this case, the magnetron is placed inside a closed anechoic chamber for health and safety purposes during the experiment. Therefore, a transformer and capacitor are used to replace the power supply. The magnetron output terminal is connected directly to the waveguides, coaxial matched load, and copper cavity flange to the measurement system components for further analysis.

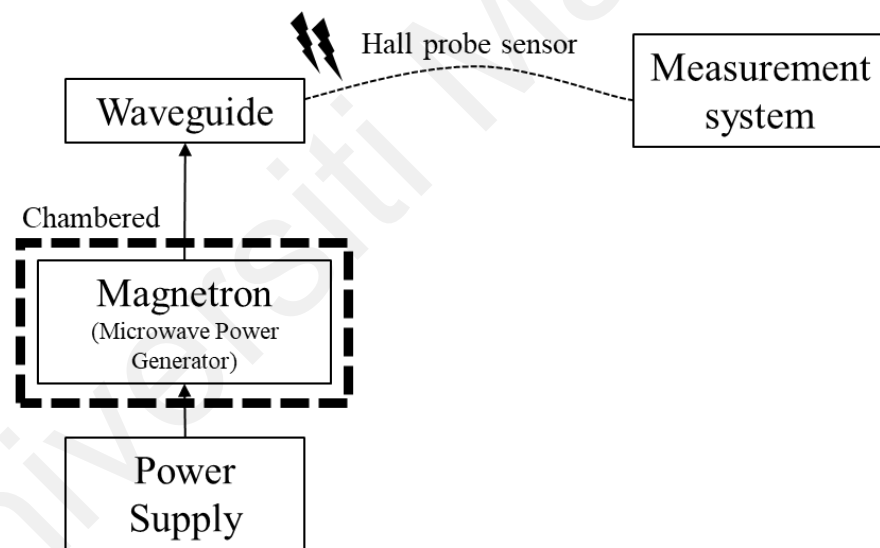


Figure 3.31: Experimental measurement setup diagram.

WR340 waveguide coupling is used for magnetron frequency pulling measurement supported by the hall probe sensor. The microwave power signal generated follows the drive current for measurement. Figure 3.31 shows the measurement setup after the magnetron is placed in a closed anechoic box and connected through waveguides. The measurement system component includes the network analyzer for measuring the scattering parameter with isolation at load, spectrum analyzer, power supply, and

oscilloscope. The measuring system is divided into two parts; the power transmitter is on the left side, while the rectenna is on the right.

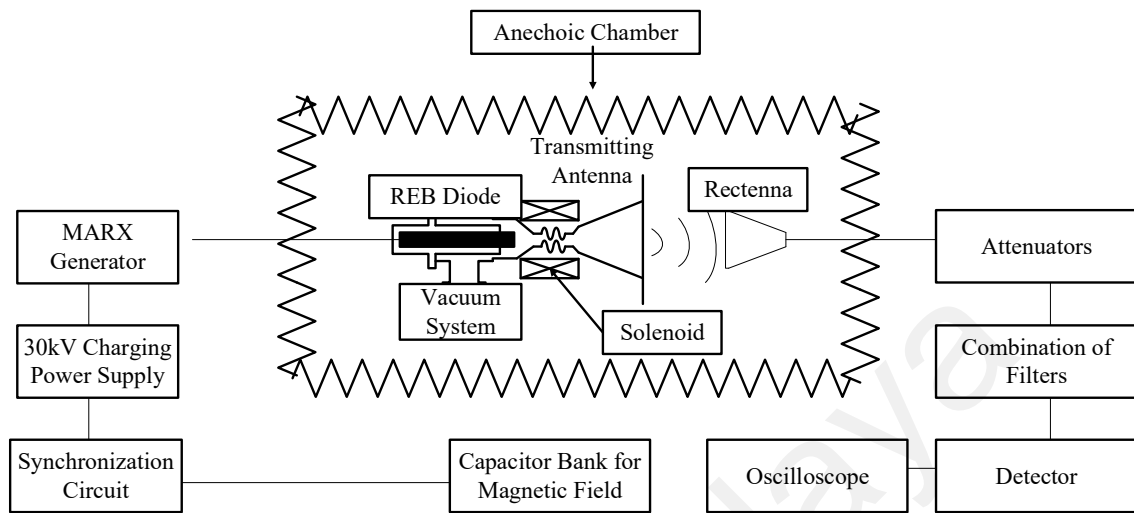


Figure 3.32: Diagram of measuring system

Figure 3.32 shows the magnetron's current captured through a SiC and GaN Polymer magnetron cathode spectrum analyzer. However, the output current from the conventional magnetron is beyond the measurable limits due to unstable operation. The comparison between BaO Substrate and, GaN and SiC Polymer magnetron is observed. There is a noticeable current distortion for the GaN and SiC Polymer, and an expected higher total harmonic distortion (THD) is recorded. GaN and SiC Polymer produce less distortion and smooth output current, easily filtered to obtain an ideal waveform.

The experimental results are categorized into three conditions to charge the 3,500mAh Lithium Polymer (LiPo) battery: conventional wire charging at a rate of 5V, 1A, and the use of BaO and GaN and SiC polymer coated magnetron's cathode. BaO substrate and, GaN and SiC Polymer coat are tested for a microwave power transmission system with an experimental setup consisting of an amplifier and Yagi antenna as a direct transmitter beam over 10 m. static without any obstacle. The power is then received by a dipole antenna and connected to an attenuator. A full-wave bridge rectifier is used to obtain the

power, and the voltage received is measured at this point. The performance is monitored using a NI PXI Controller via ZigBee attached to the rectifier circuit as the experiment setup in Figure 3.33. The transmission is operated at 2.45GHz.

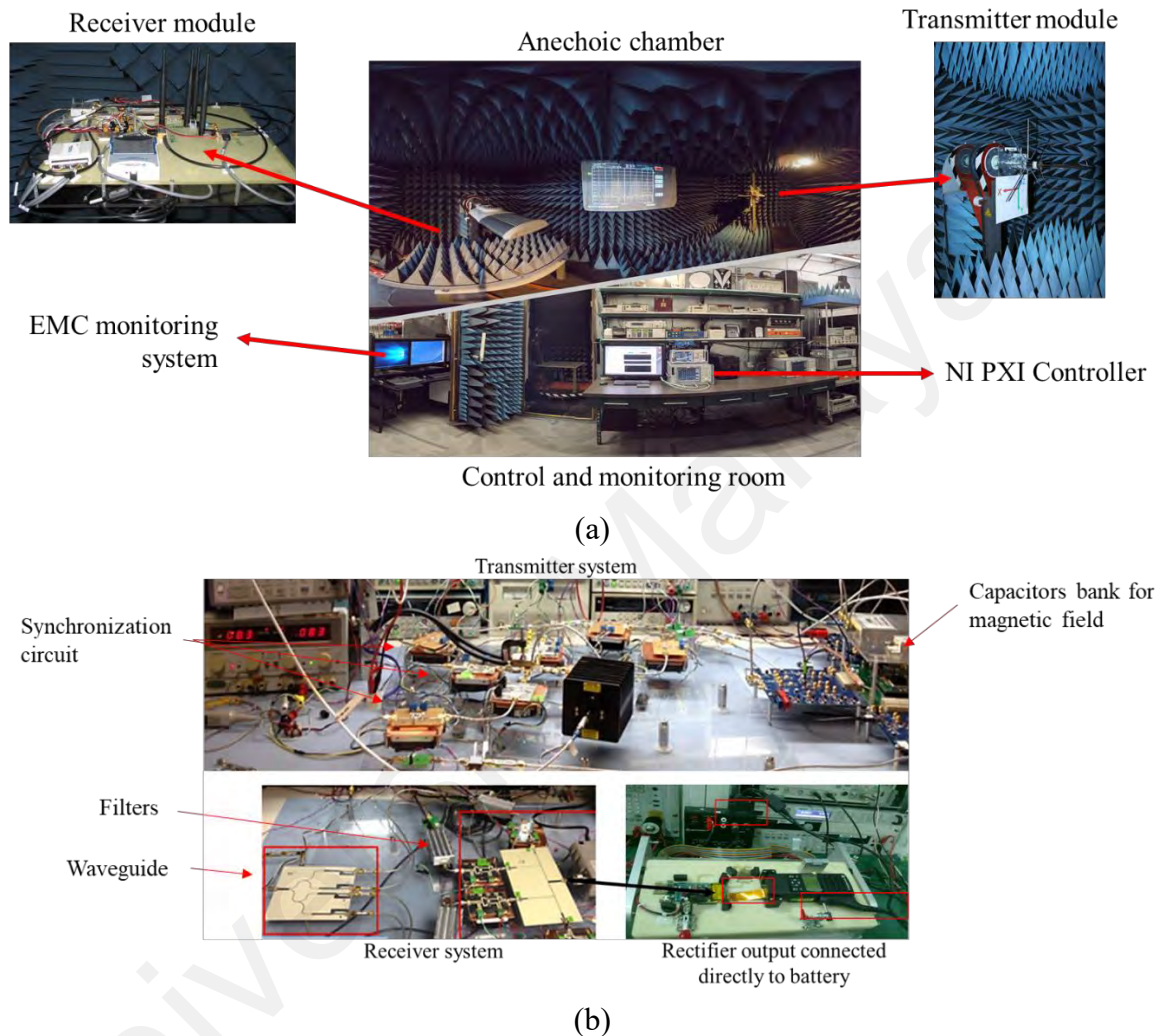


Figure 3.33: Experimental setup; a) Rectenna, b) Connection to battery

3.7 Summary

An analysis has been performed to support the simulation resulting in different electron drift velocity speeds in each material. GaN and SiC polymer electrons propagate slower than BaO material. Simulation in COMSOL is developed based on CW Sintering Thawing Magnetron's parameters. Simulation shows that GaN and SiC polymer magnetron cathode has better heat stability and lower heat density while operating at the desired parameters than the BaO material magnetron. Other parameters are obtained from

the analysis. It can be concluded that GaN and SiC Polymer performed better than BaO Substrate's magnetron cathode at high frequency and low power operation. Further works to prepare the magnetron cathode based on the simulation are performed through an annealing process. Finally, experimental validation is conducted to verify the proposed method solutions.

Universiti Malaya

CHAPTER 4: RESULTS AND DISCUSSION

4.1 Introduction

The simulation results are successfully adopted, supported by the electron drift velocity analysis. Simulation results show significant performance for GaN and SiC Polymer magnetron cathode compared to BaO Substrate magnetron cathode. It is verified by the experimental validation performed for the annealed magnetron cathode. Morphology images are also illustrated in this chapter to determine the quality of the annealing process.

4.2 Simulation Results

The temperature deformation scale ranges from room temperature starting from 20°C to 200°C. An industrial magnetron may produce a deformation scale up to a maximum of 800°C. According to magnetron's datasheet, the nominal operating temperature ranges between -25°C to 1100°C (*CW Magnetron Sintering Thawing Datasheet*, 2015; Surducan et al., 2011; Vyas et al., 2016). However, efficiency may vary based on the temperature of the magnetron. Thus, this simulation is essential in developing an experimental safety and health precautions setup. Examining the heat density in the cathode heating for TS static analysis shows a peak temperature of 380°C.

The anode is tested at 730°C for BaO coated cathode's magnetron. The analysis shows that maximum stress occurs on the bottom of both cathode bases since there is only one constraint, and heat is generated from the cathode and focused on the strong magnetic coupling. The maximum stress applied for this simulation is $Q = 0.56 \text{ GW/m}^3$, and the limit before the magnetron becomes unstable is about 7.0 GW/m^3 .

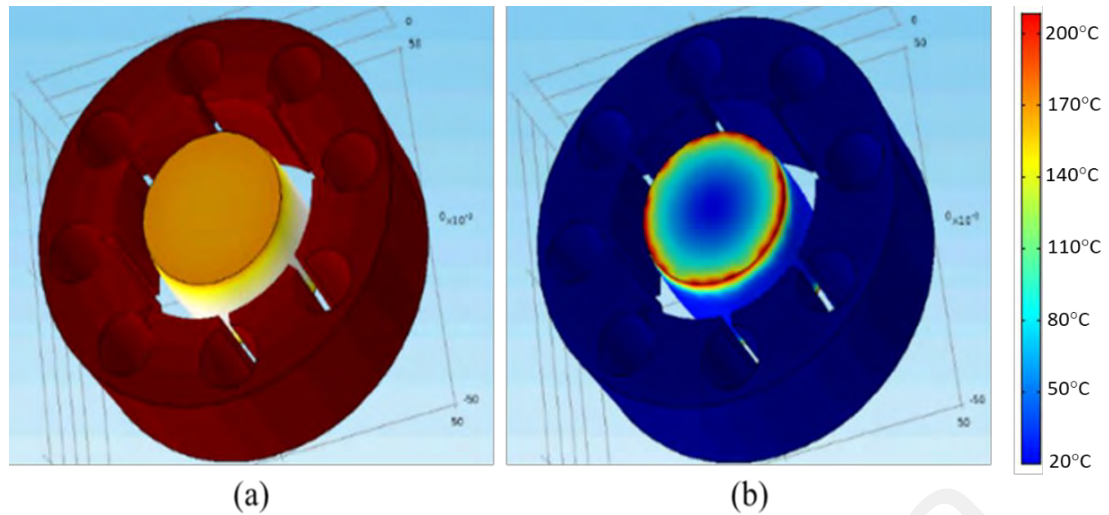


Figure 4.1: Heat density scale on magnetron model to generate 5W, 2.45GHz microwave power; a) BaO Substrate coated cathode, b) GaN and SiC Polymer coated cathode

Figure 4.1 refers to both materials' Resonant Electric Field (EF). The examined searched regular modes presence, from a cut plane, has been built on the magnetron transversal section and used to visualize the EF streamline. Figure 4.1 shows that GaN and SiC Polymer's coated EF are more directional than the BaO substrate. Non-directional EF consumes more energy, affecting its efficiency, while higher density EF gives better EMC circulation in the magnetron, as shown in Figure 4.2. The red circular motion shows the effectiveness of EF circulation.

Figure 4.2 illustrates the resonant EF streamline, which can be traceable from Figure 4.2 (b). The highlighted red arrow indicates that the EF streamline for GaN is directional and focuses on a critical point. At the same time, SiC EF streamlining is scattering and leads to power losses.

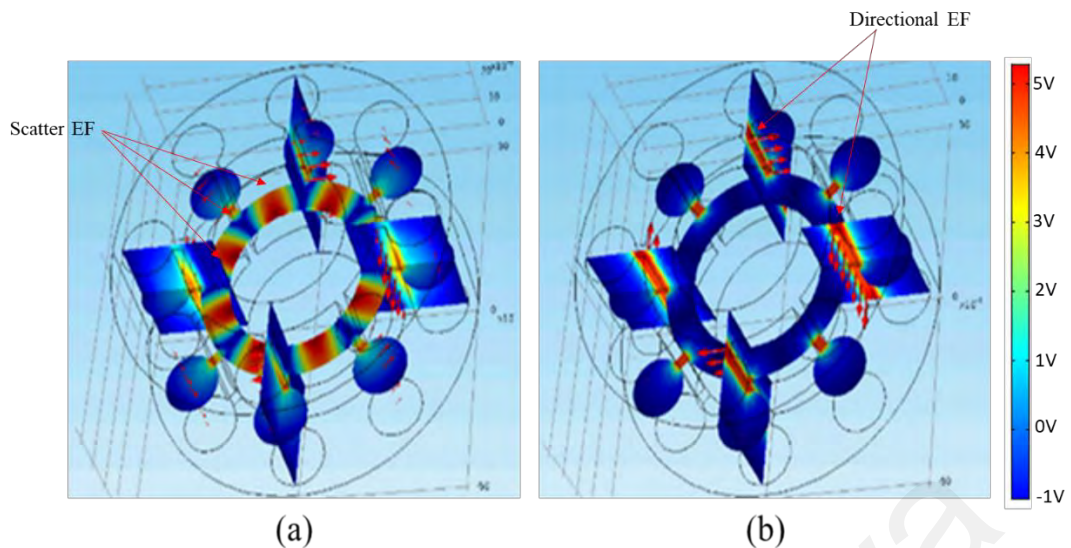


Figure 4.2: Resonant EF streamline, a) BaO coated, b) GaN and SiC polymer coated

Particle trajectories and the velocity in π mode are obtained from PT analysis. Two criteria were recorded for PT, cold and working conditions. The increase in maximum particle velocity is due to thermal excitation, which occurs in the magnetron. Maximum particle velocity magnitude recorded for cold condition is $V_{\text{Max-cold}}=2.338 \times 10^8 \text{m/s}$ and $V_{\text{Max-hot}}=2.478 \times 10^8 \text{m/s}$ for working condition. A maximum electrostatic field for cold conditions was recorded at $E_{\text{Max-cold}}=8.20 \text{MV/m}$ and $E_{\text{Max-hot}}=8.45 \text{MV/m}$ for thermal-stress working conditions. The simulation indicates that the best thickness of semiconductor polymer performance is at 100 nm. 100 nm is chosen based on the minimum thickness of the semiconductor polymer seed to full growth. Thickness less than 100 nm will expose the characteristic of BaO as the core is a BaO semiconductor. There is a slight difference between cold-condition and working conditions in particle velocity magnitude and electrostatic fields. The difference due to thermal stress can be neglected as the efficiency is not affected. The electrostatic field emitted for both conditions, shown in Figure 4.3, is almost incomparable. Therefore, GaN and SiC Substrate's coated magnetron cathode's stability and reliability for low voltage and high-frequency generation are validated.

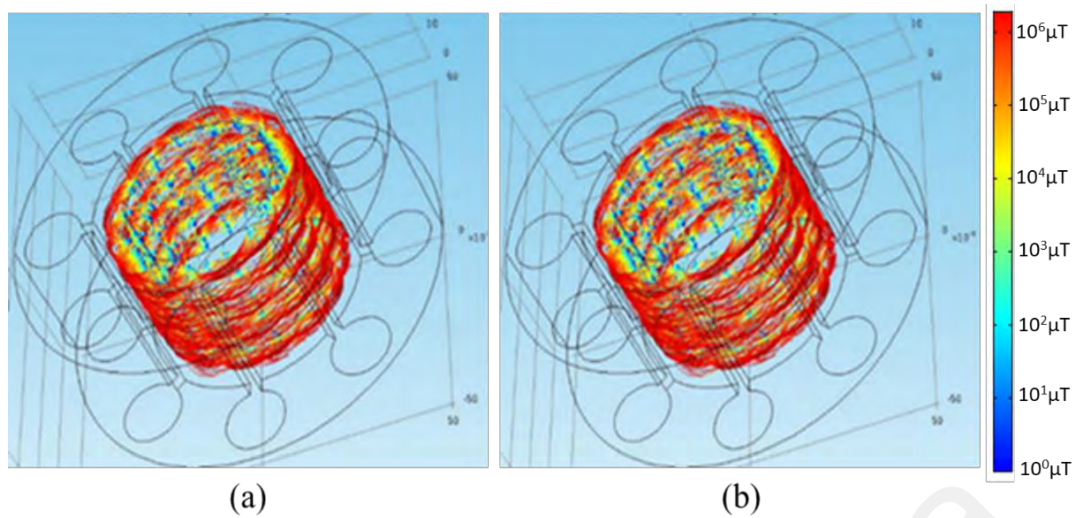


Figure 4.3: EMC performance analysis (a) Cold condition, (b) Working condition

The simulation performed in COMSOL has strongly justified that GaN and SiC Polymer's coated magnetron cathode performs better than BaO Substrate's coat.

4.3 Annealing Results

Polymer annealing on the magnetron's cathode surface using GaN Substrate and SiC Substrate semiconductor is targeted for low-power microwave power generation. Generally, a magnetron's cathode is made from solid metal, while a magnetron's anode is made from solid copper. Without going through the annealing process, the magnetron is suitable for high-power microwave generation with an efficiency of over 67% (Brown et al., 1963; Surducan et al., 2011). However, if the related magnetron is used to generate a low-power microwave, a significant loss is detected, lowering the efficiency of the microwave power generation.

Therefore, a confocal annealing process must be done to prepare the magnetron for low-power microwave generation. The confocal annealing process refers to two different substrates' exact temperature and annealing period to ensure perfect semiconductor growth on the magnetron's cathode. An unperfected annealing process exposes microwave power generation to explosion risk due to an unstable connection between the

magnetron's cathode and semiconductor polymer coating. In this case, it is essential to have a perfect annealing process on the surface with high-quality semiconductor deposition growth.

Figure 4.4 shows selected area diffraction on specific gallium material before any process started. This physical check is essential to ensure no contaminant sticks on the semiconductor surface. Figure 4.4 (a) shows the semiconductor purity and thickness in the SAED image. This case (0000) shows the GaN 100% pure without any contaminant or mixture of other types of material.

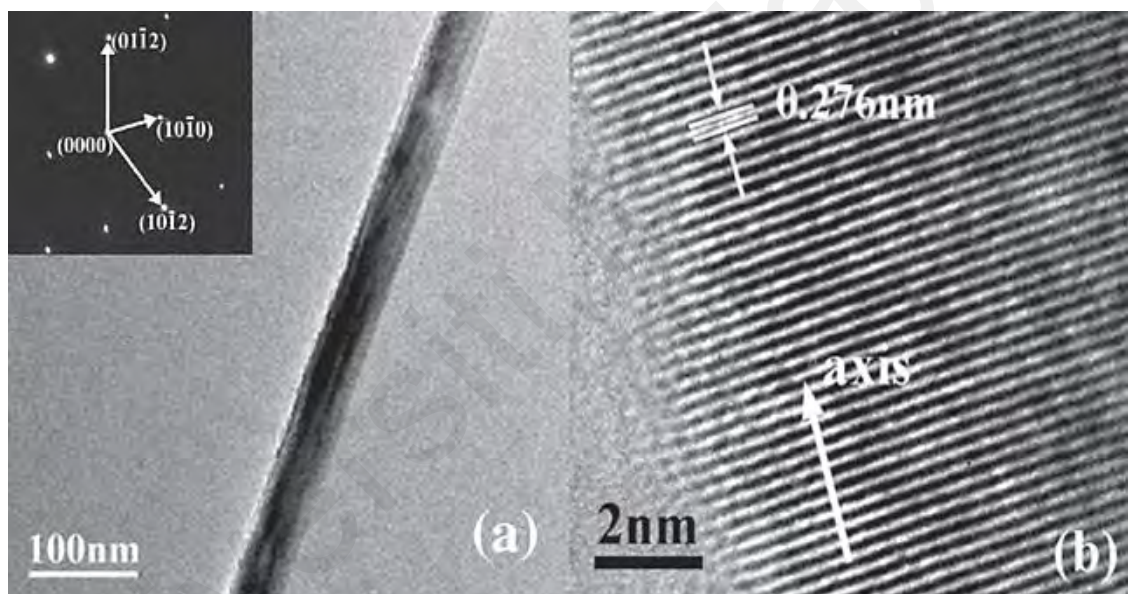


Figure 4.4: GaN substrate, (a) TEM and SAED images, and (b) HRTEM image

Figure 4.4 shows the TEM, selected area electron diffraction (SAED), and HRTEM images of an individual GaN substrate before the annealing process. The same check is performed for SiC, captured in Figure 4.5 (a), and proven no contaminant. The image is zoomed in with a 300nm ratio, while the HRTEM image is zoomed in at a 5nm scale. These materials are ready to be used in annealing by placing them on two different substrate plates.

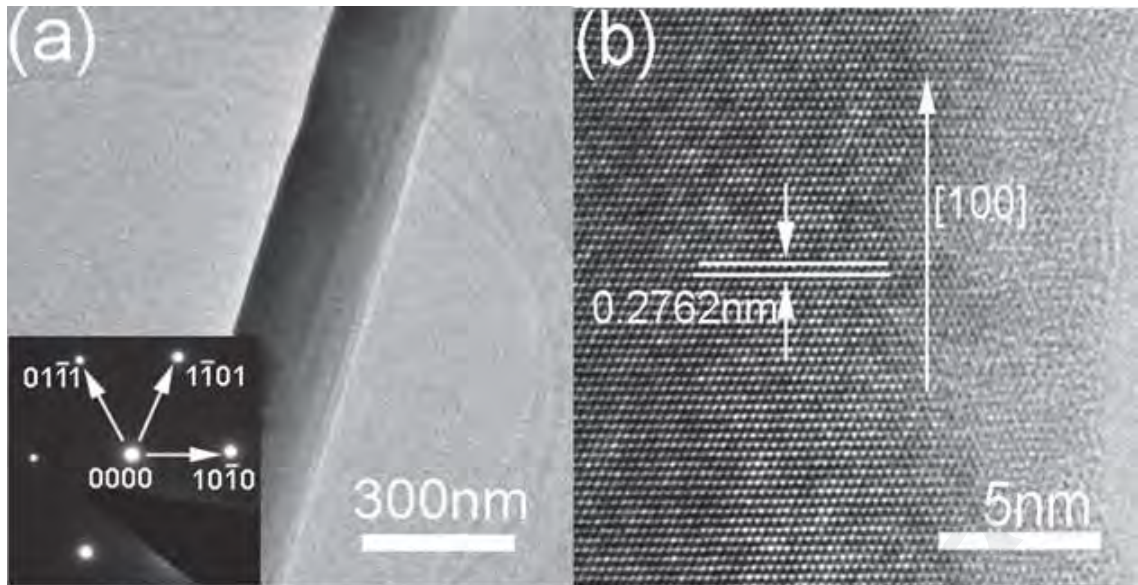


Figure 4.5: SiC substrate, (a) TEM and SAED images, and (b) HRTEM image

Figure 4.5 shows TEM, selected area electron diffraction (SAED), and HRTEM images of an individual SiC substrate. Both material annealing processes sputtered with different conditions to examine the best result. Several annealing timing processes and different deposition heating temperatures are done and physically analyzed under XPS and XRD scope before testing it on a magnetron to produce a low-power microwave. Figure 4.6 shows different zoom scales of cluster growth for GaN and SiC Polymer nanostructure at 1,200°C, which gives the best annealing result compared to other deposition temperature levels.

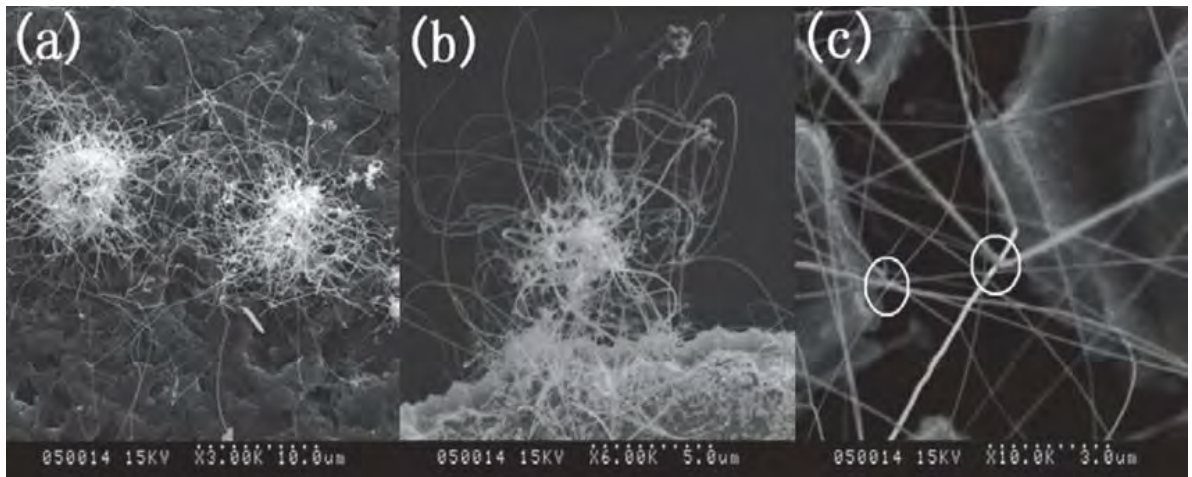


Figure 4.6: Cluster growth of one-dimensional GaN and SiC Polymer nanostructure of 100nm thickness, (a) XRD 3.00K zoom, (b) XRD 6.00K zoom, and (c) XRD 10.0K zoom

Figure 4.6 shows cluster growth of one-dimensional GaN and SiC Polymer nanostructure; (b) Magnification of local area in image (a); (c) SEM image of the single nanowire with nanoparticle on the tip. The image in Figure 4.6 (a) shows the bonding of each substrate in a specific area and can be seen clearly in the magnified image (b) the bonding of the lower parts (SiC) and the upper parts (GaN) is starting to transform into a polymer. Image (c) shows possible polymer growth where strong atom bonding is detected and reliable performance during high-temperature operations. There are no specific tests done for the magnetron's cathode that has been sputtered. Only physical XPS and XRD scope is used to evaluate the quality and rate of semiconductor deposition. These magnetron's cathodes are chosen, physically evaluated for quality, and assembled to the magnetron to generate a low-power microwave for experimental validation. After several deposition temperatures, GaN and SiC Polymer deposited using 1,200 °C are chosen as sample 1 due to better wire bonding between semiconductors, as in Figure 4.6 (c).

GaN and SiC Polymer deposited at 850 °C are chosen as sample 2. Figure 4.7 (a) shows the best deposition from the analysis and discussion due to the semiconductor

growth evenly. In contrast, no sample growth for GaN and SiC Polymer was deposited using 900 °C due to exceeding the melting point for a SiC. Figure 4.7 (c) shows that the sample loses its balance, leading to SiC evaporation.

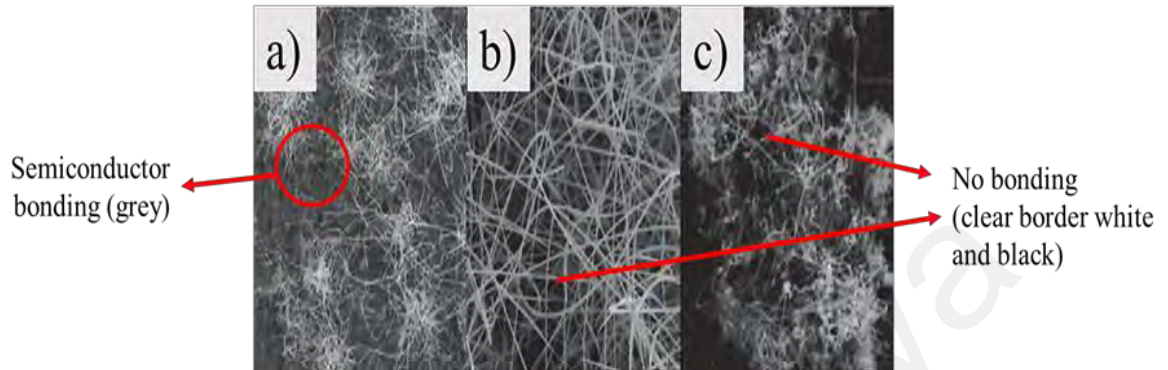


Figure 4.7: Samples grown at different temperatures, (a) 850°C, (b) 900°C, and (c) 950°C

Figure 4.7 shows SEM images of the GaN and SiC Polymer grown at different temperatures, (a) 850 °C, (b) 900 °C (c) 950 °C. While Figure 4.8 shows that GaN and SiC Polymers are grown at different periods, all four images were deposited at a fixed temperature of 850 °C. Figure 4.8 is the image from a typical SEM of Polymer grown for 5 minutes, (b) grown for 10 minutes, (c) grown for 15 minutes, and (d) grown for 20 minutes. The best result from the professional chemical engineer report is deposition at an average of 10 minutes because all semiconductor seeds (SiC and GaN) are wholly grown. While in Figure 4.8 (a), 30% of semiconductor seeds left ingrowth, (c) and (d) cause almost the same phenomena where all seeds start to be heated and absorbed by the magnetron's cathode into the metal.

Therefore, the deposition of semiconductors is performed for 10 minutes in the chamber and left to cool for 30 minutes before evaluating and assembling into a magnetron.

From analysis and research, the Ga melting point is at 29.77 °C. Deposition at 1,200 °C ensures perfect polymer growth on the magnetron's cathode surface without any uncovered surface of the magnetron's cathode metal. At the same time, the Si melting point is at 1,414 °C. A combination of both polymers changes the character of the material, and the polymer has a 2,730 °C melting point.

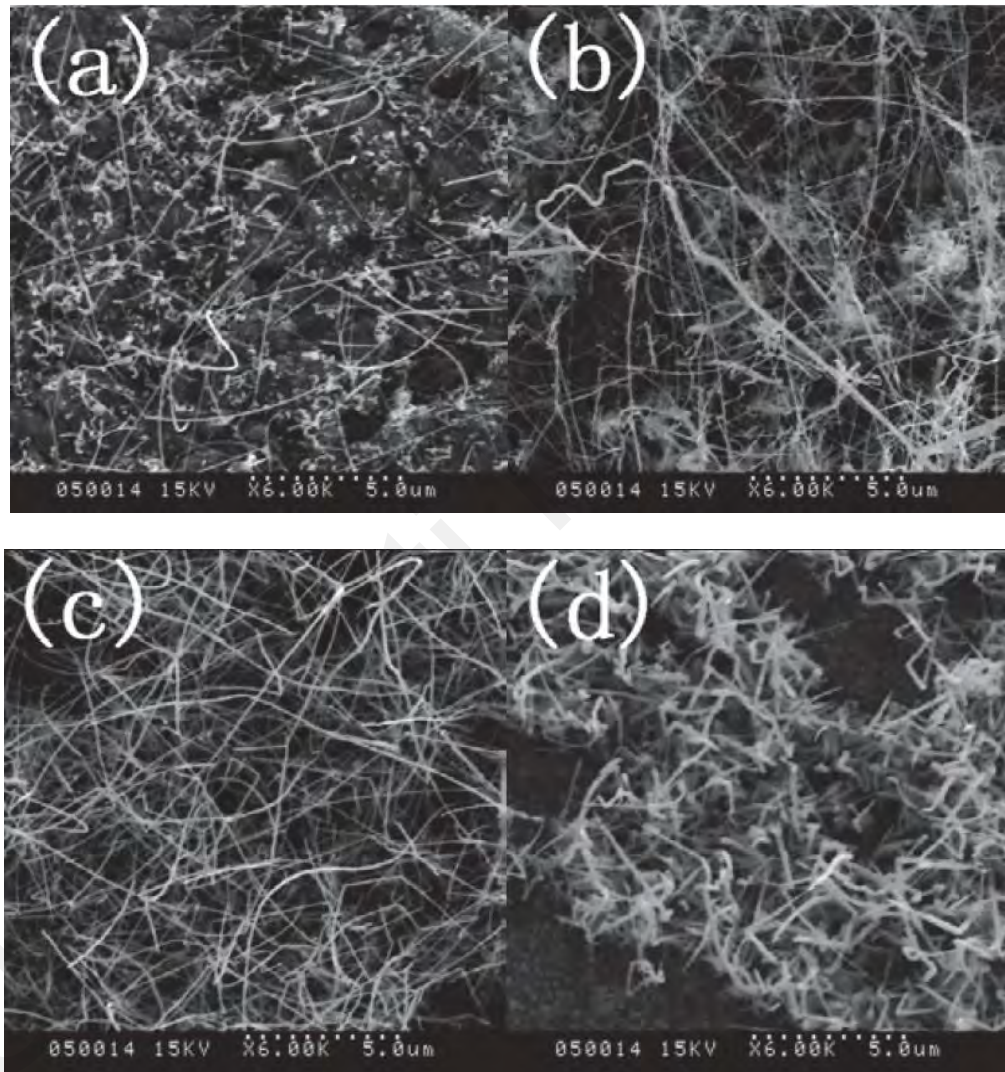


Figure 4.8: Polymer is grown at different periods, (a) 5 minutes, (b) 10 minutes, (c) 15 minutes, and (d) 20 minutes

A higher melting point ensures that the magnetron can generate microwave power safely. During microwave power generation, a strong coupling is required between the anode, cathode, and resonant cavity. This strong coupling produces heat commonly used in kitchen heating, exceeding the heating temperature of 300 °C. Therefore, materials

used in a magnetron must hold a high degree of temperature and have a high melting point to ensure their safety.

Different periods of semiconductor deposition produce different intensities. Figure 4.9 shows the intensity and wavelength produced after annealing at different heating temperature levels. The results are recorded after 15 minutes of heating in the deposition chamber. The label “a” represents the intensity for heating at 850 °C, which is the desired temperature for perfect annealing with medium-level intensity. Label “b” with high intensity was heated at 900 °C, and label “c” with heating at 950 °C had low intensity due to near semiconductor evaporating temperature. All annealing results are recorded between 275 and 650nm at the same wavelength.

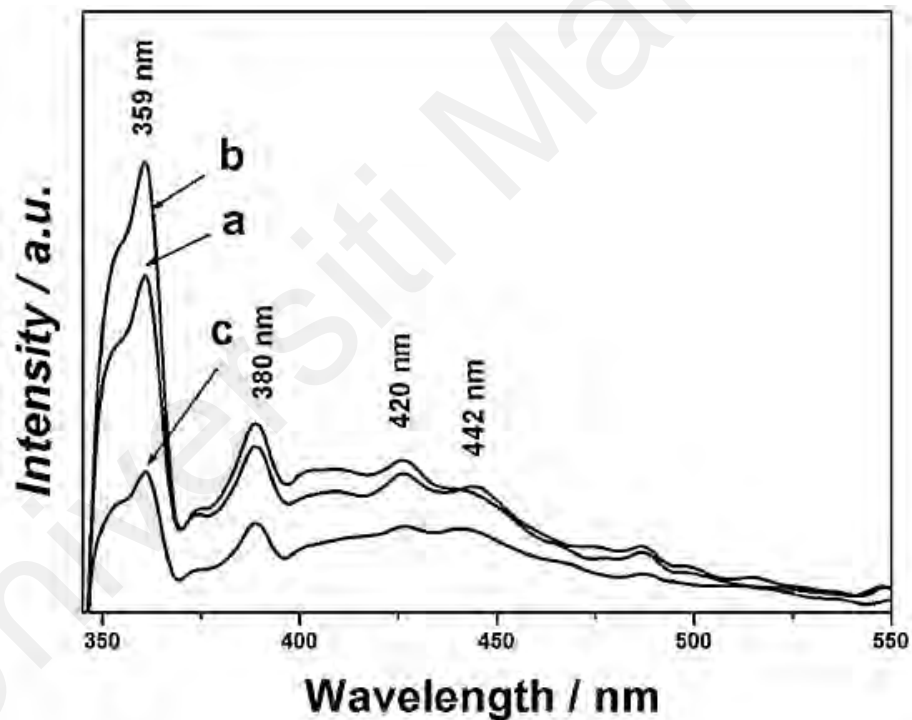


Figure 4.9: Photoluminescence spectrum of samples ammoniated at different temperatures

Another parameter of consideration to ensure better semiconductor seed deposition is the thickness of the plasma layer growth. A surface profilometer regulates the thickness of quartz crystal microbalance (QCM). Before placing the semiconductor seed, the surface profilometer, located under the seed plate, was calibrated to determine the

thickness of seed deposition and estimate the deposition rate. However, there is no specific calibration for temperature, and the deposition period differs in this experiment.

4.4 Experimental Validation

There are two types of efficiency identified in this work to verify the proposed solutions, 1) the Magnetron's efficiency ($\eta_{\text{magnetron}}$) and 2) the System's efficiency (η_{system}). As illustrated in Figure 4.4, the power supply output, the magnetron output, and the receiver has been tested with a 5Ω resistive load to measure the output power. A lower load is used in this experiment after considering the internal resistance and impedance of the battery charging system in a standard mobile phone (Bose & Laman, 2000; Brendt & Voss, 1964; Peng, 2011; Suozzo, 2008; Takeno et al., 2004; Wang et al., 2021). The output power is used to determine the efficiency. The voltage, current, power, and efficiency results are tabulated in Table 4.1. The Magnetron's efficiency is calculated using (4.1), where P_{in} refers to the power supplied to the magnetron input in Watt (W) and P_{out} refers to the power measured at the magnetron's output in Watt (W).

$$\text{Magnetron's efficiency, } \eta_{\text{magnetron}} = \frac{P_{\text{out}}}{P_{\text{in}}} \times 100\% \quad (4.1)$$

It is also essential to determine the system's efficiency, including the magnetron, transmitter, and receiver, to identify the losses during the wireless power transmission characteristics due to the difference in EF streamline from the simulation performed. Therefore, the system's efficiency is calculated using (4.2) by accounting for P_{in} as the power supplied to the magnetron in Watt (W), and P_{rxout} is the power measured at the receiver in Watt (W).

$$\text{System's efficiency, } \eta_{\text{system}} = \frac{P_{\text{rx}}}{P_{\text{in}}} \times 100\% \quad (4.2)$$

The GaN and SiC polymer magnetron's cathode EF streamline propagates higher than the BaO material. Higher directional propagation of EF streamline leads to better transmission quality and a higher possibility that the power is fully captured in the receiving antenna. On the other hand, the omnidirectional characteristic of BaO material propagation leads to inadequate coverage and high losses, as recorded in Table 4.1. There are approximately 64% of power losses from the transmitter for BaO material compared to GaN and SiC polymer, with 13% losses in the same experimental setup.

Table 4.1: Experimental Results

Measured parameter	BaO coated	Proposed solution
Magnetron input voltage, V_{in}	5V	5V
Magnetron input current, I_{in}	1A	1A
Magnetron input power, P_{in}	5W	5W
Magnetron output voltage, V_{out}	3.6V	4.7V
Magnetron output current, I_{out}	0.72A	0.94A
Magnetron output power, P_{out}	2.59W	4.418W
Received voltage, V_{rx}	3.6V	4.7V
Received current, I_{rx}	0.26A	0.82A
Received power, P_{rx}	0.93W	3.84W
Operating frequency	2.45GHz	2.45GHz
Magnetron's efficiency, $\eta_{magnetron}$	51.8%	88.36%
System's efficiency, η_{system}	18.6%	76.8%

The Magnetron's efficiency for GaN and SiC polymer material is expected to be higher than BaO material by analyzing the magnetron's heat dissipation. It is validated through analysis, simulation, and experimental results. As simulated earlier, a higher electron drift velocity in BaO materials results in higher heat dissipation. In addition, the experimental results observe the operating temperature of the GaN and SiC polymer to be maintained below 65°C without triggering the thermo-switch over a long period of microwave power generation.

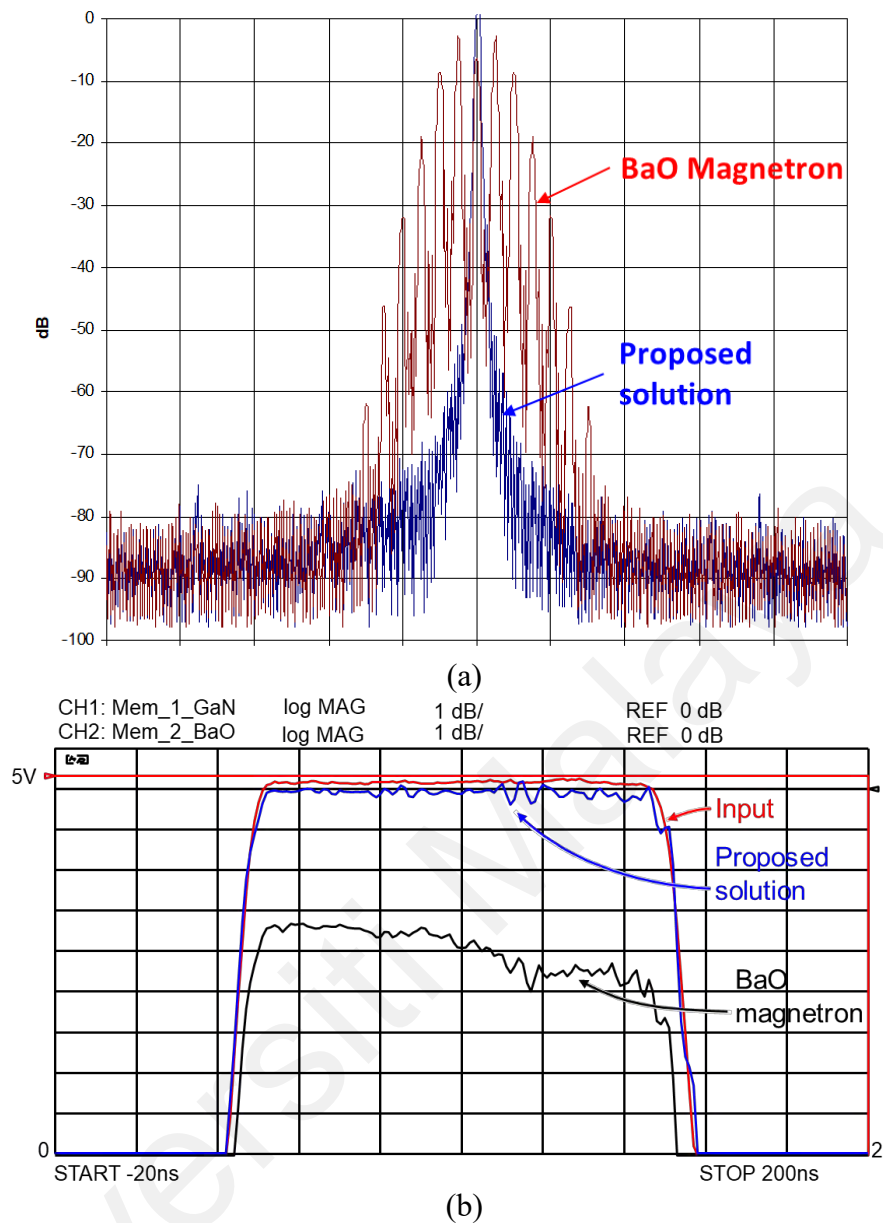


Figure 4.10: Performance comparison; a) measured output spectrum, b) measured received voltage by battery

An additional test is carried out to charge the portable communication device battery, and the result is tabulated in Table 4.2. The charging test was performed in three wireless and wired charging conditions to charge a drained battery. The drained battery voltage is observed at 2.8V before being connected to the System for wireless charging. Considering conventional wire charging as an ideal rate, GaN and SiC polymer coating has raised the charging efficiency by 51% compared to the BaO-coated magnetron cathode. The voltage supplied to the magnetron for both types of material remains the same at 5V and 2.45GHz.

As observed, the BaO coating requires a longer time to charge a 3,500mAh battery in static charging conditions.

Figure 4.10 shows the performance comparison between BaO Substrate, GaN and SiC Polymer coat used. The spectrum analyzer shows that the carrier frequency output from BaO Substrate coated magnetron cathode produces small losses even before the transmission is undertaken. At the same time, GaN and SiC Polymer are more promising in terms of voltage stability. The spectrum of the BaO Substrate was recorded -3dBW lower than the GaN and SiC Polymer at the peak, reflecting a gap of around 0.5W. The output captured at the receiver while charging the battery shows that the BaO Substrate magnetron produces a maximum distortion of 1.4Vpp. Alternatively, GaN and SiC Polymer voltage are smoother, with a maximum distortion recorded less than 0.3Vpp, which is in good agreement with the magnetron's measured input voltage.

As depicted earlier, the operating temperature rise strongly influences a magnetron's efficiency. However, a shorter period for the magnetron to achieve optimum temperature operation is also essential. Figure 4.11 shows the GaN and SiC Polymer plot achieving an optimum operating temperature faster than the BaO Substrate. Unfortunately, the BaO Substrate temperature keeps rising and causes the thermo-switch to snap at more than 65°C after 23 seconds of the microwave generation. In the earlier experiment, the thermo-switch is calibrated to snap at 65°C to test each magnetron's performance. The thermo-switch is bypassed to prevent the activation of the magnetron cooling system. Further investigation to examine BaO Substrate and, GaN and SiC Polymer performance characteristics are undertaken.

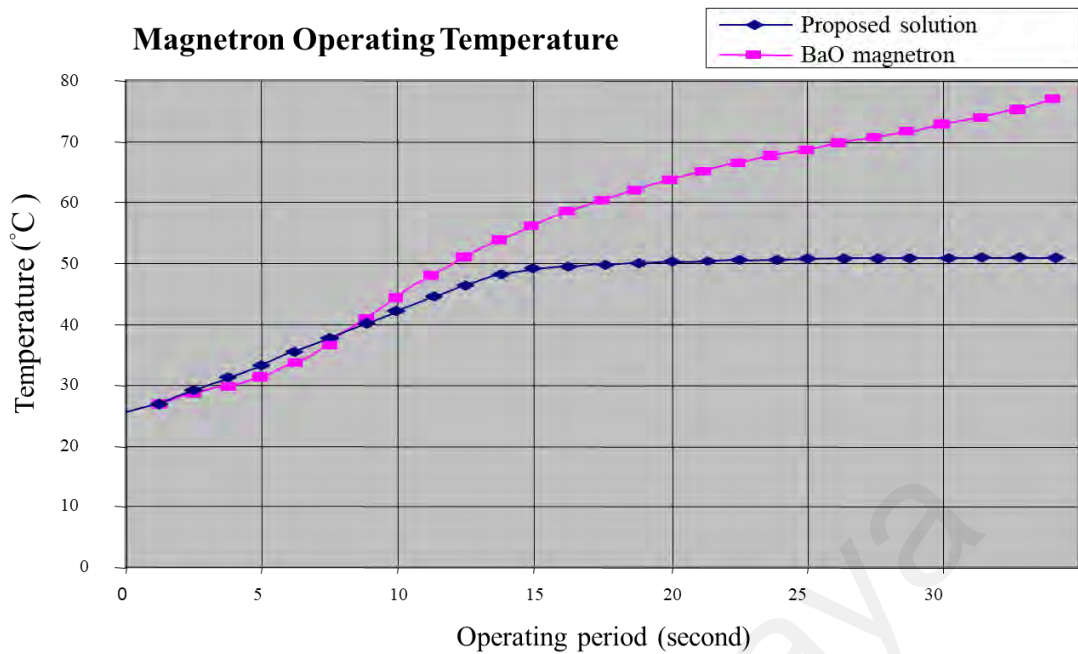


Figure 4.11: Magnetron temperature during operation

Table 4.2 shows the experimental result in conditions of wireless and wired charging applications by considering conventional wire charging as an ideal charging rate. GaN and SiC Polymer coating has increased efficiency by 51% compared to BaO Substrate's coated magnetron's cathode. The voltage supplied in both types of material remains the same at 5V and 2.45GHz. As expected, the BaO Substrate coating requires a longer time to charge a 3,500mAh battery in static charging conditions.

Figure 4.12 shows the magnetron performance for each material by analyzing the generated output. Initially, the difference in performance for the generated voltage is recorded at 0.4V between each material. However, as the voltage increases, the voltage gap becomes more expansive. BaO magnetron produces a higher percentage of voltage losses due to the increases in heat density for BaO magnetron, as recorded in Figure 4.12. GaN and SiC polymer magnetrons perform better as the voltage increases due to the magnetron achieving its stability and controlled heat density. Therefore, it can be concluded that GaN and SiC perform better with the input voltage increase than the BaO material, which produces higher voltage losses as it increases.

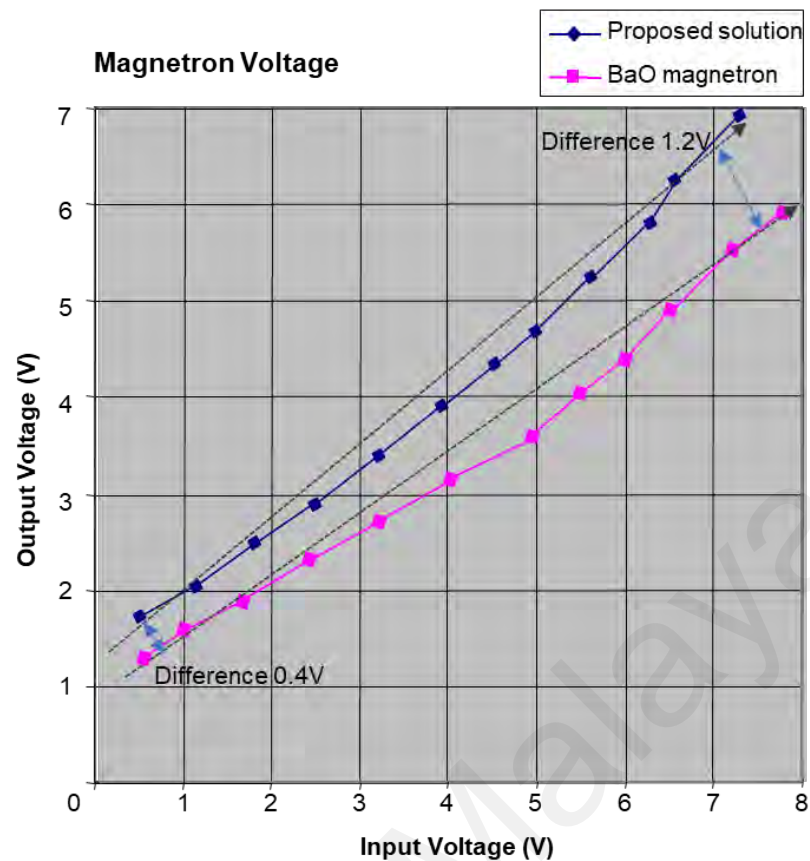


Figure 4.12: Magnetron input and output voltage

Charging by using BaO Substrate coated magnetron cathode gives an unstable voltage at the receiver ranging between 2.2V to 3.6V $V_{\text{peak-peak}}$ distortion. This distortion occurs due to the heat generated by the electron movement. Temperature rise is one of the main factors identified earlier, which causes the magnetron to lose its stability. It is essential to have a system that produces less distortion, even though it can be eliminated through filtering. Filtering a higher distortion voltage shortens the lifespan of filtering components, leading to a waste of energy (Cohn, 1959; Liu et al., 2017; Shen et al., 1997; Sivadas et al., 2000; Tang et al., 2011).

Table 4.2: Experimental result in three conditions for wireless charging and wired charging applications

Charging method	Tx. Distance	Voltage Received (receiver)	Charging time (minutes) 3,500mAh	Thermo-switch snap time (>65°C)	Efficiency
BaO coated cathode	10 m air-gap	2.2~3.6V (unstable)	336	23 seconds	36%
Proposed solution	10 m air gap	4.7V	231	never	87%
Wire charging	1 m wired	5V	205	not in use	99%

Due to the limitation of testing peripherals, the magnetron's total capacity is not verified (6kW, 2.45GHz) based on the microwave power generation datasheet (*CW Magnetron Sintering Thawing Datasheet*, 2015). Therefore, additional verification in line with safety and health is not conducted. However, as stated in the datasheet by the magnetron's manufacturer (*CW Magnetron Sintering Thawing Datasheet*, 2015), the magnetron can achieve 72% efficiency using BaO Substrate coated cathode for 6kW power generation. Therefore, the proposed solutions using the GaN and SiC Polymer's coated cathode are suitable for low power generation, and instability is used to generate high power. Alternatively, BaO Substrate's coated cathode is designed to perform high-power generation. The magnetron is excessively conducted for low power generation, leading to temperature rise due to EMC leakage.

4.5 Analysis and Comparison

Analysis and comparison in this section involved additional simulation and experimental verification towards different power ratings of conventional BaO magnetron to better understand the characteristics and behaviors. Comparison is also performed with other types of magnetron from recently published works available with a similar approach with proposed solutions.

4.5.1 Comparison with Various Magnetron Rating

This section details the simulations and experimental results over a high-power BaO magnetron with a maximum rated power of 6kW. This section compares a lower power rating BaO magnetron with a maximum rated power of 900W (model: 2M219J series).

Simulation in COMSOL is carried out with the same configuration of 5W microwave power at 2.45GHz input for all magnetron materials, as in Figure 4.13. In addition, the magnetron used model has been modified from the existing BaO model by applying the parameter, specification, and measurement for low-power BaO magnetron from the datasheet provided by the manufacturer. The comparison can be visually seen from the heat density scale generated through the simulation. The proposed system gives higher heat stability compared to the conventional BaO material. Using a high-power BaO magnetron for microwave power generation caused high heat density in the anode with more than 80°C for more than 5 minutes. The anode's high heat density caused the magnetron to lose its stability and lead to high power generation loss.

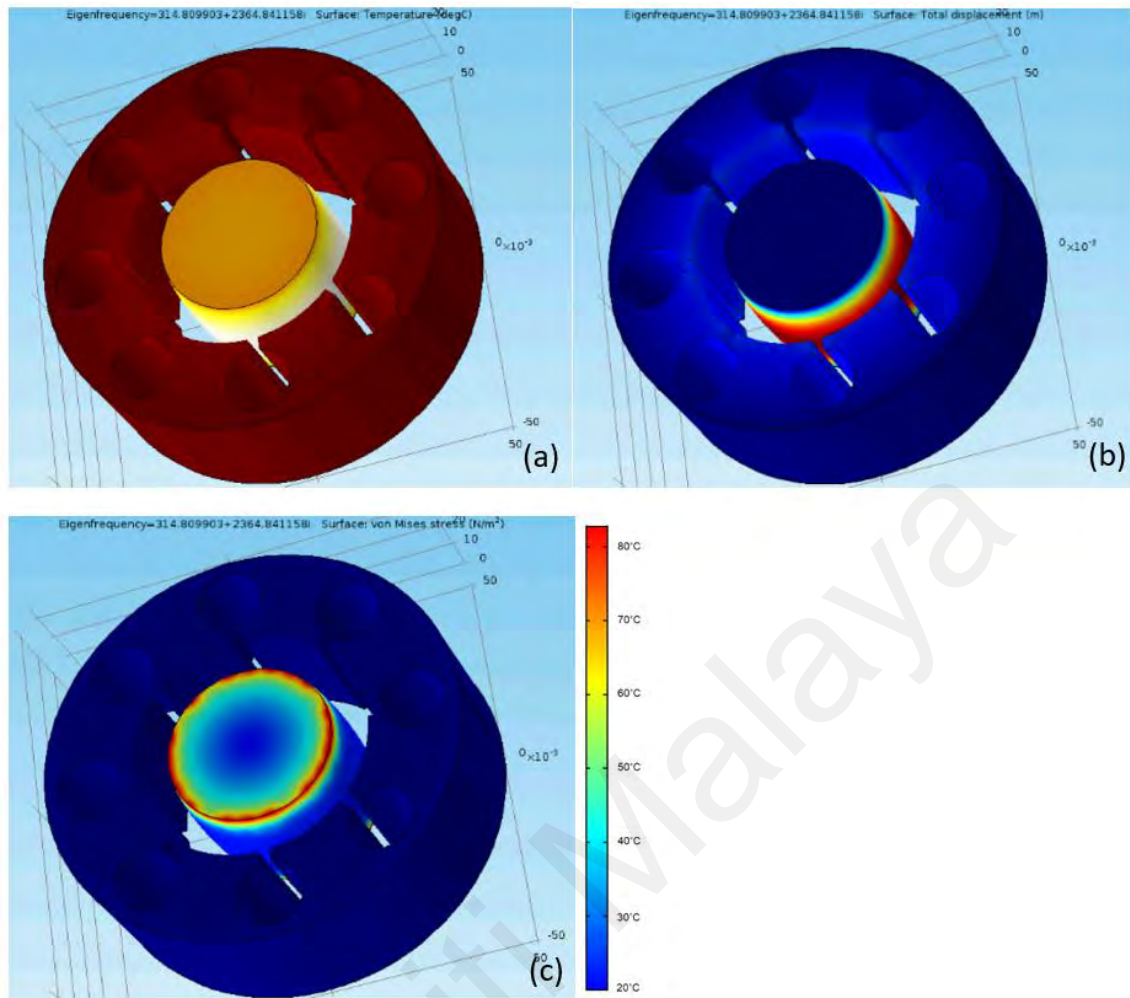


Figure 4.13: Heat density scale on magnetron model to generate 5W, 2.45GHz microwave power. a) High Power BaO Magnetron (rated 6kW), b) Lower Power BaO Magnetron (rated 900W), and c) Proposed solution

However, using a low-power BaO magnetron, a maximum of 80°C is captured on the cathode surface while the anode does not produce abnormal heat behavior. The drawback of having a high heat density cathode is that it triggers the Thermo switch attached to the magnetron and activates the cooling system, consuming higher operation power and creating a shorter lifespan of a magnetron. The proposed solution can encounter high and low-power BaO magnetron issues. As mentioned earlier, heat density in a magnetron is the main factor for achieving a high-efficiency magnetron.

Next, additional experimental verification is carried out to validate further the simulation performed earlier to examine the magnetron characteristic in terms of power

quality and generated microwave power using the same setup. The results shown in Figure 4.14 are measured at the magnetron output with a constant input of 5V at 2.45GHz. Low power BaO magnetron performs slightly better than the high-power BaO magnetron in oscillation. Without any load connected to the magnetron, a high-power BaO magnetron produces 28% voltage loss, while a low-power BaO magnetron only produces 14% voltage loss. However, the proposed system in this work performs even better than the conventional BaO magnetrons with only 6% voltage loss due to a few factors, such as internal impedance from the magnetron measured at 0.84Ω and power consumed by the thermo-switch.

Therefore, realizing the difference of oscillation captured at the magnetron output using an oscilloscope, a further investigation of the noise produced by each magnetron is performed. The experiment is carried out in an anechoic chamber to avoid exposure to microwave power and capture that the actual noise produced is 100% original from the magnetron itself. Figure 4.15 shows the output of a spectrum analyzer for a low-power BaO magnetron and the proposed solution magnetron. The BaO produces higher noise, as in Figure 4.15 (a), compared to GaN and SiC Polymer, as in Figure 4.15 (b), during the oscillation.

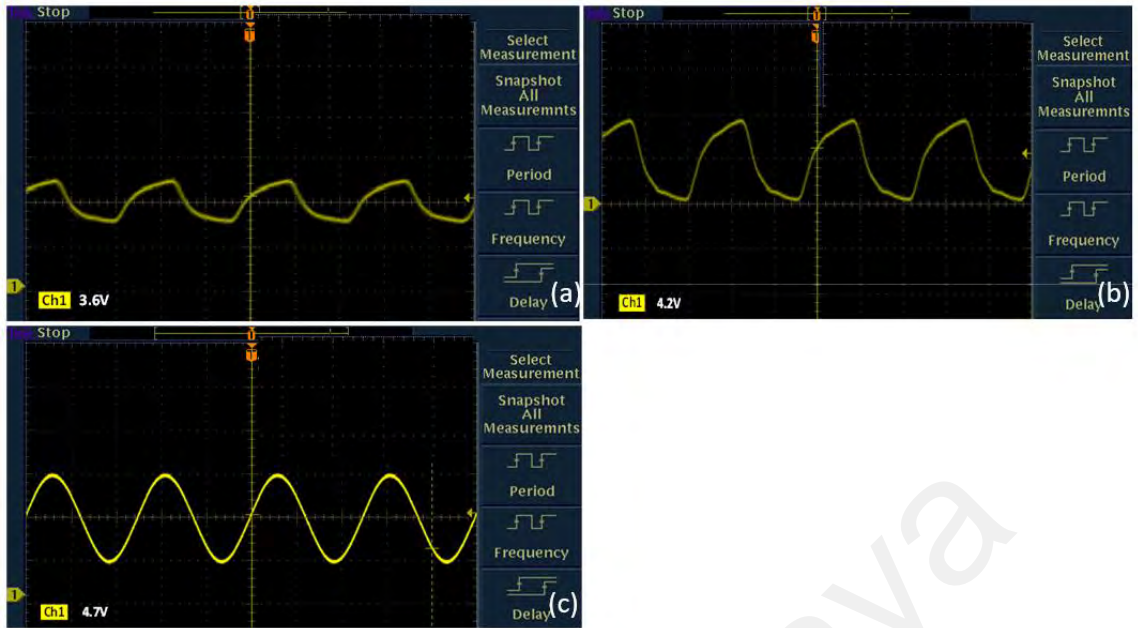


Figure 4.14: Magnetron output with 5W, 2.45GHz input. a) High Power BaO Magnetron (rated 6kW), b) Lower Power BaO Magnetron (rated 900W), and c) Proposed solution

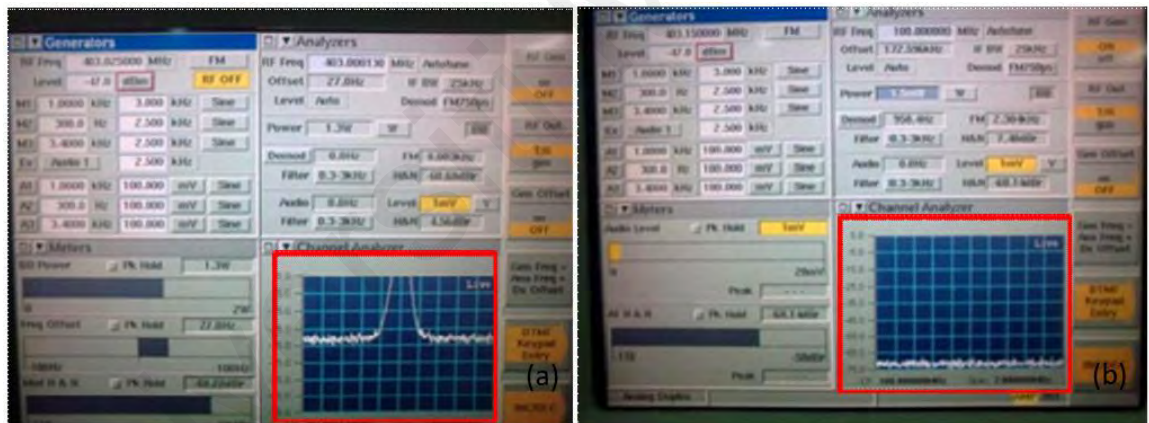


Figure 4.15: Noise captured by a spectrum analyzer. a) BaO magnetron and b) Proposed solution

The proposed system produces lower noise compared to a low-power BaO magnetron. However, noise for high-power BaO magnetron cannot be captured as the noise produced exceeds the limits measurable by the spectrum analyzer. Therefore, based on the voltage output captured from the oscilloscope earlier, it can be concluded that a high-power BaO magnetron produces higher noise than a low-power BaO magnetron.

A system with less noise is preferred to avoid disturbance to other components in a mobile phone, such as the VCO and power amplifier, or even to nearby devices, such as healthcare wearables, network sensors, and communication equipment.

The test bench is constructed in an anechoic chamber for safety purposes, and the setup does not favor background temperature variation in an intimate environment. However, based on the simulation and experimental measurement, the proposed solution magnetron can operate naturally below the temperature of 50°C generating 5W at 2.45GHz with power transmission of up to 60 minutes.

4.5.2 Comparison with Recent Works

A comparative analysis is summarized in Table 4.3 to compare recent work with a similar approach as the proposed solution. However, no detailed comparison analysis can be performed due to the novelty of the proposed solution. Thus, a comparative analysis is performed with the closest similarity and conventional systems. The proposed solution's efficiency is enhanced by approximately 50% by introducing the GaN and SiC Polymer material coating and the efficiency due to temperature rise. This trade-off defines the GaN, and SiC Polymer's coated cathode is no longer suitable for generating high power, with the BaO Substrate's coat preferred. However, no apparent solution has been reported to the described trade-off.

Table 4.3: Comparative analysis

Generator model and type	Reference	Frequency	Power	Efficiency
CK-625, 6kW, 2.45GHz Microwave Heating Sintering Thawing Continuous-Wave (CW) magnetron – GaN and SiC polymer coated magnetron cathode	Proposed method	2.45GHz	5W	88.37% (Generator) 76.8% (System)
CK-625, 6kW, 2.45GHz Microwave Heating Sintering Thawing Continuous-Wave (CW) magnetron – BaO coated magnetron cathode	Conventional (before implementation)	2.45GHz	5W	51.8% (Generator) 18.6% (System)
New BLF6G10, Dual microwave generator (Surducan & Surducan, 2013)	Vasile Surducan and Emanoil Surducan (2013)	905MHz to 918MHz	1.5W to 60W	44.7% to 45% (Generator)
Water-cooled CW CK-2091 magnetrons (Liu et al., 2018)	Zhenlong Liu, Xiaojie Chen (2019)	2,110MHz	500kW	48% (Generator)
2.45GHz-Band 250W, Feedback-type GaN-HFET Oscillator using Imbalanced Coupling Resonator Microwave Generator (Ikeda & Itoh, 2019)	Hikaru Ikeda and Yasushi Itoh (2019)	2.45GHz	5W to 263W	61.3% (Generator)
Traveling-wave tube for the communication satellite "Symphonie" (Bretting & Klein, 1969)	J. Bretting and W. Klein (1969)	3.7GHz – 4.2GHz	12W	38% (System)
Thales 150 W C-Band radiation cooled Travelling Wave Tube (Dürr et al., 2015)	W. Dilrr, C. Dilrr, P. Ehret, E. Bosch (Thales Electronics (2015)	3.4GHz – 4.2GHz	150W	74% (Generator)

Depending on its application and implementation, there are a few methods to enhance a magnetron's efficiency. A reliable and stable magnetron controls the operation's heat density and temperature rise.

The method proposed in this paper shows a significant increase in efficiency compared to other methods, including increasing the resonant cavity, enlarging operation space size, and modifying the anode structure. The listed method has only one aim: to control the operating temperature affecting efficiency by modifying the electron flow velocity.

Universiti Malaysia

CHAPTER 5: CONCLUSION AND RECOMMENDATION

5.1 Conclusions

A magnetron is commonly used to generate a high-power microwave for heating purposes and transmit a high-power microwave. However, some modifications must be done to prepare magnetron for low-power microwave transmission. Transmitting a low-power microwave requires a stable operating temperature and clean carrier frequency supply to avoid hum and noise in a microwave. At the same time, the magnetron needs to be modified using specific semiconductors for different applications.

The electron drift velocity performed by considering the cross-sectional magnetron cathode showed the different speeds of Fermi flow velocity. BaO recorded 1,570,000m/s, and proposed solution recorded 854,000m/s. The lower speed of Fermi flow velocity represents lower friction between electrons and produces lower heat density for the same cross-sectional area.

The simulation performed in COMSOL are in favor of the analysis. The proposed solution's heat density is more stable than the conventional magnetron, where the heat density is high at the anode structure due to the magnetic field occurring during the operation. Moreover, the EF streamline for the proposed solution are more directional than the conventional one, which is scattered and leads to high power loss. There is no difference captured in EMC performance for both materials. Thus, the proposed solution can generate microwave power with better heat density.

The magnetron's cathode has been annealed using GaN and SiC Polymer, and these semiconductors are grown through a deposition system at various temperatures and deposition periods. The annealing system is designed based on the conventional sputtering system. Different semiconductor deposition temperatures have been conducted and proposed the best deposition for GaN and SiC polymer annealing at 850°C.

The proposed solution for improving the low-power microwave generation's efficiency using 6kW, 2.45GHz Sintering Thawing CW magnetron is demonstrated in this thesis. The SiC and GaN Polymer's coated cathode in the magnetron operates with an output power of 5W with an efficiency of 87% has been successfully achieved at 2.45GHz. In comparison, the conventional coated BaO Substrate's cathode achieves 36% efficiency. Simulation to analyze the magnetron stability and experimental validation has proven the hypothesis. The result concludes that the solution would be a promising methodology for realizing the next generation of modulated microwave power transmission for mobile charging applications.

The comparison analysis has set the proposed solution as a benchmark among similar optimization approaches. The proposed solution gives higher generator efficiency as well as system efficiency.

The implication of the proposed solution can be implemented in long-distance mobile phone wireless charging. It can be used widely in a public area as the operating parameter complies with the health and safety regulation in Table 2.1. The proposed solution also can be applied to the healthcare wearable, wireless sensor networks, and long-distance dynamic wireless power transmission. By referring to the Appendices, the proposed solution prototype has been successfully tested on-site with long-distance communication device charging.

The annealing system has been set up to perform semiconductor deposition. The experimental verification is validated according to the hypothesis made earlier in the analysis and simulation.

5.2 Novelty and Contribution

The novelty of the work in this thesis refers to implementing a new semiconductor polymer GaN and SiC over conventional solid BaO magnetron's cathode for generating low-power, high-frequency microwave power in higher efficiency. Such work is the first reported and experimentally validated. This contributes to wireless power charging for mobile devices up to 10 meters.

5.3 Recommendation

It is found that semiconductor usage in power devices, not only magnetron, has significantly increased its efficiency. However, the GaN and SiC Polymer combination is suitable for high-frequency and low-power applications. At the same time, BaO Substrate is suitable for low-frequency and high-power applications. It is proven that different types of semiconductors react differently. It is recommended to perform further research to determine suitable semiconductor works for high frequency and high power applications and low frequency and low power applications.

Based on the outcome and contribution of the proposed solution magnetron, it is strongly recommended that the BaO magnetron be sputtered or annealed with other high-potential semiconductors such as Iridium, Germanium, Selenium, and organic semiconductor or a mixture of polymers. Each material has different characteristics when implemented in a power device. However, such research expects to consume expensive equipment and raw materials in material preparation.

Implementing different semiconductors in power devices such as magnetrons without proper procedure is risky. Therefore, such devices require extra safety and protection. Therefore, it is also recommended to design a safety apparatus or protection utility device attached to the power device for precaution.

Other optimization can be performed by modifying the magnetron structure, such as enlarging the operation space, the magnetron's cathode size, and several resonant cavities. Modifying magnetron structure is without simulation, and knowledge is harmful due to changes in characteristics and operation.

Universiti Malaya

REFERENCES

- (M), M. S. (2015). *Semiconductor fabrication and sputtering procedure book 2015*.
- Arjavalingham, G., Pastol, Y., JM, H., & Kopcsay, G. (1989). Application of picosecond optoelectronics in broadband microwave material measurements. *Microwave Journal*, 32(11), 133-138.
- Arnell, R. D., & Kelly, P. J. (1999). Recent advances in magnetron sputtering. *Surface and Coatings Technology*, 112(1-3), 170-176.
- Blaylock, R. L. Dr. Blaylock on Chemtrails.
- Blazey, K., Müller, K., Bednorz, J., Berlinger, W., Amoretti, G., Buluggiu, E., Vera, A., & Maticotta, F. (1987). Low-field microwave absorption in the superconducting copper oxides. *Physical Review B*, 36(13), 7241.
- Blazey, K., Portis, A., & Bednorz, J. (1988). Microwave study of the critical state in high-Tc superconductors. *Solid state communications*, 65(10), 1153-1156.
- Bollen, G., Moore, R., Savard, G., & Stolzenberg, H. (1990). The accuracy of heavy-ion mass measurements using time of flight-ion cyclotron resonance in a Penning trap. *Journal of Applied Physics*, 68(9), 4355-4374.
- Boot, H., & Randall, J. (1946). The cavity magnetron. *Journal of the Institution of Electrical Engineers-Part IIIA: Radiolocation*, 93(5), 928-938.
- Boot, H. A., & Randall, J. T. (1976). Historical notes on the cavity magnetron. *IEEE Transactions on Electron Devices*, 23(7), 724-729.
- Bräuer, G., Szyszka, B., Vergöhl, M., & Bandorf, R. (2010). Magnetron sputtering—Milestones of 30 years. *Vacuum*, 84(12), 1354-1359.
- Bretting, J., & Klein, W. (1969). Traveling-wave tube for the communication satellite "Symphonie.". *Journal of Spacecraft and Rockets*, 6(3), 285-288.
- Brown, W., Mims, J., & Heenan, N. (1966). An experimental microwave-powered helicopter. 1958 IRE International Convention Record,
- Brown, W., Skowron, J., MacMaster, G., & Buckley, J. (1963). The super power CW amplatron. 1963 International Electron Devices Meeting,
- Brown, W. C. (1973). Satellite power stations: A new source of energy? *IEEE spectrum*, 10(3), 38-47.
- Brown, W. C. (1977a). Electronic and mechanical improvement of the receiving terminal of a free-space microwave power transmission system.
- Brown, W. C. (1977b). Electronic and mechanical improvement of the receiving terminal of a free-space microwave power transmission system. *NASA STI/Recon Technical Report N*, 77, 31613.

- Brown, W. C. (1980). Solar power satellite program rev. DOE/NASA satellite power system concept develop. Evaluation program. Final Proc. Conf,
- Brown, W. C. (1981). Status of the microwave power transmission components for the solar power satellite. *IEEE transactions on Microwave Theory and Techniques*, 29(12), 1319-1327.
- Brown, W. C., & Eves, E. E. (1992). Beamed microwave power transmission and its application to space. *IEEE transactions on Microwave Theory and Techniques*, 40(6), 1239-1250.
- Caloz, C., Okabe, H., Iwai, T., & Itoh, T. (2002). Transmission line (TL) approach of left-handed (LH) materials. In *Electrical Engineering Department University of California*.
- Canali, C., Jacoboni, C., Nava, F., Ottaviani, G., & Alberigi-Quaranta, A. (1975). Electron drift velocity in silicon. *Physical Review B*, 12(6), 2265.
- Canali, C., Majni, G., Minder, R., & Ottaviani, G. (1975). Electron and hole drift velocity measurements in silicon and their empirical relation to electric field and temperature. *IEEE Transactions on Electron Devices*, 22(11), 1045-1047.
- Canali, C., Ottaviani, G., & Quaranta, A. A. (1971). Drift velocity of electrons and holes and associated anisotropic effects in silicon. *Journal of Physics and Chemistry of Solids*, 32(8), 1707-1720.
- Chapin, J. S. (1979). Sputtering process and apparatus. In: Google Patents.
- Chen, L., Tang, X., Deng, Y., Tianhong, W., Maoshun, C., Zonglong, C., & Youping, F. (2020). Radio frequency detection device and detection method, and microwave oven. In: Google Patents.
- Chen, L., Tang, X., Tianhong, W., Deng, Y., Maoshun, C., Zonglong, C., & Youping, F. (2020). Microwave cooking device, control method, and storage medium. In: Google Patents.
- Chen, X., Yu, Z., Lin, H., Zhao, X., & Liu, C. (2019). Improvements in a 20-kW Phase-Locked Magnetron by Anode Voltage Ripple Suppression. *IEEE Transactions on Plasma Science*.
- Cheney, M. (2011). *Tesla: man out of time*. Simon and Schuster.
- Cheung, A., Rank, D. M., Townes, C., Thornton, D. D., & Welch, W. (1968). Detection of N H 3 Molecules in the Interstellar Medium by Their Microwave Emission. *Physical Review Letters*, 21(25), 1701.
- Cheung, A., Rank, D. M., Townes, C., Thornton, D. D., & Welch, W. (1969). Detection of water in interstellar regions by its microwave radiation. *Nature*, 221(5181), 626-628.
- Chodorow, M., & Wessel-Berg, T. (1961). A high-efficiency klystron with distributed interaction. *IRE Transactions on electron Devices*, 8(1), 44-55.

- Christou, A. (2019). Nanostructures and Crystal Defects in Thick GaN and SiC Epitaxial Layers for Power Electronic Switches. *ECS Transactions*, 92(7), 99-109.
- Code, S. (2015). Limits of Human Exposure to Radiofrequency Electromagnetic Energy in the Frequency Range from 3 kHz to 300 GHz.
- Cohn, S. B. (1959). Design considerations for high-power microwave filters. *IRE Transactions on Microwave Theory and Techniques*, 7(1), 149-153.
- CW Magnetron Sintering Thawing Datasheet*. (2015). [Magnetron Operation]. Hitachi.
- Daimon, M., & Jiang, W. (2007). Modified configuration of relativistic magnetron with diffraction output for efficiency improvement. *Applied physics letters*, 91(19), 191503.
- Das, S., Sherwin, B. D., Aguirre, P., Appel, J. W., Bond, J. R., Carvalho, C. S., Devlin, M. J., Dunkley, J., Dünner, R., & Essinger-Hileman, T. (2011). Detection of the power spectrum of cosmic microwave background lensing by the atacama cosmology telescope. *Physical Review Letters*, 107(2), 021301.
- Dickinson, R. (1975). Evaluation of a microwave high-power reception-conversion array for wireless power transmission. *NASA STI/Recon Technical Report N*, 76, 11207.
- Dickinson, R., & Brown, W. C. (1975). Radiated microwave power transmission system efficiency measurements.
- Dürr, W., Dürr, C., Ehret, P., & Bosch, E. (2015). Thales 150 W C-Band radiation cooled Travelling Wave Tube. 2015 IEEE International Vacuum Electronics Conference (IVEC),
- English, N. J., & MacElroy, J. (2003). Molecular dynamics simulations of microwave heating of water. *The Journal of chemical physics*, 118(4), 1589-1592.
- Fischer, R., Drummond, T. J., Klem, J., Kopp, W., Henderson, T. S., Perrachione, D., & Morkoc, H. (1984). On the collapse of drain IV characteristics in modulation-doped FET's at cryogenic temperatures. *IEEE Transactions on Electron Devices*, 31(8), 1028-1032.
- Florian, C., Mastri, F., Paganelli, R. P., Masotti, D., & Costanzo, A. (2014). Theoretical and numerical design of a wireless power transmission link with GaN-based transmitter and adaptive receiver. *IEEE transactions on Microwave Theory and Techniques*, 62(4), 931-946.
- Foust, J. (2008). A step forward for space solar power. *The Space Review*.
- Frankel, M. Y., Voelker, R. H., & Hilfiker, J. N. (1994). Coplanar transmission lines on thin substrates for high-speed low-loss propagation. *IEEE transactions on Microwave Theory and Techniques*, 42(3), 396-402.
- Fujisawa, K. (1958). General treatment of klystron resonant cavities. *IRE Transactions on Microwave Theory and Techniques*, 6(4), 344-358.

- Fuks, M., & Schamiloglu, E. (2005). Rapid start of oscillations in a magnetron with a "transparent" cathode. *Physical Review Letters*, 95(20), 205101.
- Gandhi, O. P. (2019). Microwave emissions from cell phones exceed safety limits in Europe and the US when touching the body. *IEEE Access*, 7, 47050-47052.
- Gerling, J. E. (1987). Microwave oven power: a technical review. *Journal of Microwave Power and Electromagnetic Energy*, 22(4), 199-207.
- Glaser, P. E. (1992). An overview of the solar power satellite option. *IEEE transactions on Microwave Theory and Techniques*, 40(6), 1230-1238.
- Gold, S. H., & Nusinovich, G. S. (1997). Review of high-power microwave source research. *Review of Scientific Instruments*, 68(11), 3945-3974.
- Goubau, G., & Schwering, F. (1961). On the guided propagation of electromagnetic wave beams. *IRE Transactions on Antennas and Propagation*, 9(3), 248-256.
- Gui-Ming, L., Hu-Dong, C., Bing, S., & Hong-Gang, L. (2013). The Microwave Characteristics of an In_{0.4}Ga_{0.6}As Metal-Oxide-Semiconductor Field-Effect Transistor with an In_{0.49}Ga_{0.51}P Interfacial Layer. *Chinese Physics Letters*, 30(8), 087304.
- Gunaydin, Y., Jahdi, S., Yuan, X., Yu, R., Shen, C., Munagala, S. P., Hopkins, A., Simpson, N., Hosseinzadehlish, M., & Ortiz-Gonzalez, J. (2022). Unclamped inductive stressing of GaN and SiC Cascode power devices to failure at elevated temperatures. *Microelectronics Reliability*, 114711.
- Han, A., Fu, C., Yan, X., Chen, J., Cheng, X., Ke, C., Hou, J., Shen, S., & Zhang, J. (2020). Effect of cobalt ion contamination on proton conduction of ultrathin Nafion film. *International Journal of Hydrogen Energy*, 45(46), 25276-25285.
- Helmersson, U., Lattemann, M., Bohlmark, J., Ehasarian, A. P., & Gudmundsson, J. T. (2006). Ionized physical vapor deposition (IPVD): A review of technology and applications. *Thin solid films*, 513(1-2), 1-24.
- Henley, M., Potter, S., Howell, J., & Mankins, J. (2002). Wireless power transmission Options for Space Solar power. International Astronautical Congress,
- Houston, P., & Evans, A. (1977). Electron drift velocity in n-GaAs at high electric fields. *Solid-State Electronics*, 20(3), 197-204.
- Howes, M. J., & Morgan, D. V. (1985). Gallium arsenide: materials, devices, and circuits. *Chichester*.
- Hu, L., Su, J., Ding, Z., Hao, Q., & Yuan, X. (2014). Investigation on properties of ultrafast switching in a bulk gallium arsenide avalanche semiconductor switch. *Journal of Applied Physics*, 115(9), 094503.
- Hu, L., Su, J., Qiu, R., & Fang, X. (2018). Ultra-wideband microwave generation using a low-energy-triggered bulk gallium arsenide avalanche semiconductor switch with ultrafast switching. *IEEE Transactions on Electron Devices*, 65(4), 1308-1313.

- Hull, A. W. (1921). The magnetron. *Journal of the American Institute of Electrical Engineers*, 40(9), 715-723.
- Hult, B., Thorsell, M., Chen, J.-T., & Rorsman, N. (2022). High Voltage and Low Leakage GaN-on-SiC MISHEMTs on a “Buffer-Free” Heterostructure. *IEEE Electron Device Letters*, 43(5), 781-784.
- Hung, H.-L., Polak-Dingels, P., Webb, K. J., Smith, T., Huang, H., & Lee, C. H. (1989). Millimeter-wave monolithic integrated circuit characterization by a picosecond optoelectronic technique. *IEEE transactions on Microwave Theory and Techniques*, 37(8), 1223-1231.
- Hwang, C., Siegel, D. A., Mo, S.-K., Regan, W., Ismach, A., Zhang, Y., Zettl, A., & Lanzara, A. (2012). Fermi velocity engineering in graphene by substrate modification. *Scientific reports*, 2(1), 1-4.
- Ikeda, H., & Itoh, Y. (2018). 2.4-GHz-band high-power and high-efficiency solid-state injection-locked oscillator. *IEEE transactions on Microwave Theory and Techniques*, 66(7), 3315-3322.
- Ikeda, H., & Itoh, Y. (2019). A 2.4 GHz-Band 250 W, 60% Feedback-Type GaN-HFET Oscillator Using Imbalanced Coupling Resonator for Use in the Microwave Oven. *Applied Sciences*, 9(14), 2887.
- Jackson, T. J., Cosh, M. H., Bindlish, R., Starks, P. J., Bosch, D. D., Seyfried, M., Goodrich, D. C., Moran, M. S., & Du, J. (2010). Validation of advanced microwave scanning radiometer soil moisture products. *IEEE Transactions on Geoscience and Remote Sensing*, 48(12), 4256-4272.
- Jacoboni, C., Nava, F., Canali, C., & Ottaviani, G. (1981). Electron drift velocity and diffusivity in germanium. *Physical Review B*, 24(2), 1014.
- Jang, S.-R., Ahn, S.-H., Ryoo, H.-J., & Kim, J.-S. (2011). Design of High-efficiency Soft-switching Converters for High-power Microwave Generation. *Journal of the Korean Physical Society*, 59(6), 3688-3693.
- Jang, S.-R., Ryoo, H.-J., Ahn, S.-H., Kim, J., & Rim, G. H. (2011). Development and optimization of high-voltage power supply system for industrial magnetron. *IEEE Transactions on Industrial Electronics*, 59(3), 1453-1461.
- Jepsen, R. L., & Muller, M. W. (1951). Enhanced emission from magnetron cathodes. *Journal of Applied Physics*, 22(9), 1196-1207.
- Jiang, W., Masugata, K., & Yatsui, K. (1995). New configuration of a virtual cathode oscillator for microwave generation. *Physics of Plasmas*, 2(12), 4635-4640.
- Jindal, G., Pomeroy, J. W., Watkins, G. T., Morris, K., Kuball, M., & Cappello, T. (2022). High-Speed Electro-Thermal Measurements in RF Power Amplifiers Using Thermo-Reflectance. 2022 International Workshop on Integrated Nonlinear Microwave and Millimetre-Wave Circuits (INMMiC),

- Jones, M., Neculaes, V., Lau, Y., Gilgenbach, R., White, W., Hoff, B., & Jordan, N. (2005). Magnetron priming by multiple cathodes. *Applied physics letters*, 87(8), 081501.
- Jorudas, J., Šimukovič, A., Dub, M., Sakowicz, M., Prystawko, P., Indrišiūnas, S., Kovalevskij, V., Rummyantsev, S., Knap, W., & Kašalynas, I. (2020). Algan/gan on sic devices without a gan buffer layer: Electrical and noise characteristics. *Micromachines*, 11(12), 1131.
- Kachi, M., Kubota, T., Ushio, T., Shige, S., Kida, S., Aonashi, K., Okamoto, K. i., & Oki, R. (2011). Development and utilization of “jaxa global rainfall watch” system based on combined microwave and infrared radiometers aboard satellites. *IEEJ Transactions on Fundamentals and Materials*, 131(9), 729-737.
- Kalinin, P. V., Arzhannikov, A. V., Burdakov, A. V., Bobylev, V. V., Ivanenko, V. G., Makarov, A. G., Mekler, K. I., Polosatkin, S. V., & Rovenskikh, A. F. Station for resonance microwave heating. 2009 European Microwave Conference (EuMC),
- Kaminski, N., & Hilt, O. (2012). SiC and GaN devices-competition or coexistence? 2012 7th International Conference on Integrated Power Electronics Systems (CIPS),
- Karalis, A., Joannopoulos, J. D., & Soljačić, M. (2008). Efficient wireless non-radiative mid-range energy transfer. *Annals of physics*, 323(1), 34-48.
- Kearsley, E. (1984). A new general cavity theory. *Physics in Medicine & Biology*, 29(10), 1179.
- Khachaturyan, K., Weber, E., Tejedor, P., Stacy, A. M., & Portis, A. (1987). Microwave observation of magnetic field penetration of high-T_c superconducting oxides. *Physical Review B*, 36(16), 8309.
- Kim, S. H., Kim, H. J., Shin, S. W., Kim, J. D., Kim, B. K., & Choi, J. J. (2011). Combined power oscillator using GaN HEMT. 2011 IEEE MTT-S International Microwave Symposium,
- King, J. B., & Brazil, T. J. (2012). Nonlinear electrothermal GaN HEMT model applied to high-efficiency power amplifier design. *IEEE transactions on Microwave Theory and Techniques*, 61(1), 444-454.
- Knox, W. H., Henry, J. E., Goossen, K. W., Li, K., Tell, B., Miller, D., Chemla, D., Gossard, A., English, J., & Schmitt-Rink, S. (1989). Femtosecond excitonic optoelectronics. *IEEE journal of Quantum Electronics*, 25(12), 2586-2595.
- Kovalchuk, B. M., Polevin, S. D., Tsygankov, R. V., & Zherlitsyn, A. A. (2010). S-band coaxial vircator with electron beam premodulation based on compact linear transformer driver. *IEEE Transactions on Plasma Science*, 38(10), 2819-2824.
- Kurs, A., Karalis, A., Moffatt, R., Joannopoulos, J. D., Fisher, P., & Soljačić, M. (2007). Wireless power transfer via strongly coupled magnetic resonances. *science*, 317(5834), 83-86.

- Kurs, A., Karalis, A., Moffatt, R., Joannopoulos, J. D., Fisher, P., & Soljačić, M. (2007). Wireless power transfer via strongly coupled magnetic resonances. *science*, 317(5834), 83-86.
- Kutkut, N. H., Divan, D. M., & Novotny, D. W. (1995). Charge equalization for series connected battery strings. *IEEE Transactions on Industry Applications*, 31(3), 562-568.
- Lawless, P. A., & Sparks, L. E. (1988). Modeling particulate charging in ESPs. *IEEE Transactions on Industry Applications*, 24(5), 922-927.
- Lee, B.-i., Geum, J. M., Jung, E. S., Kang, E. G., Kim, Y.-T., & Sung, M. Y. (2014). Analysis of lattice temperature in super junction trench gate power MOSFET as changing degree of trench etching. *JSTS: Journal of Semiconductor Technology and Science*, 14(3), 263-267.
- Lee, C. H. (1990). Picosecond optics and microwave technology. *IEEE transactions on Microwave Theory and Techniques*, 38(5), 596-607.
- Lee, J., & Wang, H. (2009). Study of subharmonically injection-locked PLLs. *IEEE journal of solid-state circuits*, 44(5), 1539-1553.
- Lee, T. (2015). A Place in the History Books [President's Column]. *IEEE Microwave Magazine*, 16(2), 8-9.
- Levy, R., & Cohn, S. B. (1984). A history of microwave filter research, design, and development. *IEEE transactions on Microwave Theory and Techniques*, 32(9), 1055-1067.
- Littlejohn, S. D. (2013). *Electrical properties of graphite nanoparticles in silicone: Flexible oscillators and electromechanical sensing*. Springer Science & Business Media.
- Liu, L., Yang, Y., Li, Z., Jin, X., Mo, W., & Liu, X. (2017). Low power consumption and continuously tunable all-optical microwave filter based on an opto-mechanical microring resonator. *Optics express*, 25(2), 960-971.
- Liu, Z., Chen, X., Yang, M., Wu, P., Huang, K., & Liu, C. (2018). Experimental studies on a four-way microwave power combining system based on hybrid injection-locked 20-kW S-band magnetrons. *IEEE Transactions on Plasma Science*, 47(1), 243-250.
- Lu, P., Song, C., Cheng, F., Zhang, B., & Huang, K. (2020). A Self-Biased Adaptive Reconfigurable Rectenna for Microwave Power Transmission. *IEEE Transactions on Power Electronics*, 35(8), 7749-7754.
- Lu, P., Song, C., & Huang, K. M. (2020). A Compact Rectenna Design With Wide Input Power Range for Wireless Power Transfer. *IEEE Transactions on Power Electronics*, 35(7), 6705-6710.

- Lu, X., Niyato, D., Wang, P., Kim, D. I., & Han, Z. (2015). Wireless charger networking for mobile devices: Fundamentals, standards, and applications. *IEEE Wireless Communications*, 22(2), 126-135.
- Luo, B., Long, T., Guo, L., Dai, R., Mai, R., & He, Z. (2020). Analysis and design of inductive and capacitive hybrid wireless power transfer system for railway application. *IEEE Transactions on Industry Applications*, 56(3), 3034-3042.
- Mahan, J. E. (2000). *Physical vapor deposition of thin films*.
- Makishima, H., Miyano, S., Imura, H., Matsuoka, J., Takemura, H., & Okamoto, A. (1999). Design and performance of traveling-wave tubes using field emitter array cathodes. *Applied surface science*, 146(1-4), 230-233.
- Maleki, L. (2011). The optoelectronic oscillator. *Nature Photonics*, 5(12), 728-730.
- Mankins, J., & Howell, J. (2000). Overview of the space solar power (SSP) Exploratory Research And Technology (SERT) program. 35th Intersociety Energy Conversion Engineering Conference and Exhibit,
- Mankins, J., Kaya, N., & Vasile, M. (2012). SPS-ALPHA: the first practical solar power satellite via arbitrarily large phased array (a 2011-2012 NIAC project). 10th International Energy Conversion Engineering Conference,
- Martin, D., Jianu, A., & Ighigeanu, D. (2001). A method for the 2.45-GHz magnetron output power control. *IEEE transactions on Microwave Theory and Techniques*, 49(3), 542-545.
- Matsumoto, H. (2002). Research on solar power satellites and microwave power transmission in Japan. *IEEE Microwave Magazine*, 3(4), 36-45.
- Mattox, D. M. (2002). Physical vapor deposition (PVD) processes. *Metal Finishing*, 100, 394-408.
- Mattox, D. M. (2010). *Handbook of physical vapor deposition (PVD) processing*. William Andrew.
- Miller, S. T. (1981). Dictionary of scientific biography. *Reference Services Review*.
- Mohamadzade, B., & Afsahi, M. (2017). Mutual coupling reduction and gain enhancement in patch array antenna using a planar compact electromagnetic bandgap structure. *IET Microwaves, Antennas & Propagation*, 11(12), 1719-1725.
- Moller, C., Elfsberg, M., Hurtig, T., Larsson, A., & Nyholm, S. E. (2009). Proof of Principle Experiments on Direct Generation of the TE_{11} Mode in a Coaxial Vircator. *IEEE Transactions on Plasma Science*, 38(1), 26-31.
- Musil, J., Baroch, P., Vlček, J., Nam, K., & Han, J. (2005). Reactive magnetron sputtering of thin films: present status and trends. *Thin solid films*, 475(1-2), 208-218.

- Nasiri, A., Zabalawi, S. A., & Mandic, G. (2009). Indoor power harvesting using photovoltaic cells for low-power applications. *IEEE Transactions on Industrial Electronics*, 56(11), 4502-4509.
- Ni, Z., Wang, Y., Yu, T., You, Y., & Shen, Z. (2008). Reduction of Fermi velocity in folded graphene observed by resonance Raman spectroscopy. *Physical Review B*, 77(23), 235403.
- Nüchter, M., Ondruschka, B., Bonrath, W., & Gum, A. (2004). Microwave assisted synthesis—a critical technology overview. *Green chemistry*, 6(3), 128-141.
- O'Neill, J. (2007). *Prodigal genius: the life of Nikola Tesla*. Book Tree.
- Oka, T., Ueno, Y., Ina, T., & Hasegawa, K. (2014). Vertical GaN-based trench metal oxide semiconductor field-effect transistors on a free-standing GaN substrate with blocking voltage of 1.6 kV. *Applied Physics Express*, 7(2), 021002.
- Okabe, K. (1929). On the short-wave limit of magnetron oscillations. *Proceedings of the Institute of Radio Engineers*, 17(4), 652-659.
- Okawa, T., Kiuchi, K., Okabe, H., & Ohsato, H. (2001). Microwave dielectric properties of $\text{BaLa}_4\text{Ti}_3\text{O}_{12}$ homologous series. *Japanese Journal of Applied Physics*, 40(9S), 5779.
- Oraizi, H., & Afsahi, M. (2007). Analysis of planar dielectric multilayers as FSS by transmission line transfer matrix method (TLTMM). *Progress In Electromagnetics Research*, 74, 217-240.
- Orr, J. A., Emanuel, A. E., & Pileggi, D. J. (1984). Current harmonics, voltage distortion, and powers associated with electric vehicle battery chargers distributed on the residential power system. *IEEE Transactions on Industry Applications*(4), 727-734.
- Osepchuk, J. M. (1984). A history of microwave heating applications. *IEEE transactions on Microwave Theory and Techniques*, 32(9), 1200-1224.
- Patterson, M. J., & Sovey, J. S. (2013). History of electric propulsion at NASA Glenn Research Center: 1956 to present. *Journal of Aerospace Engineering*, 26(2), 300-316.
- Pellish, J., Carts, M., Buchner, S., Campola, M., Xapsos, M., & Seidleck, C. (2010). Pulsed Laser Single-Event Transient Testing of the MiniCircuits RAM-3+ MMIC InGaP HBT Amplifier. In.
- Pengelly, R. S., Wood, S. M., Milligan, J. W., Sheppard, S. T., & Pribble, W. L. (2012). A review of GaN on SiC high electron-mobility power transistors and MMICs. *IEEE transactions on Microwave Theory and Techniques*, 60(6), 1764-1783.
- Peterson, P., Kamhawi, H., Manzella, D., & Jacobson, D. (2007). Hall thruster technology for NASA science missions: HiVHAC status update. 43rd AIAA/ASME/SAE/ASEE Joint Propulsion Conference & Exhibit,

- Pottelette, R., Ergun, R., Treumann, R., Berthomier, M., Carlson, C., McFadden, J., & Roth, I. (1999). Modulated electron-acoustic waves in auroral density cavities: FAST observations. *Geophysical Research Letters*, 26(16), 2629-2632.
- Prati, E., & Fanciulli, M. (2008). Manipulation of localized charge states in n-MOSFETs with microwave irradiation. *Physics Letters A*, 372(17), 3102-3104.
- Protection, I. C. o. N.-I. R. (2017). ICNIRP statement on diagnostic devices using non-ionizing radiation: existing regulations and potential health risks. *Health physics*, 112(3), 305-321.
- Qian, Y., & Yamashita, E. (1991). Phase compensation and waveform reshaping of picosecond electrical pulses using dispersive microwave transmission lines. *IEEE transactions on Microwave Theory and Techniques*, 39(6), 924-929.
- Raskin, J.-P., Gillon, R., Chen, J., Vanhoenacker-Janvier, D., & Colinge, J.-P. (1998). Accurate SOI MOSFET characterization at microwave frequencies for device performance optimization and analog modeling. *IEEE Transactions on Electron Devices*, 45(5), 1017-1025.
- Rostov, V. V., Romanchenko, I. V., Gunin, A. V., Pedos, M. S., Rukin, S. N., Sharypov, K. A., Shunailov, S. A., Ulmaskulov, M. R., & Yalandin, M. I. (2018). Review of experiments on microwave beam steering in arrays of high-power oscillators by the control of voltage rise time. *IEEE Transactions on Plasma Science*, 46(10), 3640-3647.
- Saeed, W., Shoaib, N., Cheema, H. M., & Khan, M. U. (2018). RF energy harvesting for ubiquitous, zero power wireless sensors. *International Journal of Antennas and Propagation*, 2018.
- Saldin, E., Schneidmiller, E., & Yurkov, M. (2002). Klystron instability of a relativistic electron beam in a bunch compressor. *Nuclear Instruments and Methods in Physics Research Section A: Accelerators, Spectrometers, Detectors and Associated Equipment*, 490(1-2), 1-8.
- Sasaki, S., Tanaka, K., Higuchi, K., Okuizumi, N., Kawasaki, S., Shinohara, N., Senda, K., & Ishimura, K. (2007). A new concept of solar power satellite: Tethered-SPS. *Acta Astronautica*, 60(3), 153-165.
- Sayadian, H. A., Li, M., & Lee, C. H. (1989). Generation of high-power broad-band microwave pulses by picosecond optoelectronic technique. *IEEE transactions on Microwave Theory and Techniques*, 37(1), 43-50.
- Schiller, S., Goedicke, K., Reschke, J., Kirchhoff, V., Schneider, S., & Milde, F. (1993). Pulsed magnetron sputter technology. *Surface and Coatings Technology*, 61(1-3), 331-337.
- Schlesak, J., Alden, A., & Ohno, T. (1985). Sharp (stationary high altitude relay platform)-rectenna and low altitude tests. GLOBECOM'85-Global Telecommunications Conference,

- Schnieder, F., Bengtsson, O., Schmückle, F.-J., Rudolph, M., & Heinrich, W. (2013). Simulation of RF power distribution in a packaged GaN power transistor using an electro-thermal large-signal description. *IEEE transactions on Microwave Theory and Techniques*, 61(7), 2603-2609.
- Schubert, E., & Ploog, K. (1984). Shallow and deep donors in direct-gap n-type Al_xGa_{1-x}As: Si grown by molecular-beam epitaxy. *Physical Review B*, 30(12), 7021.
- Sessler, A. M., & Simon, S. Y. (1987). Relativistic klystron two-beam accelerator. *Physical Review Letters*, 58(23), 2439.
- Shakeri, S., Mirak, S. A., Pantuck, A., Sisk, A., Ahuja, P., Lu, D. S., & Raman, S. (2018). PD61-10 SAFETY AND EFFICACY OF PERCUTANEOUS US AND CT GUIDED MICROWAVE ABLATION OF T1A AND T1B RENAL TUMORS. *The Journal of Urology*.
- Shen, Z.-Y., Wilker, C., Pang, P., Face, D. W., Carter, C. F., & Harrington, C. M. (1997). Power handling capability improvement of high-temperature superconducting microwave circuits. *IEEE transactions on applied superconductivity*, 7(2), 2446-2453.
- Sivadas, A., Yu, M., & Cameron, R. (2000). A simplified analysis for high power microwave bandpass filter structures. 2000 IEEE MTT-S International Microwave Symposium Digest (Cat. No. 00CH37017),
- Skolnik, M. (2002). Role of radar in microwaves. *IEEE transactions on Microwave Theory and Techniques*, 50(3), 625-632.
- Sliney, D., Aron-Rosa, D., DeLori, F., Fankhauser, F., Landry, R., Mainster, M., Marshall, J., Rassow, B., Stuck, B., & Trokel, S. (2005). Adjustment of guidelines for exposure of the eye to optical radiation from ocular instruments: statement from a task group of the International Commission on Non-Ionizing Radiation Protection (ICNIRP). *Applied optics*, 44(11), 2162-2176.
- Somekh, R. (1984). The thermalization of energetic atoms during the sputtering process. *Journal of Vacuum Science & Technology A: Vacuum, Surfaces, and Films*, 2(3), 1285-1291.
- Sproul, W. D. (1996). Physical vapor deposition tool coatings. *Surface and Coatings Technology*, 81(1), 1-7.
- Strassner, B., & Chang, K. (2013). Microwave power transmission: Historical milestones and system components. *Proceedings of the IEEE*, 101(6), 1379-1396.
- Sun, B., Jorgensen, K. L., Zhang, Z., & Andersen, M. A. (2020). Research of Power Loop Layout and Parasitic Inductance in GaN Transistor Implementation. *IEEE Transactions on Industry Applications*.
- Sung, K. Y., Jeon, W., Jung, Y., Lim, J. E., Uhm, H. S., & Choi, E. H. (2005). Influence of anode-cathode gap distance on output characteristics of high-power microwave from coaxial virtual cathode oscillator. *IEEE Transactions on Plasma Science*, 33(4), 1353-1357.

- Surducun, V., & Surducun, E. (2013). Low-Cost Microwave Power Generator for Scientific and Medical Use [Application Notes]. *IEEE Microwave Magazine*, 14(4), 124-130.
- Surducun, V., Surducun, E., & Ciupa, R. (2011). Variable power, short microwave pulses generation using a CW magnetron. *Advances in Electrical and Computer Engineering*, 11(2), 49-54.
- Takenaka, I., Ishikura, K., Asano, K., Takahashi, S., Murase, Y., Ando, Y., Takahashi, H., & Sasaoka, C. (2014). High-efficiency and high-power microwave amplifier using GaN-on-Si FET with improved high-temperature operation characteristics. *IEEE transactions on Microwave Theory and Techniques*, 62(3), 502-512.
- Tanaka, M., & Sato, M. (2007). Microwave heating of water, ice, and saline solution: Molecular dynamics study. *The Journal of chemical physics*, 126(3), 034509.
- Tang, Y., Loh, P. C., Wang, P., Choo, F. H., Gao, F., & Blaabjerg, F. (2011). Generalized design of high performance shunt active power filter with output LCL filter. *IEEE Transactions on Industrial Electronics*, 59(3), 1443-1452.
- Tiebout, M. (2004). A CMOS direct injection-locked oscillator topology as high-frequency low-power frequency divider. *IEEE journal of solid-state circuits*, 39(7), 1170-1174.
- Treado, T. A., Bolton, R. A., Hansen, T. A., Brown, P. D., & Barry, J. D. (1992). High-power, high efficiency, injection-locked, secondary-emission magnetron. *IEEE Transactions on Plasma Science*, 20(3), 351-359.
- Van Dyck Jr, R., Schwinberg, P., & Dehmelt, H. (1977). Precise measurements of axial, magnetron, cyclotron, and spin-cyclotron-beat frequencies on an isolated 1-MeV electron. *Physical Review Letters*, 38(7), 310.
- Vintizenko, I. (2018). *Relativistic Magnetrons*. CRC Press.
- Vintizenko, I. I. (2014). Modifications of a relativistic magnetron. *Technical Physics*, 59(1), 113-118.
- von Helmolt, C. H., Kruger, U., Kruger, K., & Grosskopf, G. (1997). A mobile broadband communication system based on mode-locked lasers. *IEEE transactions on Microwave Theory and Techniques*, 45(8), 1424-1430.
- Vyas, S. K., Maurya, S., & Singh, V. P. (2016). Efficiency enhancement of CW magnetron by ferrite material filling. *IEEE Transactions on Plasma Science*, 44(12), 3262-3267.
- Wada, Y., & Tomizawa, M. (1988). Drain avalanche breakdown in gallium arsenide MESFET's. *IEEE Transactions on Electron Devices*, 35(11), 1765-1770.
- Walton, J., Alexander, M., Fairley, N., Roach, P., & Shard, A. (2016). Film thickness measurement and contamination layer correction for quantitative XPS. *Surface and Interface Analysis*, 48(3), 164-172.

- Wang, K., Dahan, R., Shentcis, M., Kauffmann, Y., Hayun, A. B., Reinhardt, O., Tsesses, S., & Kaminer, I. (2020). Coherent interaction between free electrons and a photonic cavity. *Nature*, 582(7810), 50-54.
- Wang, W., Song, Q., Zhang, S., Li, Y., Ahmad, M., & Gong, Y. (2020). The Loss Analysis and Efficiency Optimization of Power Inverter Based on SiC MOSFETs Under the High-Switching Frequency. *IEEE Transactions on Industry Applications*.
- Willert-Porada, M. (2006). *Advances in microwave and radio frequency processing*. Springer.
- Wu, M., Cheng, K., Yang, L., Hou, B., Zhang, X.-C., Wang, P., Zhang, M., Zhu, Q., Zheng, X.-F., & Hu, Y.-S. (2022). Structural and thermal analysis of polycrystalline diamond thin film grown on GaN-on-SiC with an interlayer of 20 nm PECVD-SiN. *Applied physics letters*, 120(12), 121603.
- Xu, J., Gu, L., Ye, Z., Kargarrazi, S., & Davila, J. M. R. (2019). Cascode GaN/SiC: A Wide-Bandgap Heterogenous Power Device for High-Frequency Applications. *IEEE Transactions on Power Electronics*.
- Xu, K., Wang, Y., Zheng, C., Xiong, J., & Wang, G. (2014). Terahertz performance of a GaN-based planar nanochannel device. *Journal of Nanomaterials*, 2014.
- Xu, X., Wei, Y., Shen, F., Duan, Z., Gong, Y., Yin, H., & Wang, W. (2011). Sine waveguide for 0.22-THz traveling-wave tube. *IEEE Electron Device Letters*, 32(8), 1152-1154.
- Yang, F., Singh, M., Uren, M. J., Martin, T., Hirshy, H., Casbon, M. A., Tasker, P. J., & Kuball, M. (2022). Study of drain injected breakdown mechanisms in AlGaIn/GaN-on-SiC HEMTs. *IEEE Transactions on Electron Devices*, 69(2), 525-530.
- Yang, Y.-R. (2013). A magnetron power supply with transition-mode ZVS inverter. 2013 IEEE 10th International Conference on Power Electronics and Drive Systems (PEDS),
- Yao, X. S., & Maleki, L. (1996). Optoelectronic oscillator for photonic systems. *IEEE journal of Quantum Electronics*, 32(7), 1141-1149.
- Yao, X. S., & Maleki, L. (2000). Multiloop optoelectronic oscillator. *IEEE journal of Quantum Electronics*, 36(1), 79-84.
- Ye, Y., Wu, M., Kong, Y., Liu, R., Yang, L., Zheng, X., Jiao, B., Ma, X., Bao, W., & Hao, Y. (2022). Active Thermal Management of GaN-on-SiC HEMT With Embedded Microfluidic Cooling. *IEEE Transactions on Electron Devices*.
- Yilmaz, M., & Krein, P. (2012). Review of charging power levels and infrastructure for plug-in electric and hybrid vehicles and commentary on unidirectional charging. IEEE International Electrical Vehicle Conference,

- Yoshino, K., Sowada, U., & Schmidt, W. (1976). Effect of molecular solutes on the electron drift velocity in liquid Ar, Kr, and Xe. *Physical review A*, 14(1), 438.
- You, Y., Wang, N.-Y., Kubota, T., Aonashi, K., Shige, S., Kachi, M., Kummerow, C., Randel, D., Ferraro, R., & Braun, S. (2020). Comparison of TRMM microwave imager rainfall datasets from NASA and JAXA. *Journal of Hydrometeorology*, 21(3), 377-397.
- Yu, X. (2022). Investigation of Advanced GaN and SiC Semiconductor Materials: Key Characteristics and Diverse Applications. *Highlights in Science, Engineering and Technology*, 5, 51-61.
- Yuen, J. H. (2013). *Deep space telecommunications systems engineering*. Springer Science & Business Media.
- Zhang, W., Jia, B., & Furumai, H. (2018). Fabrication of graphene film composite electrochemical biosensor as a pre-screening algal toxin detection tool in the event of water contamination. *Scientific reports*, 8(1), 1-10.
- Zhang, W., Wang, K., Zhu, S., Li, Y., Wang, F., & He, H. (2009). Yttrium-doped TiO₂ films prepared by means of DC reactive magnetron sputtering. *Chemical Engineering Journal*, 155(1-2), 83-87.
- Zhou, X. J., Yoshida, T., Lanzara, A., Bogdanov, P., Kellar, S., Shen, K., Yang, W., Ronning, F., Sasagawa, T., & Kakeshita, T. (2003). Universal nodal Fermi velocity. *Nature*, 423(6938), 398-398.
- Zhu, G., Pahl, B., Xu, Z., Samanta, S., Wong, I., Bhattacharya, S., Beddingfield, R., & Ohodnicki, P. R. (2020). Wireless Power Transformation for Data Centers and Medium Voltage Applications. 2020 IEEE Applied Power Electronics Conference and Exposition (APEC),